NTNU – Trondheim
Norwegian University of
Science and Technology

Effect of Solution Annealing on Plasma Weld Deposited Ti-6Al-4V Characterized by In-Situ Tensile Testing Combined With EBSD

Erlend Næss Trøan

Materials Science and Engineering
Submission date: June 2014
Supervisor: Ola Jensrud, IMTE
Co-supervisor: Jarle Hjelen, IMT
Martin Borlaug Mathisen, Norsk Titanium

Norwegian University of Science and Technology
Department of Materials Science and Engineering

Preface

This work has been carried out at the Norwegian Univeristy of Science and Technology (NTNU), at the Department of Materials Science and engineering, as a master thesis within Material development and properties.

I would like to express my gratitude to my supervisor Ola Jensrud for very good guidance throughout the duration of this project. I would also like to thank my co-supervisor Jarle Hjelen, for many productive talks. In addition, my sincere thanks goes to my company contact at Norsk Titanium, Martin Borlaug Mathisen, for very helpful guidance along the way.

Trondheim, June 2014

Erlend Næss Trøan

Acknowledgements

My sincere thanks go out to the following persons who have guided and helped me throughout the work of my master thesis.

Ola Jensrud (NTNU)	Supervisor
Jarle Hjelen (NTNU)	Co-supervisor
Martin Borlaug Mathisen (NTi)	Company Supervisor
Yingda Yu (IMT)	Engineer at SEM lab
Trygve Schanche (NTNU)	Labassistant
Torild Krogstad (NTNU)	Labassistant
Robert Karlsen (NTNU)	Cutting of samples
Knut Erik Snilsberg (SINTEF)	Working with titanium at SINTEF Raufoss Manufacturing
Rene de Kloe (EDAX)	Engineer in EDAX (producer of OIM Analysis)
Eli Beate Larsen (NTNU)	Dilatometer
Delphine Leroy (NTNU)	ReSiNa furnace
Wilhelm Dall (SINTEF)	Senior engineer at SINTEF
Astrid Salvesen (NTNU)	Coordinator at the glassblowing workshop

I would also like to dedicate my thanks to Norsk Titanium and SINTEF Raufoss Manufacturing for supplying material and data related to the process and tensile test.

Abbreviations list

AC	Air-cooled
AM	Additive manufacturing
BCC	Body centered cubic
BOR	Burgers orientation relationship
CAD	Computer aided design
CI	Confidence index
CP	Commericially pure
CRSS	Critical resolved shear stress
EBSD	Electron backscatter diffraction
FC	Furnace-cooled
HCP	Hexagonal close packed
IPF	Inverse pole figure
IQ	Image quality
NTi	Norsk Titanium
ROI	Region of interest
SE	Seconday electrons
SEM	Scanning electron microscope
SiC	Silicon carbide
TEM	Transmission electron microscope

Abstract

This work is based on the work done by Mathisen et al. [1], which considers the mechanical properties of the components produced by Norsk Titanium (NTi). NTi produces Ti-6Al-4V (grade 5 titanium) components by additive manufacturing (AM). After receiving samples from NTi, the material were heat-treated in order to study the possible differences in deformation mechanisms. The material was either furnace-cooled (FC) or air-cooled (AC) after solution annealing at 950°C for 1 hour. Both FC and AC samples went to an aging procedure at 600°C for two hours after solution annealing. The deformation mechanisms were observed by doing in-situ tensile tests with electron-backscattered diffraction (EBSD). The time spent on sample preparation for EBSD proved valuable as the average CI-, fit- and IQ-values for the tensile specimens before deformation were 0.44, 1.07 and 144.8 respectively.

Both prismatic and basal slip are present in the material, in addition to hard/soft-grain deformation. The combination of elastic stiffness and Schmid factor proved effective for calculating the activation and propagation of all three types of deformation. In the as-received material, the deformation accumulates at the columnar β-grain boundaries, while after heat treatment, the deformation are more uniformly distributed among the β-grains. The anisotropy of the material is however still obvious, as the deformation is concentrated in certain grain.

The AC material gained a more homogenous width of α-lamellas as compared to the as-received material, although tendencies towards basketweave structure were still present. The FC material obtained α-lamellae that are more discontinuous than in the as-received material. The larger the width of the α-lamellas, the higher the ductility, as slip can propagate longer. If the slip isn't restricted by the orientation of the neighboring lamellas, the material can travel even further. Due to a strict orientation relationship, the material doesn't seem to obtain a more isotropic texture after the heat treatment. Due to a non-equilibrium composition and microstructure in the AM material, the use of dilatometry was unable to obtain any useful data to determine the transition temperature. The first specimens that underwent a heat treatment showed a very brittle behavior, as the material had been exposed to a contamination of both hydrogen and oxygen. This underlines the importance of atmospheric protection when operating with titanium at elevated temperatures.

Sammendrag

Det følgende prosjektet er basert på arbeidet til Mathisen et. al. (**REFERENCE**), of tar for seg de mekaniske egenskapene til komponenter produsert av Norsk Titanium (NTi). NTi produserer Ti-6Al-4V (grad 5 titan) komponenter med bruk av additive manufacturing (AM). Etter at prøvene fra NTi ble mottatt, gikk de igjennom en varmebehandling for å studere mulige forskjeller i deformasjon. Materialet ble enten ovnskjølt (FC) eller luftkjølt (AC) etter herding på 950°C i 1 time. Både FC og AC materialet gikk deretter gjennom en eldingsprosess på 600°C i 2 timer. Deformasjonen ble observert ved å gjennomføre en in-situ strekktest med electron-backscattered diffraction (EBSD). Prøvepreparingen var vellykket, og den gjennomsnittlige CI-, fit- og IQ-verdiene før testing var på henholdsvis 0.44, 1.07 og 144.8.

Både prisme og basal slip er tilstede i materialet, i tillegg til hard/mykt-korn deformasjon. Bruken av E-modul og Schmid faktor viste seg å være egnet for å beregne aktivering og oppførsel på alle de tre slipp-systemene. I materialet mottatt fra NTi (grunnmateriale), er det tydelig at deformasjon konsentrerer seg langs β-korngrensene, mens det etter varmebehandling er en mer uniform fordeling av deformasjon i β-kornene. Anisotropien i materialet er allikevel fortsatt tilstede etter varmebehandling, ettersom deformasjonen fortsatt er mer konsentrert i noen korn.

AC materialet har en mer homogen bredde på α-lamellene enn i grunnmaterialet, selv om basketweave-strukturen fortsatt er tydelig. FC materialet viser en mer diskontinuerlig lamellstruktur, enn grunnmaterialet. Jo bredere α-lamellene er, jo høyere er duktiliteten, ettersom slip kan bevege seg fritt inne i lamellen. Hvis slipplinjene ikke er begrenset av orientering på nabolamellene, kan de traversere enda lenger i materialet. På grunn av et strengt orienteringsforhold i materialet oppnås det ikke mer isotropi etter varmebehandling, og pga. at både sammensetning og mikrostruktur ikke er i likevekt gir ikke dilatometer-forsøkene noen resultater som kunne brukes for å avgjøre fasetransformasjon. De første prøvene som gikk igjennom varmebehandling viste en veldig sprø oppførsel under testing. Dette skyldes forurensning av både hydrogen og oksygen, og underbygger viktigheten av atmosfærisk beskyttelse når man operer med titan ved høye temperaturer.

Table of Content

1. Introduction

Ti-6Al-4V is a well-known grade 5 titanium alloy, and is described as the “workhorse” of the titanium alloys. Up to date the main functions of the alloy have been limited to critical aerospace components and medical implants, mainly due the cost related to producing the titanium. Norsk Titanium (NTi) has patented an Additive manufacturing (AM) technique severely decreasing the costs of producing titanium components. The AM process produces close to net-shape products, with far less material waste than conventional techniques (80-90%). Even though NTi have started full scale production, there is a continuously research being performed trying to increase the understanding of the material and process as a whole. The previous two years project work and master thesis have been performed in relation to NTis process [1].

1.1 Ti-6Al-4V

Ti-6Al-4V is an α/β titanium alloy, and is the most widely used titanium alloy in the world today, mainly because of its high strength, good reproducibility and high fatigue resistance [2]. These properties in combination with the properties exhibited by more or less all titanium alloys, such as: low density, low modulus and excellent corrosion resistance, temperature resilience makes Ti-6Al-4V very attractive for the aerospace and other industries where the requirements to mechanical properties and weight are high. Although titanium is a quite common metal, the costs of the final products have remained relatively high compared to its competitors, such as steel and aluminum. This is due to the cost of producing raw titanium as well as machining and processing of products [3]. The need for an alternate way of producing titanium is therefore imminent.

1.2 Direct Metal Deposition

Additive manufacturing (AM) is a production technique which in the most general terms are “the process of joining materials to make objects from 3D model data, usually layer upon layer” [4]. By decreasing the thickness of each layer, the product will be closer to its final shape, thus reducing the machining needed afterwards. The primary usage of AM-products the recent years have been electronics and medical and dental applications. But other industries like aerospace and automotive industries have started showing interest in the benefits with both reduced production time and the cost savings that are related to additive manufacturing. Because of the issues related

to properties and reproducibility [5] AM still has a way to go before being fully comparable to the more conventional wrought products.

AM uses a three dimensional CAD model to control the process, and focused thermal energy is used to fuse material together by partial re-melting during deposition. In the case for NTi the source for thermal energy is a plasma arc, very similar to the one used for welding (Figure 1). The energy source can also be provided by a laser or electron beam, but to increase deposition rates arc-based welding techniques have been used [6]. During production two robot arms, with six rotation axes each are being used [7]. The specific technique applied by NTi is done in a chamber with an overpressure of argon gas, to avoid the titanium to react with air. The production is done by laying strings of molten Ti-6Al-4V from a wire feedstock on a substrate plate by a geometry given by the computer software. The use of wire instead of powder feedstock is known to give less contamination and a higher productivity.

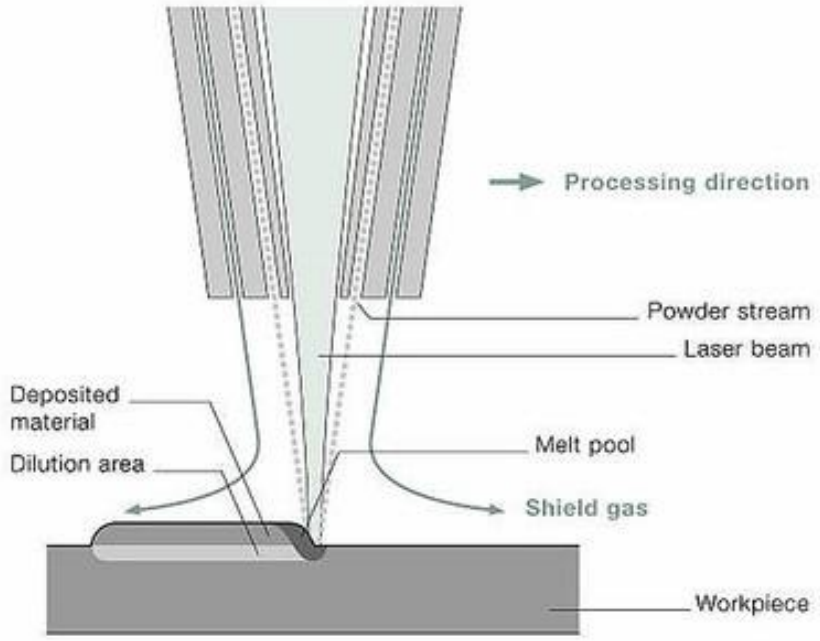

Figure 1: Schematic illustration of the AM process. The heat source for this image is a laserbeam. [8]

The substrate plate (workpiece) works as a heat sink conducting heat away from the end product, which results in a thermal gradient passing through the already deposited material. For the material studied in this paper the deposition direction is the x-axis, the height (build) direction is the z-axis while the y-axis transverse direction. Consequently, the metal is deposited along the x-

axis, moving in the transverse direction for each weld bead that is completed. This is done until the desired x/y-plane is completed. The torch then starts building a new x/y-plane, on top of the previous. Before the deposition of each new string of material, the surrounding material have to cool down to a given temperature (interpass temperature). The already deposited metal will undergo several thermal cycles as new material is beign deposited, and has an anisotropic behavior. To obtain a more isotropic and ductile material NTi has started looking into different heat treatments to alternate the microstructure.

2. Theory

The following sections give a brief insight to the fundamental theoretical principles of for both titanium and Ti-6Al-4V, in addition to a brief introduction of EBSD and texture analysis by pole figures.

2.1 Crystal Structure

Alloys like Ti-6Al-4V exhibits an allotropic transformation, meaning that the crystal structure changes at a given temperature called the transition (transus) temperature. In Ti-6Al-4V this type of transformation takes place when the body centered cubic (BCC) β-phase starts to transform to the hexagonal close packed (HCP) α-phase (Figure 2). The α-phase is present at room temperature and up to the transus temperature, which is approximately 1000°C for Ti-6Al-4V. 100% β-phase is present at temperatures above the transus temperature, and in most α/β-alloys some β is even present at room temperature.

The hexagonal structure shown in figure 2 has a c/a-ratio that is slightly more compressed (1,587) than the ideal ratio for HCP of 1,633, which will affect the activation of slip systems in the HCP lattice. β can exist down to room temperature either as a metastable phase due to quenching, or stabilized by alloying elements called β-stabilizers. Generally the β-stabilizers are transition and noble metals with unfilled electron bands, such as vanadium. The β-phase could be desired for some purposes, such as for workability [9]. In the same way as β, the α-phase can be stabilized at increasing temperatures by alloying with α-stabilizers. Generally the α-stabilizers are non-transition metals, or interstitial like nitrogen and oxygen. The alloying elements can place themselves either interstitial or substitutional in the crystal lattices, although titanium exhibits substitutional solid solution with most elements with an atomic size factor within 20% [10].

Considering the general form of Gibb's free energy:

$$G = H - TS \qquad 1.$$

The entropy of the BCC β is somewhat larger than the entropy of the more closepacked HCP α, so the β will increase its stability as the temperature inceases. When $G_\alpha > G_\beta$, the dense BCC lattice is thermodynamically preferable as compared to the HCP structure.

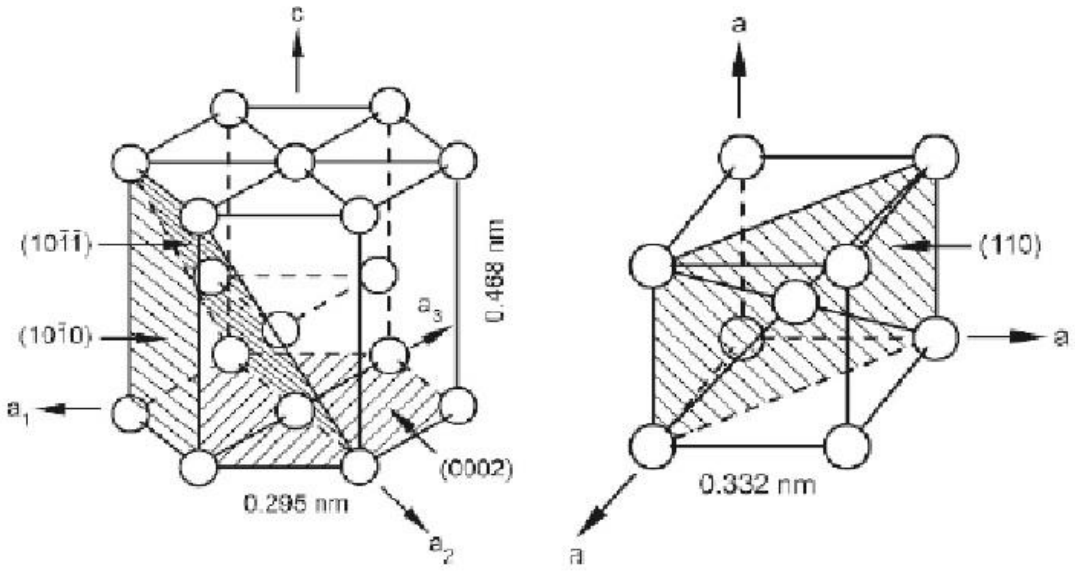

Figure 2: Left: Unit cell of α-Ti, HCP structure. Basal(0002), prismatic $(10\bar{1}0)$ and pyramidal $(10\bar{1}\bar{1})$ planes are shaded Right: Unit cell of β-Ti, BCC structure. The shaded area is the (110)-plane [2]

2.2 Phase Diagram

A binary phase diagram for titanium can have different shapes depending on which alloying element that is considered, as shown in Figure 3. By adding aluminum the transus temperature reaches higher levels, and the chance for observing the β-phase at room temperature decreases, aluminum is therefore considered an α-stabilizer. By addition of sufficient vanadium (β-isomorphous in Figure 3) the β can be stabilized down to room temperature by decreasing the transus temperature, as well as giving a dual phase region (α+β) at intermediate vanadium contents. For this reason, vanadium is considered a β-stabilizer.

The β eutectoid elements such as Fe, Cr and Si are widely applied in different titanium alloys, while the use of other elements such as Ni, Cu, Mn etc. rather limited. The addition of hydrogen, one of the β eutectoid elements (Figure 3), gives a low transus temperature around 300°C [2] with an addition of 30wt%. Combining that with the high diffusivity of hydrogen, one can achieves a microstructure refinement process called hydrogenation/dehydrogenation (HDH) process. The

neutral phase diagram in Figure 3 is a result of addition of elements which react more or less neutral, meaning that they will decrease the transus temperature slightly before increasing it again at higher concentrations.

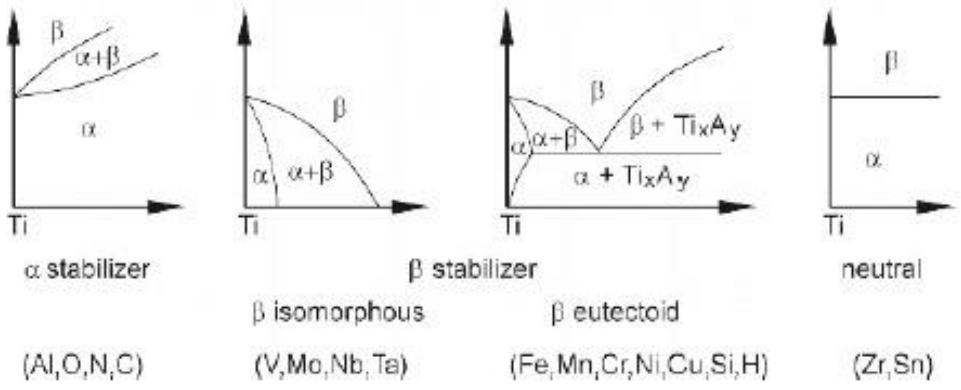

Figure 3: Phase diagrams, illustrating the effect of the different alloying elements in titanium [2]

In Figure 4 the two pseudo binary phase diagrams for Ti-6Al-4V are given, and the effect given by the addition of aluminium and vanadium can be viewed separately. The phase diagrams in Figure 4 are given in equilibrium, which is rarely the case in any metallurgical processes, especially not for the AM process. Parameters such as the cooling rate will have a large influence on the final phase composition and microstructure.

It should be noted that there will also be trace elements in the alloy such as oxygen, nitrogen and iron. Oxygen takes interstitial sites in the lattice, and is considered as an α-stabilizer. A blue layer on the titanium is typical due to some oxidation, and is not considered to degrade the properties [11]. When the surface gets a brown color, the oxidation is more severe and it's likely that the properties of the titanium have been altered. Oxygen will at relatively high levels lead to embrittlement, while intermediate values will give a contribution to strength through solid solution hardening. Oxygen is also known to reduce the solubility of aluminum, enhancing the likelihood of Ti_3Al precipitation formation [12]. Ti_3Al are known to form at holding times below 550°C, but are unfortunately hard to detect by EBSD and will not be studied any further in this work [9].

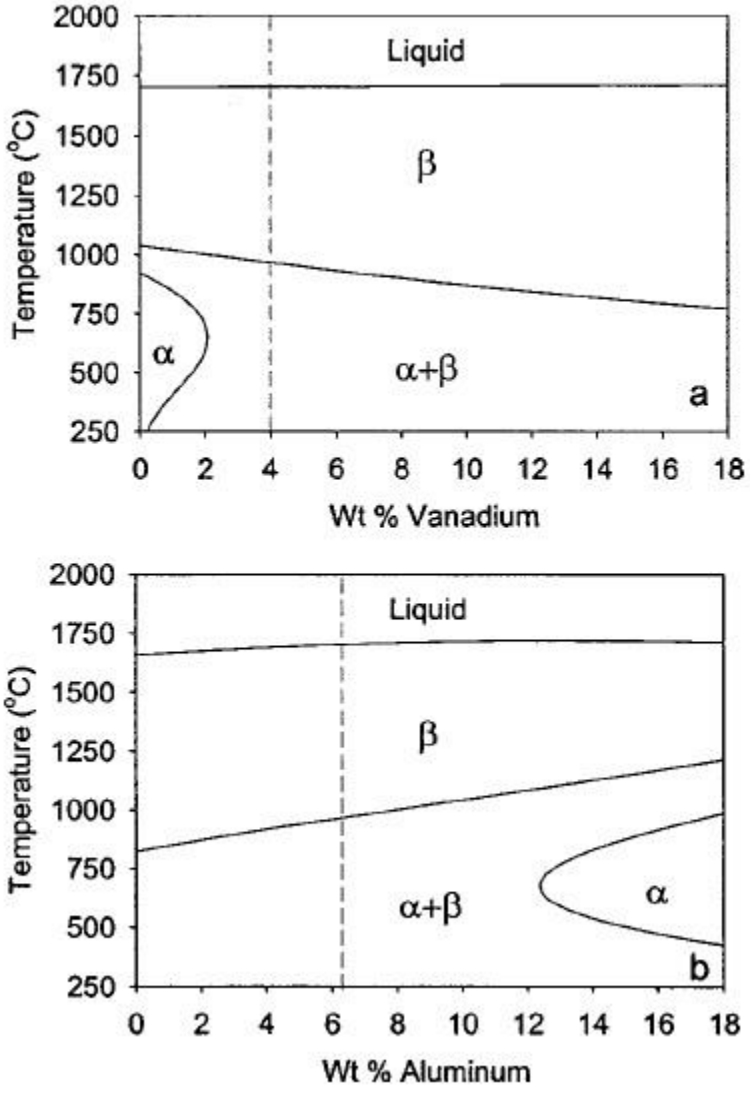

Figure 4: Pseudo-binary phase diagram for Ti-6Al-4V. Top: Vanadium content in Ti-6Al. Bottom: Aluminum content in Ti-4V [13]

2.3 Phase Transformation

There are two main phase transformations for titanium. The first occur when the liquid metal reaches the liquidus temperature and the titanium starts to solidify, and is completed when the alloy reaches the solvus temperature. The second phase transformation is an allotropic phase transformation (section 2.1) at the transus temperature, when the β-phase starts to transforms into the α-phase. The β → α transformation can give a large number of different microstructures depending on the cooling rate.

The AM process for titanium can be considered as a combination of welding and casting. The process is characterized by heterogeneous nucleation, as well as a directional and rapid solidification [5]. The liquid metal is added in strings of molten titanium into the desired geometry. The heat from the plasma arc will be used for melting the wire into droplets that is deposited on the end product. In addition some energy will cause re-melting of the material at the surface. The material that doesn't melt will still experience a heat input from of the plasma arc and the deposited droplets, leading to heat affected zones similar to conventional welding. The as-deposited alloy will therefore exhibit a microstructure with similarities to both cast and welding products, as the material is taken through the $\beta \rightarrow \alpha \rightarrow \beta$ transformation several times.

2.3.1 Solidification

Metals will have a tendency to grow in a direction with good heat transfer, which for titanium corresponds to $<100>_{\beta}$ [14]. In conventional welding the initial stages for growth is considered to be epitaxial, i.e. the solid metal at the fusion line act as nuclei and the new β grains grows with an orientation similar to the already solidified metal, as observed by Elmer, J.W., et al. [13] for epitaxial growth from large HAZ grains. As the workpiece operates as a heat sink ,the formation of small β grains will occur close to the substrate plate due to rapid solidification. When increasing the distance from the substrate plate grains with a columnar morphology will appear, growing parallel with the direction of the highest temperature gradient.

For the AM process it's likely to assume that most of the heat transfer occurs through solid metal [15], and one can therefore state that the heat flow is opposite to the growth direction parallel to the z (build)-axis [16]. The columnar grains are a typical AM feature and is caused by partial re-melting of uppermost material, before the re-melted material solidifies again according to an equiaxed growth mechanism. The numerous heat passes causes the columnar grains to grow in the build direction, but due to the moving torch imposing a temperature gradient in the deposition direction, the grains will be slightly tilted in the direction of the moving torch (Figure 5).

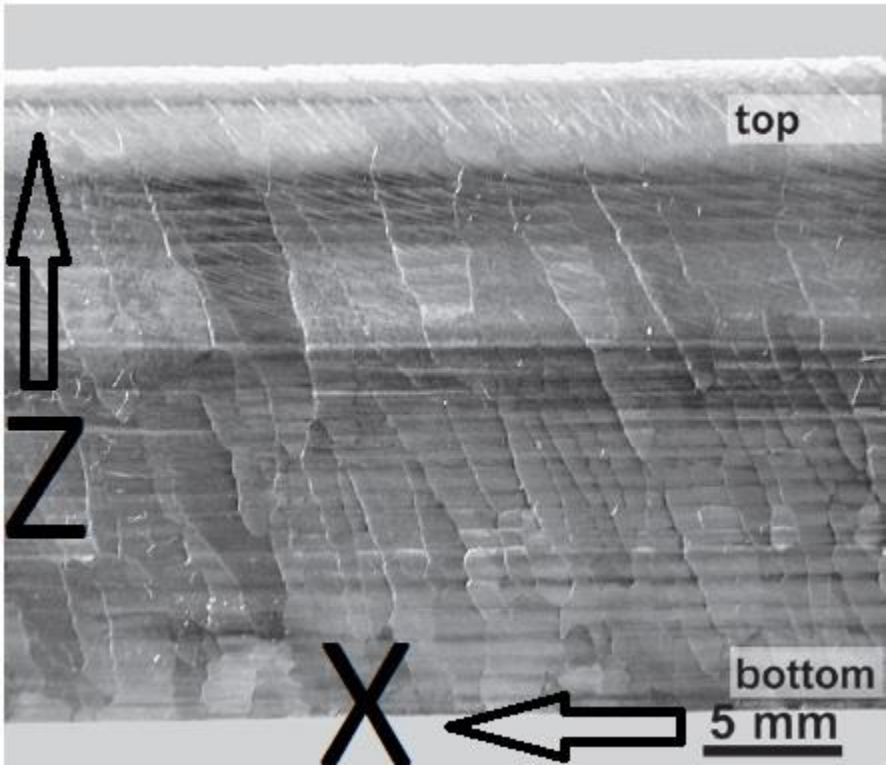

Figure 5: Showing largely elongated β-grains produced by AM. The grains have grown epitaxial in the build direction, and are as a result slightly inclined in the deposit direction due to the thermal gradient imposed by the moving torch [17]

As an alloy solidifies and the temperature decreases, the solubility of the elements such as aluminum and vanadium decreases. These elements are being rejected from the solid into the liquid metal, which in turn leads to a decrease in the solidus temperature. This phenomenon is called constitutional undercooling, which means that the molten zone ahead of the solid interface has a lower solidification temperature then the local equilibrium solidification temperature [16]. As the constitutional undercooling increases, the growth morphology goes from planar interface via cellular to dendritic. Because of the cooling rates related to AM it's not likely that there will be any planar growth. Elmer J. W. et al. [18] did report dendritic growth in Ti-6Al-4V at cooling rates of 150°C/s, although these were not present at room temperature due to the relatively high solubility of alloy elements and the lack of segregated phases.

2.3.2 Solid State Transformation

Upon cooling from the transus temperature, titanium will gradually transform from the initial open BCC structure towards a HCP structure. For α/β alloys, such as Ti-6Al-4V, the amount of α

and β at room temperature can be altered by heat treatments as well as the cooling rates. The final result after the heat treatment will however also depends on the thermal history of the titanium. Burgers, W.G. [19] stated that there's an orientation relationship in solid state phase transformation between the high temperature β-phase and the new stable α-phase. It was shown that the orientation of the α-phase would depend on the solidification structure of the β-phase. Even though the work was performed for zirconium, this relationship has proven to be true for titanium as well.

Titanium will generally grow in the $< 11\bar{2}0 >$ direction lying in the basal plane {0001}, as these have the highest thermal conductivity [20]. When Ti-6Al-4V is cooled below the transus temperature α-phase will start to transform, by growth along the $(0001)_\alpha$ forming colonies of thin plates or lamellae into the β-grains in the $(110)_\beta$ plane in the $<111>_\beta$ direction (Figure 6). As α-growth will depend on the initial β orientation it's possible to predict approximately how the solidification took place, as the high temperature β leaves a clear signature on the α texture [21].

The Burgers orientation relationship (BOR) can occur for both diffusion controlled and martensitic transformation [2]. It states that the BCC lattice can transform into twelve different hexagonal variants, with different orientations shown below.

$$(110)_\beta \leftrightarrow (0001)_\alpha \qquad 2.$$
$$< 1\bar{1}1 >_\beta \leftrightarrow < 11\bar{2}0 >_\alpha$$

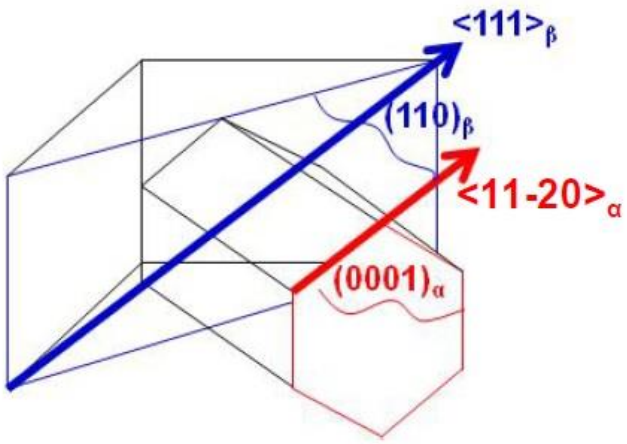

Figure 6: The Burgers orientation relationship between the α and the β-phase, where $<111>_\beta(110)_\beta||<11\text{-}20>_\alpha(0001)_\alpha$. These type of relationship is unique, and only seen in a few metals with HCP structure [22].

There are two $<111>_\beta$ (b1 and b2 direction) directions in the $\{110\}_\beta$ plane, but only one of the three $< 11\bar{2}0 >$ (a1, a2 and a3 direction) directions in the basal (0001) plane can align itself with one of the $<111>_\beta$ directions. For geometrical reasons this means that if a1||b1, there will be a 10,5° misorientation between a2 and b2 (Figure 7), while a3 will be largely misaligned [23]. This relationship has a large effect on the slip transfer between α and β phase.

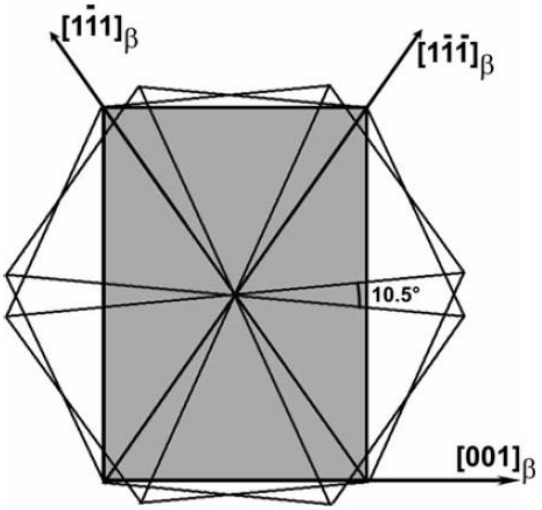

Figure 7: Two variants of hexagon orientation following BOR, showing the misalignment that occur during phase transformation between the HCP and BCC lattice [23]

2.3.2.1 Diffusional growth

When the cooling commences, the α-phase will nucleate at the β grain boundaries as incoherent layers. By continue to cool down, the α-phase will eventually start to grow as parallel plates called α-colonies, into the β grain. These α-colonies consist of fine lamellas, separated by the β-phase. The lamellas will grow inwards from the β-grain exterior, without crossing any of the boundaries [24]. At continued cooling the characteristic basket weave or Widmanstätten structure will start to form, as the colonies themselves can't fill the entire prior β-grain. The lamellas will grow in one of the 12 Burger's variants (Figure 8) until it encounters another colony with a different variant. Even though the β-phase in theory can transform into 12 different α-orientations, there tends to be a variant selection to certain orientations, i.e. certain orientations are preferred over others. The degree of variant selection depends on the chemical force (supersaturation), which can be altered by both grain size and cooling rate [25]. A high supersaturation related to a high cooling rate will decrease the variant selection, and thus give a higher amount of differently oriented α-phase.

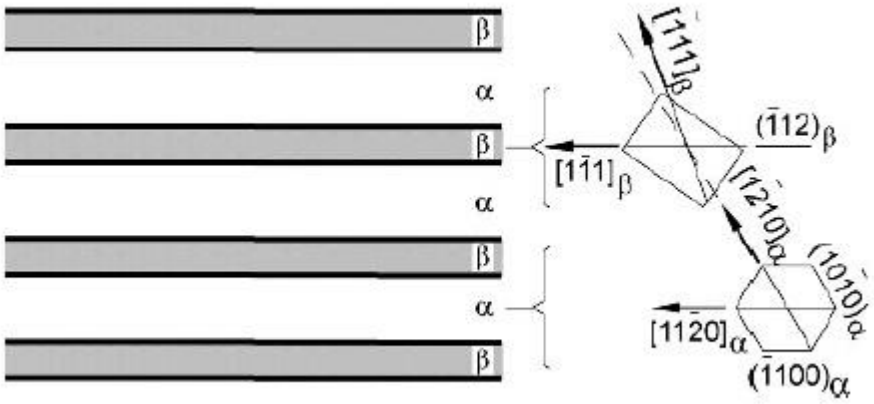

Figure 8: Schematic representation of the growth mechanism for the α-lamellae in the β-phase, applying BOR [2]

2.3.2.2 Martensite

β-phase can be transformed into martensite by quenching, or by mechanical stress/strain at room temperature. The martensite transformation is a cooperative movement of atoms by shear resulting in a homogenous transformation from BCC to HCP, and can be extremely fast, reaching the speed of sound. The crystal structure of α-phase and martensite (α') is very similar, making

them hard to distinguish. Martensite in titanium cab also exxhibit an orthorhombic (α'') structure, given the right alloy composition and atmospheric pressure [2]. To complete the martensitic transformation there have to be a displacement of alternate atomic layers as well as a homogenous volume change of the lattice. For a full explanation of the martensitic transformation, the reader is referred to [19].

Eventually the {0001}-plane in the HCP will end up being parallel to the {110}-plane in the BCC, as well as one of the $[11\bar{2}0]$-directions being parallel to the [111]-directions in the {110}-plane. The BCC lattice has, as mentioned, six {110}-planes and two [111]-directions, this gives rise to twelve different martensitic variants.

2.4 Microstructure

The microstructural evolution during AM is a rather complex combination of solidification, thermal kinetics and cycling, as well as phase transformations [26]. When in equilibrium the commercially pure (CP) titanium has 100% of the α-phase at room temperature. The β-phase doesn't usually become present until the temperature is increased. For the AM produced Ti-6Al-4V, there's almost no β-phase observed at room temperature [9]. On the basis of these two phases, there are several morphologies that can be present at room temperature, such as martensite and the Wiedmanstätten structure.

When cooling from the β region the cooling rate is the determining parameter for the microstructure. As there is extensive grain growth when operating above the transus temperature, the time the alloy experience in the β-region is a crucial parameter [27]. While cooling from α/β-region, the peak temperature is the main parameter controlling the microstructure. The time plays a minor role, but becomes increasingly more important as the temperature increases towards the transus temperature. This is because the grain growth in the α/β region is limited. Even though both phases will tend to grow, they are restricted heavily by each other [27]. The α-phase will start to coarsen during heat treatment in the α/β-region, and even globularize when given enough time [27]. The work performed by Ivasishin et. al. [28] states that β grows discontinuous when there's a strong textured α present. By longer annealing times the growth rate will increase, as the texture decreases.

Upon reaching the transus temperature during coolong, a continuous α-layer will start forming at the β grain boundaries. The thickness of the grain boundary α increases as the cooling rate decreases. The grain boundary α doesn't follow the orientation relationship (section 2.3.2) in the same ways as the material in the grain interior, but rather makes a compromise of the orientation of the two neighboring β-grains [23]. There will therefore be a somewhat gradual misorientation across the boundaries, making the slip transfer across them rather hard.

Eventually, growth into the β grain will occur in the form of parallel plates (Figure 9) growing from α-regions at the grain boundaries, forming so called α-colonies. The α-plates will grow until they encounter plates that have grown from other regions of the β interface with another variant of BOR. In between these α-plates there will be retained β-phase from the matrix, which often are incorrectly referred to as β-plates [2]. The content of aluminum decreases from the center of the plates towards the β-phase, as it is an α-stabilizer. The vanadium content will however increase in the same direction [29], as it works as a β stabilizer.

Towards the center one usually observe Widmanstätten colonies [11], caused by a somewhat higher driving force where the colonies cannot fill the interior all by itself. The α-Widmanstätten will start to nucleate at points on existing α-lamellae and grow perpendicular to these interfaces. This gives the characteristic *basketweave* structure. Both colony and Widmanstätten α are chategorized as primary alpha α_p. During heat treatments in the α/β-region, the β will increase its concentration of Al (α-stabilizator) and decrease its concentration of V (β-stabilizator) [30]. During cooling some of the β will transform back into α_p, as a result of grain growth. But some of the β-phase will form secondary alpha (α_s), with a somewhat similar orientation as the α_p. The α_s does however has a finer lamellar structure than the α_p.

Grain boundaries works as a highway for diffusion, so an increased grain size will cause the diffusivity of the α-stabilizers to decrease, consequently the β-grain will become more stable as the size increases. Large (columnar) β-grains causes the transus temperature to decrease, leading to thinner Widmanstätten lamellae [29], as the undercooling becomes high before any phase transition takes place.

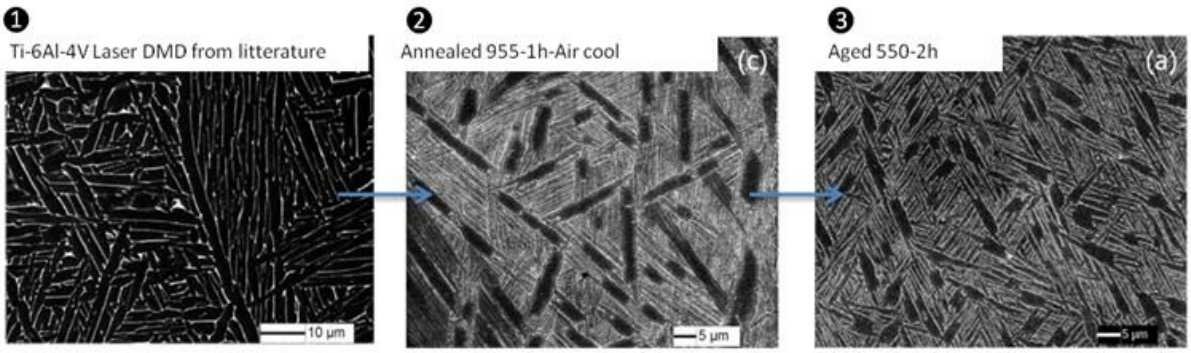

Figure 9: Example of Ti-6Al-4V microstructure. 1: As deposited lamellar structure. 2: After annealing. 3: After aging [31]

By increasing the cooling rate, the formation of α' (section 2.3.2.2) will eventually take place. In comparison to martensite in steel the martensitic transformation in titanium exhibits a crystal structure equal to the equilibrium phase (α-HCP), although with a slightly different lattice parameter [13]. Martensite grows from the retained β, via a diffusionless process. α' has a very fine characteristic needle structure, and grows fast when the M_s-temperature is exceeded. The starting temperature for martensitic formation are around 850°C [2], and a cooling rate of about 410K/s is required [26] to keep the process running. Annealing the titanium at a temperature between 700°C and 850°C will dissolve the martensite, turning it into fine lamellar α/β structure [32]. As compared to a ferrous system the driving force for martensitic transformation is much lower, due to a lower shear modulus at the transus temperature, and less inhomogeneous strain due to the crystallographic relation to the parent phase [14].

A unique microstructure that can be obtained from the lamella microstructure is the so-called crab-like primary α. This microstructure is a result of a heat treatment in the upper part of the α/β phase region. During the heat treatment, the α/β grain boundaries will be enriched by α-stabilizing elements (Al). As these grain boundaries are incoherent and therefore possess a high interfacial energy, nucleation of secondary alpha is beneficial [33]. The α_s will grow on the edge of α_p in the <1120> crystallographic direction by a diffusive decomposition process. The formation of the crab-like morphology is very sensitive to temperature, and has only been observed for air cooled samples.

2.5 Deformation and slip systems

Deformation in CP titanium and α-titanium is a combination of twinning and conventional dislocation slip in the prismatic and basal plane. In Ti-6Al-4V the twinning mechanism is nearly fully suppressed by relatively small phase dimensions and high aluminium content, and twinning is therefore not expected in Ti-6Al-4V, unless extreme deformation conditions are imposed [34].

2.5.1 Single grain deformation

The HCP structure is associated with a low ductility due to few slip planes. The c/a-ratio in α-titanium is however lower than the ideal ratio (1,587 instead of 1,633), leading to a closer packing of both prismatic and pyramidal planes. Thus, slip in both the close packed basal plane, the prismatic and pyramidal planes will occur more easily.

Following the principle that slip occurs in the most densely packed directions, slip will be limited to the three close-packed directions of <$11\bar{2}0$> (the basal $\vec{a}$ Burgers vector). The three planes containing these directions is the basal plane (0001), the $\{10\bar{1}0\}$ prismatic planes and the $\{10\bar{1}1\}$ pyramidal planes (Figure 10). This gives a total of three independent slip systems.

By assuming that von Mises criterion for homogenous deformation can be applied, five slip systems must be activated. This means that two additional slip systems not containing a pure basal Burgers vector ($\vec{a}$ Burgers vector) has to be active. Slip in the $\vec{c}$+$\vec{a}$ slip system can occur in the first order pyramidal $\{10\bar{1}1\}< 11\bar{2}3 >$ and second order pyramidal $\{11\bar{2}2\} < 11\bar{2}3 >$ slip system [22]. The critical resolved shear stress (CRSS) in the α-phase is however significantly higher for $\vec{c}$+$\vec{a}$ slip than for $\vec{a}$ slip, so in polycrystalline α-titanium the $\vec{a}$ slip is activated much easier with respect to $\vec{c}$+$\vec{a}$. The primary deformation mode for titanium is prismatic slip system [35] due to a decreased c/a-ratio compared to an ideal HCP-crystal, exhibiting a much coarser slip than the basal slip [36]. Addition of aluminum (above 6%) will however increase the prismatic CRSS, thus making basal slip more favorable [36].

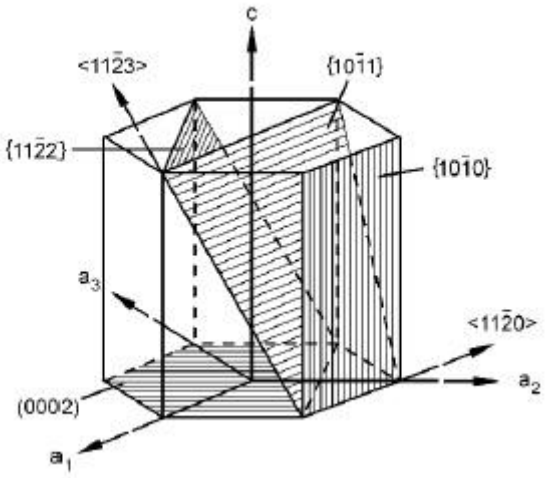

Figure 10: Illustration showing the α-Ti HCP structure, and its accompanying slip systems. The prismatic and basal are the most active slip systems, due to their low CRSS value relative to the 1st and 2nd order pyramical slip [2]

2.5.2 The Schmid factor

By considering a uniaxial tensile load on a rod of Ti-6Al-4V the critical resolved shear stress of a grain can be determined by applying the method from Schmid (Figure 11). For slip to occur the resolved shear stress on the plane (τ_R) have to be larger, or equal to the CRSS.

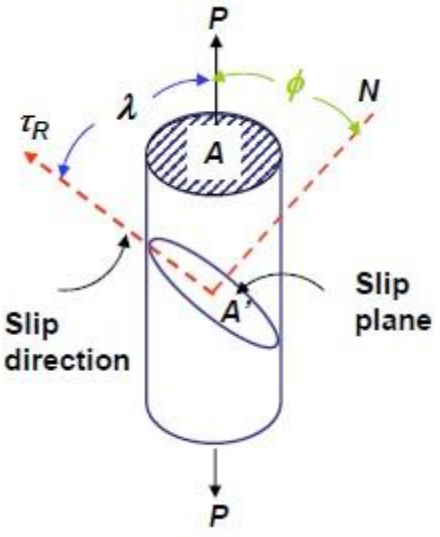

Figure 11: Schematic illustration for the parameters involved to calculate the resolved shear stress by the Schmid factor [37]

The calculation of the resolved shear stress on a slip system is as follows:

$$\tau_R = \sigma \cos(\lambda) \cos(\varphi) \quad 3.$$

Where σ is the stress applied, φ is the angle between the applied force (P) and the normal to the slip plane, λ is the angle between P and the slip direction (Figure 11). The $\cos(\lambda)\cos(\varphi)$ term is named the Schmid factor, and is related to orientation of a specific slip system relative to the applied load in an uniaxial stress-state. The Schmid factor gives a good indication of how easy a specific slip system can be activated, the higher the Schmid factor the easier the activation of the slip system is.

By equation 3 it is seen that if the applied stress is normal or perpendicular to the slip plane, i.e. φ=0° and λ=90° or vice versa the resolved shear stress will be zero. This is the same state as where the stress axis is parallel to c-axis. The deformation involving an $\vec{a}$ Burgers vector is more or less impossible with this orientation and the surrounding grains will have to carry the load. Due to inhomogeneity in the AM-produced titanium, this may lead to fracture rather than slip [9]. This combination of a grain unwilling to deform, sharing a grain boundary with a grain more susceptible to deformation, is called a rogue grain [38], or hard-soft grain combination. The Schmid's factor can give a good indication for the behavior of slip systems in HCP polycrystals. It does however not give a clear indication for whether or not the slip system actually will be activated [36].

2.5.3 The Young's modulus

According to the work of Bridier, F. et al. [39] the Schmid factor was insufficient to show the deformation in Ti-6Al-4V alone. Other parameters in addition to the Schmid factor had to be considered, to describe the deformation mechanisms of the material. The E-module of the HCP crystal is considered one of these factors [39]. The HCP lattice is anisotropic, as can be seen in Figure 12 the Young's module depends on its orientation relative to the stress axis. A grain with a low stiffness will easier be deformed than a grain with a high stiffness, given they have the same tendency towards slip.

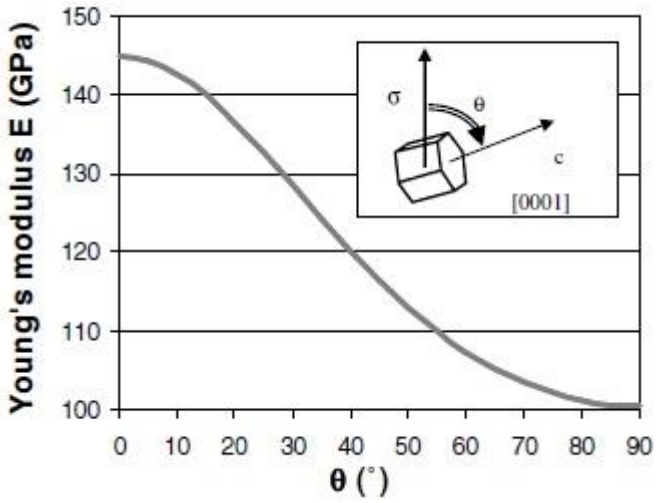

Figure 12: Showing the theoretical Young's modulus of the HCP crystal of Ti-6Al-4V depending on its orientation with the stress. The maximum value is when c || σ (145 GPa), while the minimum is observed when c is perpendicular to the stress (100 GPa) [39]

2.5.4 Polycrystalline deformation

The α-colony in Ti-6Al-4V can be considered as a grain, since the lamellas inside each colony have a similar orientation, making slip transfer inside the colony rather easy. A coarse lamellae structure will increase the ductility [40], as the advancing crack isn't arrested by a boundary to a new lamellae. Even with β-phase in-between the α-lamellae the slip can propagate through the entire colony as discontinuous lines. Slip might however also be unable to move through the colony due to misorientation [22], recalling the alignment of the b1 , b2, a1, a2 and a3 directions mentioned in section 2.3.2. For slip to occur from one colony to another, the orientation of both colonies need to be aligned so that slip in the same system is promoted. The boundary between colonies are however often observed as significant obstacles for advancing cracks [41].

Material produced by AM will exhibit anisotropy, the degree of it depends on several parameters such as cooling rate and interpass temperature. The lamellar microstructure combined with BOR and a HCP structure will lead to a rather complex grain-to-grain interaction, which can make stress-strain calculations rather complicated. By considering a grain (or colony) having its c-axis close to parallel with the tensile direction, the Schmid factor will be low and the grain will be more or less unable to deform. The strain will therefore have to be accommodated for by neighboring grains that exhibit a higher Schmid factor [42], which naturally gives an inhomogeneous strain

distribution. As the material is inhomogeneous, the accumulation of strain to the neighboring grains can lead to very concentrated deformation, and eventually crack formation.

The prior grain boundaries of the old β-phase are considered to play a crucial role in deformation of the material. The grain boundary α (section 2.4) has a very soft behavior, and would therefore deform more easily than the interior of the prior β-grains. Slip from colonies could transfer to the β-grain boundary, but due to the large misalignment with the neighbor β-grain the strain will not be able to travel any further [22]. The slip will accumulate inside the grain boundary α, and lead to the formation of cracks at a relatively early stage.

2.5.5 Deformation in the AM material

Due to the nature of the AM process, it's unlikely that the as-cast AM product will show isotropic behaviour. Baufeld, B. and O. van der Biest [17] showed that the strength in the x-direction is somewhat higher than in the z-direction. Whereas, the ductility is significantly larger in the z-direction compared to the x-direction

The AM product contains remnants of the columnar β-grains (Figure 5) in the z-direction, as α will form easily at these boundaries. The thickness of α at the grain boundary affects the ductility, the thicker the α is, the lower the ductility [34]. The z-direction will contain much less grain boundaries compared the x-direction, which in turn decreases the strength. However, as grain boundary α often are sources for failure, the ductility will decrease in the deposition direction. The material at the bottom will have experienced several heat cycles and is therefore expected to have a coarser microstructure, which in turn will increase the ductility. The material further up in the build direction will have undergone less weld passes, leaving a finer lamellae structure with a higher strength and lower ductility. It's been observed that the strength is hardly altered during heat treatments, while the strain is significantly changed [5]. With the correct form of heat treatment, the material can eventually obtain properties equal to wrought products.

Titanium has a low workability, which will result in rapid formation of microvoids during deformation. Microvoids are known to initiate at α/β interfaces, so a low aspect ratio of the lamellae is not favorable when it comes to ductility [43]. Baufeld, B. and O. van der Biest [17] proposed that the ultimate tensile strength was inversely proportional with the α-lath width.

Cavitation will easily occur when two neighboring grains have c-axis close to perpendicular to each other. A low ductility could also be caused by the presence of Ti_3Al, which could be precipitated due to slow cooling from its solvus temperature (550°C) [30].

2.6 Electron backscatter diffraction

Electron backscatter diffraction (EBSD) is a technique used in the scanning electron microscopy (SEM). SEM is a microscope that in many ways work as the conventional light microscope, but instead of light this microscope uses accelerated electrons which gives a much higher resolution at higher magnification. For more information about SEM the reader is referred to [44].

A high energy current is bombarded unto a tilted specimen surface, which is diffracted by Bragg's diffraction to a phosphor screen with a digital camera behind it. These diffraction bands are called Kikuchi diffraction. Bragg's law is given as:

$$n\lambda = 2d\,sin(\theta) \qquad 4.$$

Where n is the order of diffraction, λ is the wavelength of the electrons, d is the atomic spacing of the material fulfilling Bragg's law and θ is the angle the electron beam form with the plane of the diffracting lattice.

EBSD is an extremely powerful tool for analyzing microstructure, texture, grain boundaries and phases. The sample preparation for EBSD is however extremely crucial. The surface of the sample should be more or less deformation free, as the signals from the sample origin no longer than 50nm from the surface. A deformed surface will give misorientation of the lattice, making the diffracted patterns from the sample hard to characterize.

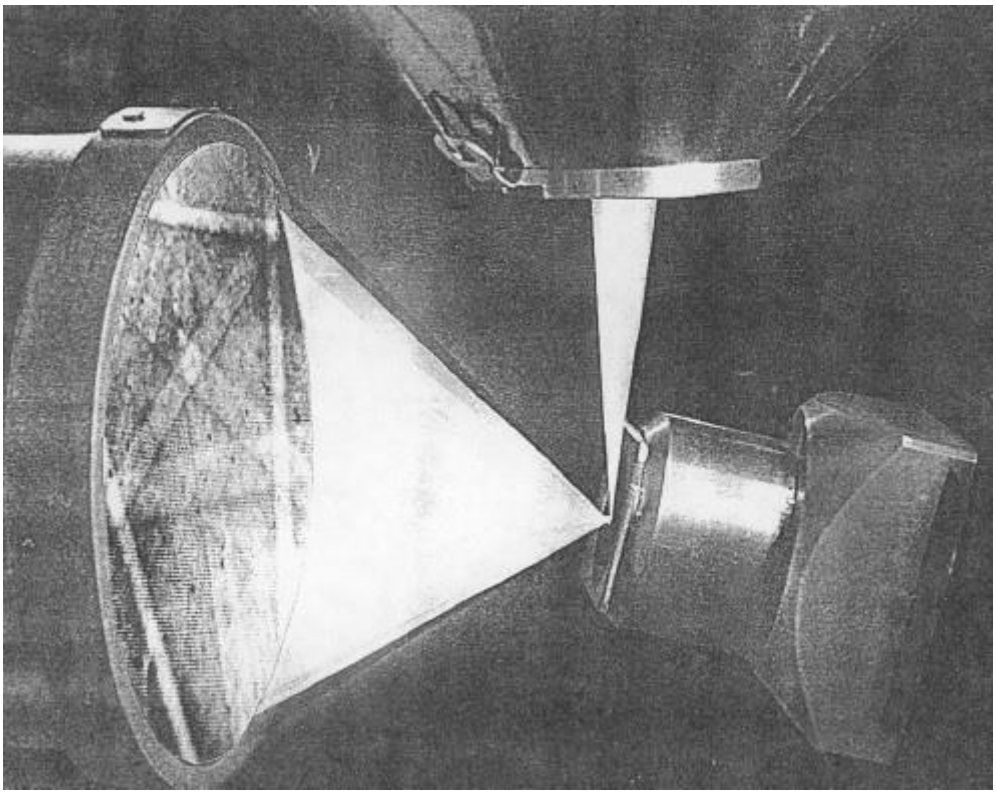

Figure 13: Set up for EBSD. The electron beam (top) hits the tilted specimen (right). Backscattered electrons are then diffracted onto the phosphorus screen (to the left) giving a diffraction pattern characteristic for the phase and the orientation of the material being studied [45]

To obtain a sufficiently good signal a large aperture opening is used. This allows a higher amount of electrons in the beam, but also broadens the electron beam leading to a higher signal/noise-ratio which gives a somewhat lower resolution. By tilting of the sample (Figure 13), the amount of backscattered diffracted electrons increases, and thus giving a better diffraction pattern.

The diffracted electrons form patterns on the phosphorous screen that is captured by the camera, stored on the hard disk, and prosessed at a later stage. This type of EBSD treatment of data is called offline EBSD. As the electron beam moves over the specimen surface, each phase and orientation will give a unique diffraction pattern (Figure 14). The diffraction patterns contain a very high amount of information, and by the use of a software one can obtain information such as texture, phase distribution and high and low angle boundaries. The software used for indexing the diffraction patterns is OIM Analysis 6.1, produced by EDAX. EDAX have patented the term confidence index (CI), which is a value for how reliable the diffraction pattern is. From earlier research the CI index for Ti-6Al-4V produced by AM should be equal or higher than 0.3 [9]. The

fit-value is related the angular fit between the obtained diffraction pattern, and the one stored in the database. A fit-value below 1° is considered a good value.

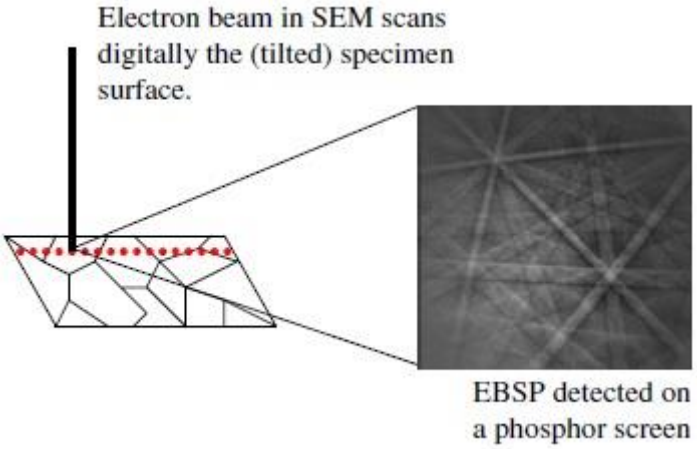

Figure 14: Schematic illustration showing how the offline EBSD collects data. For each point a diffraction pattern is obtained and stored on the hard-drive, and will be indexed at a later stage [45].

2.7 Texture Analysis

Evolution of hexagonal texture has not until recently been an area of interest, as compared to FCC and BCC materials. As a result of this there are a limited amount of information available related to hexagonal texture [35].

The texture change in hexagonal structures will be affected by both its initial texture, as well as the c/a-ratio. There are several ways of representing crystallographic texture, both graphically and by use of different reference frames. In general, orientation can be defined as how atomic planes choose to place themselves in a volume relative to a fixed reference. Texture is defined as a preferred orientation of the material, and can highly affect the properties such as strength and ductility.

For graphical representation from (3D to 2D) of texture plot orientation, projected poles using stereographic projection are common. When a crystal structure has a center of symmetry, meaning (x,y,z) = (-x,-y,-z), it becomes hard to distinguish point groups. This is because diffraction patterns always will be centrosymmetric, which only makes it possible to distinguish between the various centrosymmetric crystal classes [46]. This classification is called Laue classes.

2.7.1 The Pole Figure

The pole figure uses the crystal orientation in the external coordinate system, usually the specimen coordinate system. By assuming a crystal inside a reference sphere, one can obtain a pole by obtaining the normal of the lattice plane on the sphere (Figure 15). By then drawing the lines from each pole to the south pole of the sphere, the intersection with the equatorial plane will be the poles obtained in the pole figure, which will give a 2D representation of the orientation. A material without crystallographic texture has projection points scattered all over the projection plane. In a material with a distinct crystallographic texture the poles will tend to cluster, and form specific patterns.

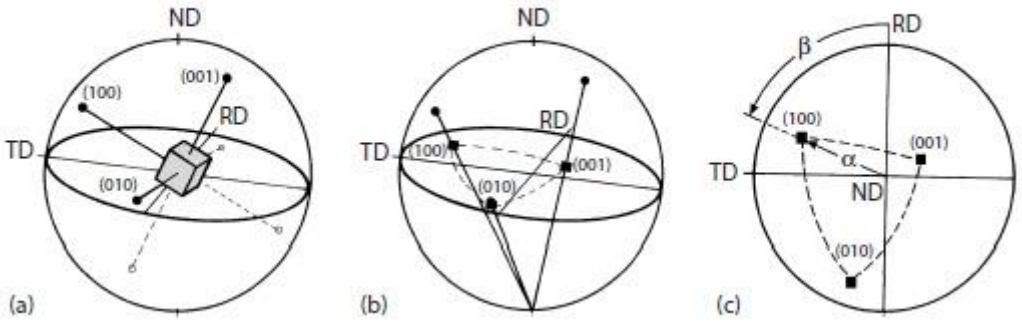

Figure 15: Illustration of stereographic projection of the {100} poles from a cubic crystal. (a): Place the crystal in the unit sphere. (b): Moving the lattice to the south pole, and set the projections on the equator plane. (c): The final {100} pole figure[46]

A typical way to illustrate texture in pole figures is by using contour levels that show the distribution of texture, instead of using points. This is especially useful in polycrystals, when the number of points in a pole figure could make the figure very hard to read.

2.7.2 The inverse pole figure

The inverse pole figure (IPF) uses the specimen coordinates inside a crystal coordinate system, i.e. the inverse of the pole figure. The directions plotted in the figure, are directions parallel to one of the specimen coordinates (x,y,z or rolling-, transverse-, normal direction). Due to symmetry of the Laue class, one only need one out the twelve equivalent stereographic triangles (Figure 16) to make an inverse pole figure. By defining a reference direction grains can receive their color relative to the direction, and their orientation.

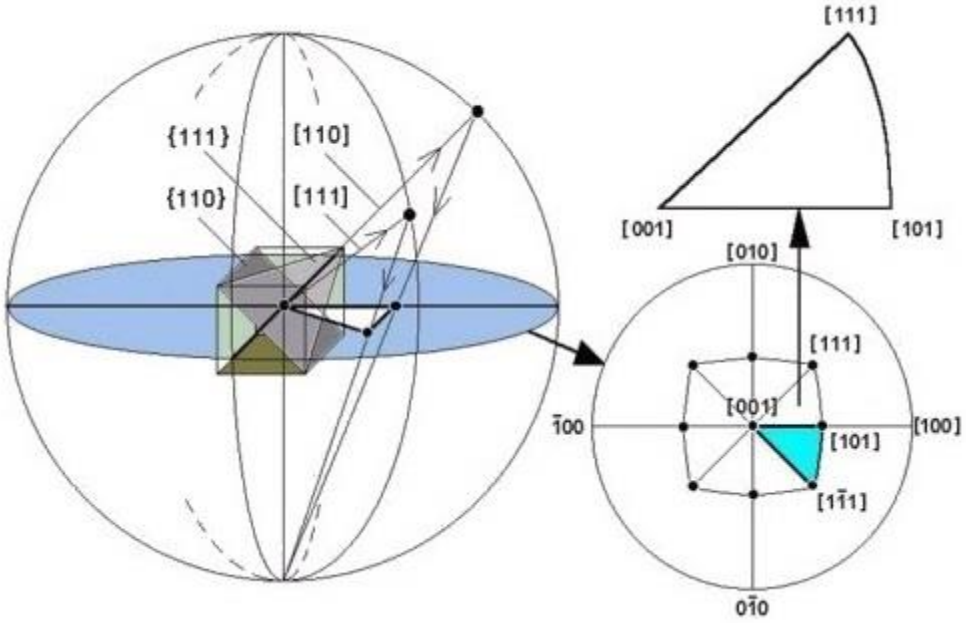

Figure 16: Schematic illustration showing how the inverse pole figure is extracted from the conventional pole figure, using a cubic crystal structure[47].

3. Experimental

In this section the material studied will be presented, in addition to a thoroughly explanation of the sample preparation, heat treatment procedures, the thermodynamical experiments (dilatometry) in addition to the set-up and parameters used for in-situ tensile testing with EBSD. A simplified chart of the expermintal process is seen in Appendix A.

3.1 Sample preparation

Samples delivered from NTi came in “strips” with different sizes and geometries, extracted from blocks of AM produced Ti-6Al-4V. The blocks (Figure 17) being orthorhombic, had geometry of x=200mm, y=120mm and z=100mm. The material delivered had not been through any heat treatment except stress annealing at 700°C for 2 hours.

3.1.1 Samples

The samples examined were extracted from Z5 and Z6, i.e. relatively close to the substrate plate (Figure 17). The reason for choosing material close to the deposition plate is the thermal history experienced towards the bottom, and the desire to study the response of this material. The “strips” had different geometry given in Table 1.

X-direction [mm]	Y-direction [mm]	Z-direction [mm]
70-130	10-15	15-25

Table 1: The geometry of the strips extracted from the deposited material

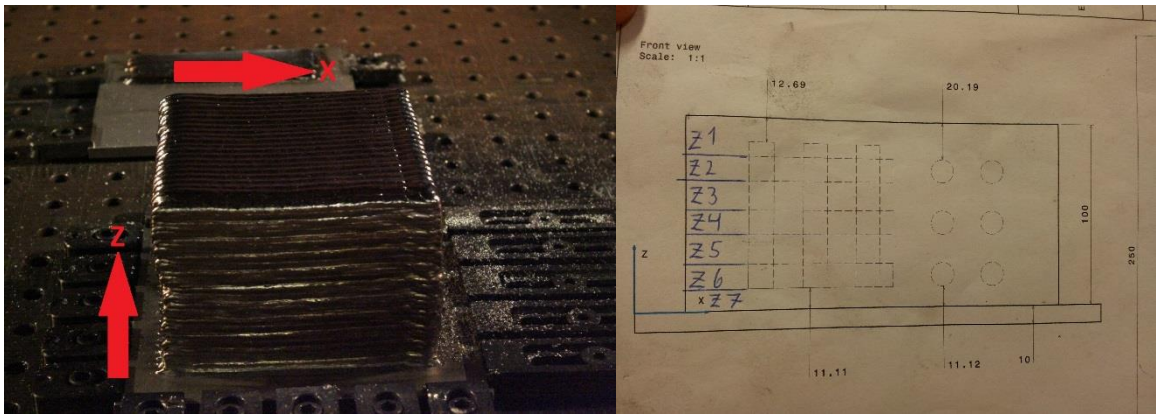

Figure 17: <u>Left:</u> The block. X – deposition direction, Z – build direction. Y – transverse direction. <u>Right:</u> Showing the sectioning of the block in the build direction. Z1 is at the top, while Z7 is right above the substrate plate

For extracting the tensile specimen geometry needed for in-situ tensile testing in SEM, the strips of material were sent to Nomek Ranheim for spark cutting. The plane studied were the z/x-plane as this will contain a high amount of columnar prior β-grains, which is thought to be of importance when it comes to deformation. The geometry of the sample is given by Figure 18, with a thickness of 1,1 mm. It is assumed that the thickness will be reduced to approximately 1 mm after grinding and polishing.

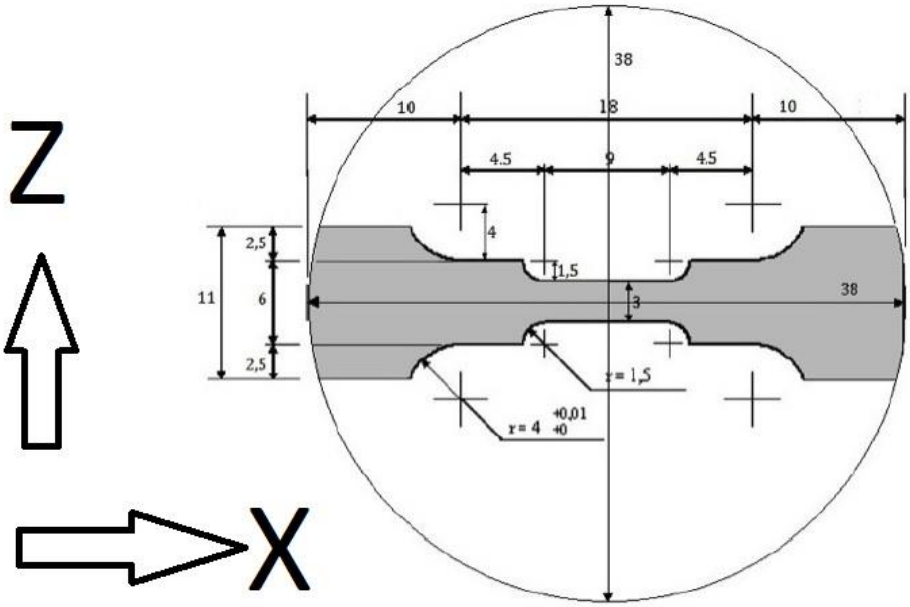

Figure 18: The geometry of the samples used for in-situ tensile test in the SEM, with a thickness of 1,1mm. The orientation of the axis is given to the left

3.1.2 Mechanical grinding

The grinding and polishing is done to obtain a flat surface, as well as stepwise removing deformation layer. Each grinding step introduce some deformation, but by doing the grinding with a decreasing grit (finer surface/suspension) the deformation layer will gradually become thinner. The edges of the samples should be grinded by hand with the 80 SiC to remove some of the roughness on the surface that remains after spark cutting. The roughness (crevices and sharp edges) can initiate premature fracture during the tensile testing.

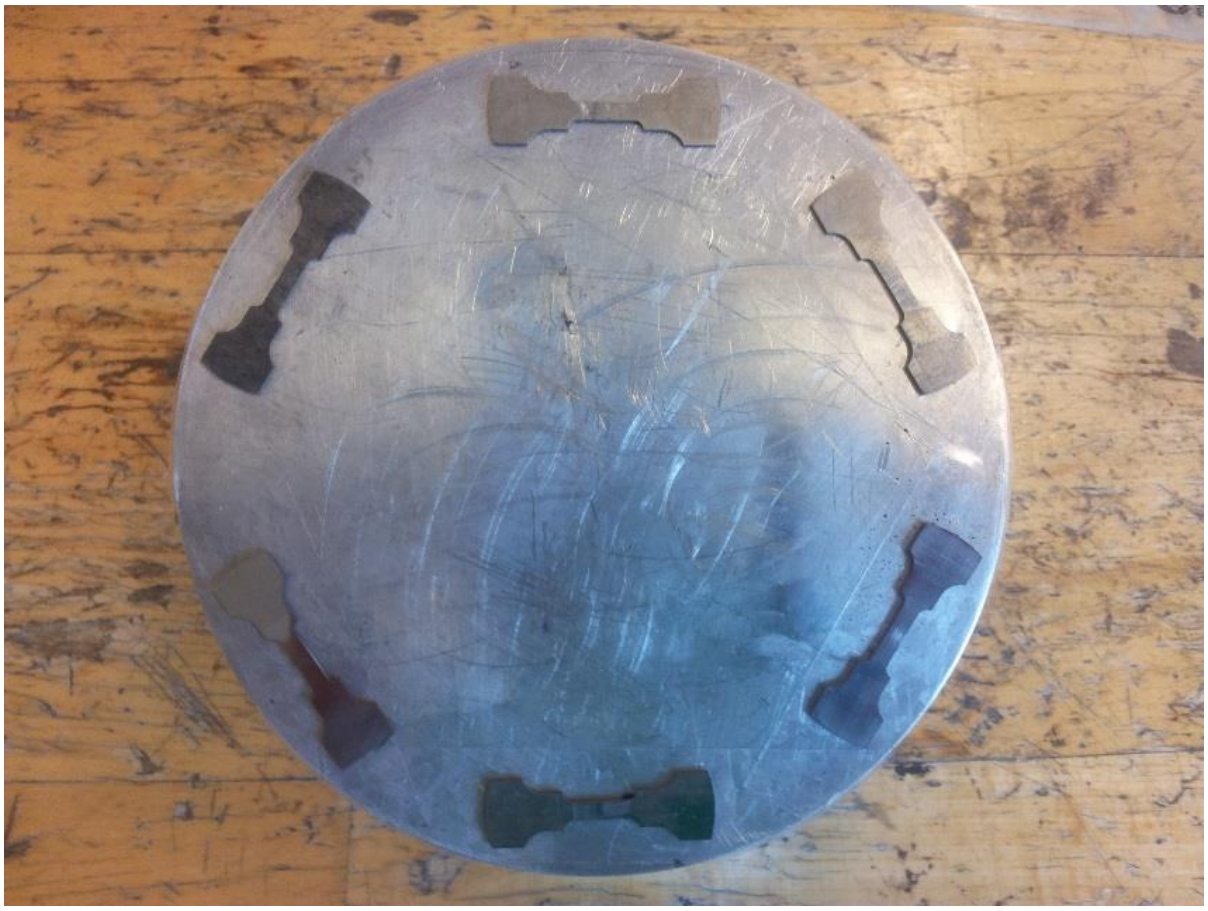

Figure 19: Showing a typical mounting of the tensile bars on the sample holder. The samples are oriented in the circumference direction, and is evenly distributed around the circumference to have the loading as even as possible on each sample.

The samples were mounted on a sample holder made of stainless steel with diameter of 14 cm and thickness 2 cm using a double sided tape into a Struers RotoPol-31 coupled with Struers RotoForce 4. The samples should be mounted in the circumference direction (Figure 19), and be aligned so that the force is evenly distributed. The samples should be mounted with 25N per

sample, and with 300rpm co rotation using 500 SiC paper and water as lubricant. The samples were usually level after 1 min of grinding. Force reduction should be used at the final step of each paper/surface, to reduce the deformation caused at the surface. The samples should be thoroughly cleaned in water and ethanol before changing surface/paper.

Further grinding is thereby done by Struers TegraPol-31, coupled up to TegraForce-5 and Tegra Doser-5, both from Stuers. MD Largo (Struers) 9µm Diapro was used as surface, and as suspension 9µm grit DP should be applied. The force used was 25N per sample with a 150rpm contra rotation. This should be done for 7-10 minutes, before cleaning the samples with water and ethanol.

Step	**Grinding Surface**	**Time**	**Force per sample**	**Rotation**	**Lubricant/ suspension**
1	80	Until edges are smooth	Manually	N/A	N/A
2	500 SiC	1 min	25N	300rpm. Co rotation	Water
3	MD Largo (Struers)	7-10 min	25N	150rpm. Contra rotation	9µm grit DP

Table 2: The mechanical grinding processes found to give the best results for Ti-6Al-4V in EBSD

3.1.3 Chemical-mechanical polishing

The final preparation surface is a MD chemical cloth, with an OPS and hydrogen peroxide mixture as suspension. OPS is an alcohol-silica suspension with a grit of 0,4µm. The OPS/H_20_2 mixture contains 10vol% of a 30% solution with hydrogen peroxide, while the OPS is diluted in water to a 10vol% solution. The H_20_2 is known to contribute to the removal of deformation layer during polishing of titanium.

Step	Grinding Surface	Time	Force per sample	Rotation	Lubricant/ suspension
1	MD chemical cloth (Struers)	15	15	150rpm. Contra rotation	OPS(90vol%)+ H_20_2(10vol%)
2	MD chemical cloth (Struers)	1	10	150rpm. Contra rotation	Water

Table 3: The chemical-mechanical polishing process found to give the best result for Ti-6Al-4V in EBSD

The force used was 15N, with 150rpm and contra rotation. After fifteen min, the OPS suspension was changed to water for one minute with decreasing force. After polishing, the samples were thoroughly cleaned in water and ethanol. The deformation layer of the samples should now have been more or less removed.

3.1.4 Sample cleansing

To remove particles and thin organic films that might have been accumulated on the surface, the samples were soaked into a bath of acetone in a Struers Metason 120 ultrasonic bath for ten minutes. The samples were then flushed in ethanol and dried. When the ethanol had evaporated the samples were put inserted in a Fischione Instruments Plasma Cleaner Model 1020 for 6min. The sample should go through the plasma cleaner step prior to the each insertion in SEM, as it removes any hydrocarbons that have contaminated the surface during the previous examination.

3.1.5 Etching

To investigate the 1st batch of samples after heat treatment more thoroughly, a parallel undergoing the same kind of treatment was initiated. After heat treatment and sample preparation, the samples were soaked in a Kroll's reagent (Table 4) for 14 seconds. The Kroll's reagent is known to be a good etch for investigating titanium as it highlights lamellas and other microstructural factors that often isn't visible in neither bright field microscope or SEM.

Water	HNO_3	HF
92 vol%	6 vol%	2 vol%

Table 4: Chemical composition of the Kroll's reagent used to etch the titanium samples

3.2 Solution annealing and aging

In order to improve ductility and homogeneity the material underwent a solution annealing and aging process. The heat treatment performed was based on similar treatments performed by NTi. The heat treatment (Figure 20) is divided in two parts; solution annealing and aging. The solution annealing was performed at 950°C for 1hours, while the aging was performed at 600°C for 2 hours. The focus for this heat treatment was mainly to see the effect of cooling rate after solution annealing.

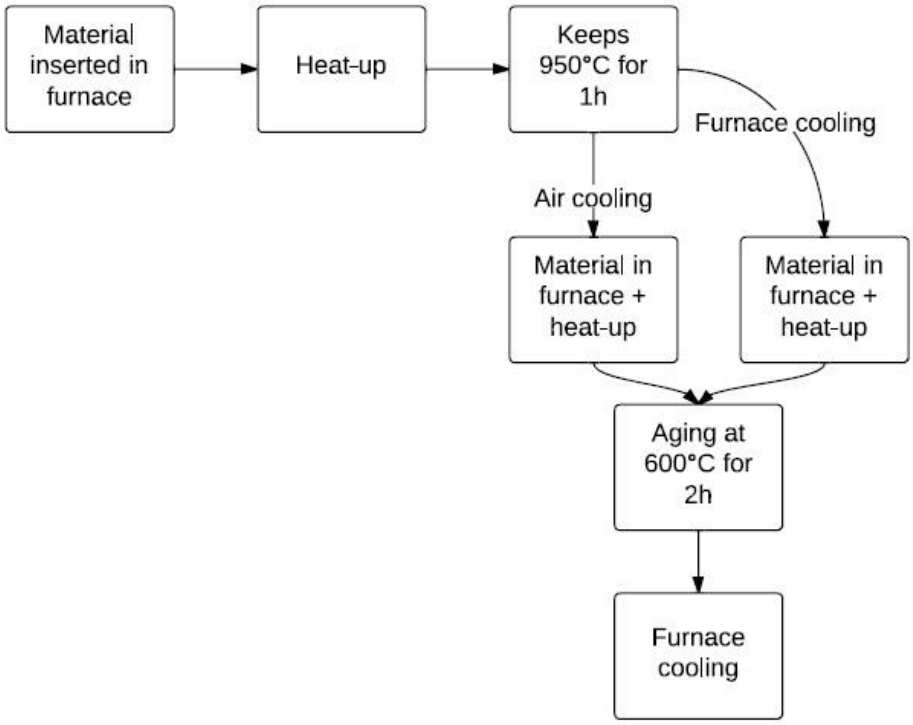

Figure 20: Flow chart for the heat treatment procedure in general, i.e. solution annealing and aging

Due to contamination of the 1st heat treatment, a new heat treatment similar to the previous had to be performed. However, as two different furnaces are used there will be some differences in heating/cooling rate and in the furnaces ability to maintain a stable and precise temperature.

3.2.1 1st. heat treatment procedure

The material were put in the oven after spark cutting, which seemed to cause some warping on a few of the samples. Making the sample preparation harder, as the specimens seemed to fall of rather easily.

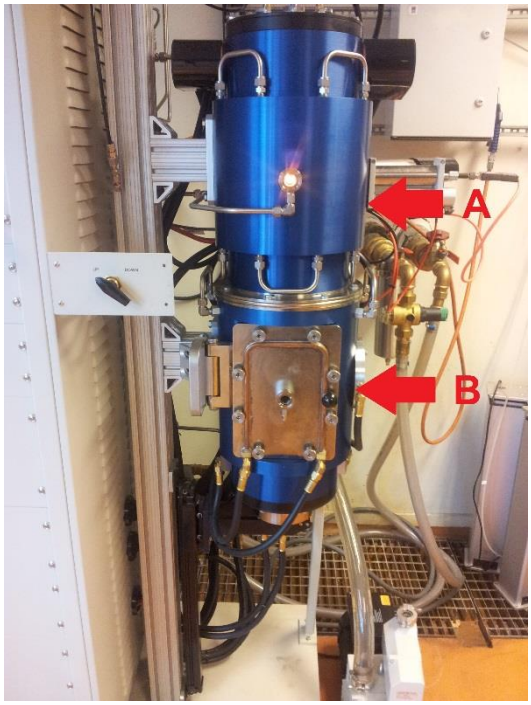

Figure 21: Showing the ReSiNa furnace used for heat treatment of the tensile samples. A: The chamber containing the samples during the heat treatment. B: Chamber were samples for AC are moved to during cooling

The oven used were a ReSiNa oven with a Graphite tube chamber (Figure 21). The atmosphere used were inert (argon), to prevent the titanium to react with the atmosphere and degrade the microstructure. The samples themselves were mounted in an alumina cups.

It was not possible to perform actual AC using the ReSiNa furnace. This is related to the graphite inside the chamber which will start to burn in air unless the temperature is below approximately 200°. The alumina cup were mounted on a flat piston surface being able to move from chamber A to chamber B. To achieve thermal gradient equal to AC the piston is moved from chamber A to chamber B, which holds room temperature. The oven in chamber A is turned off, and argon is flushed into chamber B (Figure 21) to improve cooling. The temperature in chamber B were measured with a regular mantle K-element with Fluke thermoreader right above the alumina cup.

When applying furnace cooling, the sample were kept in chamber A for the duration of the cooling period.

3.2.2 2nd. heat treatment procedure

The blocks of titanium delivered from NTi (before spark cutting) were sealed in a glass ampoule filled with argon gas. As the material was sealed in an ampoule with inert atmosphere (Figure 22), the ampoules could be exposed to high temperatures in a non-inert environment. The samples then was subjected to a similar heat treatment as in the 1st procedure, but this time in a Nabertherm N17/HR (Figure 22) furnace. As the furnace could be opened at high temperatures, the AC becomes more realistic. The oven cooling took approximately 1,5 hours from 950°C. After aging the material was sent to Nomek Ranheim for spark cutting.

Figure 22: Left: Nabertherm N17/HR was used as furnace for the second heat treatment. Right: The ampoules (after solution annealing and aging) used to seal off the material from the environment in the furnace

3.3 Material characterization

Different type of techniques used to characterize the materials, both the as-received and the contaminated specimens.

3.3.1 Thermal analysis

To be able to find the allotropic transformation temperature (β-transus), a Netzsch DIL 402 C (dilatometer) equipment. The elongated samples machined at *Finmekanisk Verksted* at NTNU were about 20-30mm. long, with either a quadratic cross section with a diagonal of about 8mm..

The dilatometer analysis measures the length expansion (dL/L_0), as the material expands during heating as well as well as during a change in crystal structure. The atmosphere inside the equipment were inert (argon), to avoid the titanium to react with air. The experiments were performed up to 1100°C, with a heating/cooling rate of 2°C/min. The samples were cleaned 10 min. in an aceton ultrasonic bath before being mounted in the Netzsch STA 449 C, to remove any dirt that might have deposited on the surface.

3.3.2 Light microscopy

The samples studied in the *Leica MEF4M* microscope were prepared in the same manner as the EBSD samples. The software used to store the images was ProgRes®CapturePro 2.8.8. To get proper contrast from the non-etched samples, polarized light with crossed polarizators were used. For the etched and deformed samples regular bright field was used. As the use of light microscopy was done to obtain an overview of the macrostructure, the magnification was limited to 2,5x and 10x.

3.3.3 Microhardness

The samples where contamination were suspected was tested for microhardness, using a Struers Duramin-A2500. In total 20 measurements were taken, at both the edge and in the bulk of a contaminated in-situ tensile specimen.

3.3.4 Chemical analysis

Due to the suspicion of contamination from hydrogen after the 1st heat treatment, the need for a chemical analysis became imminent to get an actual confirmation that hydrogen was the cause of the premature fracture. Three different samples with an approximate weight of 0,5 gram were sent to Molab AS in Porsgrunn, for chemical analysis. One sample being a reference, which should be free of contamination, and two samples with suspected hydrogen contamination. The technique used is based on combustion by induction elements in an inert atmosphere, where the amount of contamination is measured by either infrared radiation or conductivity, depending on standard for the specific material.

3.4 EBSD

The reader is referred to Chen et. al. [48] for an introduction in EBSD parameters and how they correlate. Be aware that the parameters mentioned in this section might be different depending on which microscope that is applied.

3.4.1 In-situ tensile stage

In order to perform the tensile testing in the SEM, a new stage had to be installed (Figure 23). The in-situ tensile were clamed in the tensile stage, before evacuating the SEM chamber. As the tensile stage has quite a lot free surfaces for oxygen to deposit, the SEM have to evacuate for about 6 hours until the pressure in the chamber is approximately $2 \cdot 10^{-6}$ torr. The tensile testing was done stepwise (in strain increments), usually in steps of 1% or 0,5%. For each strain increment the tensile test were paused for approximately 15 min for an EBSD scan to be performed.

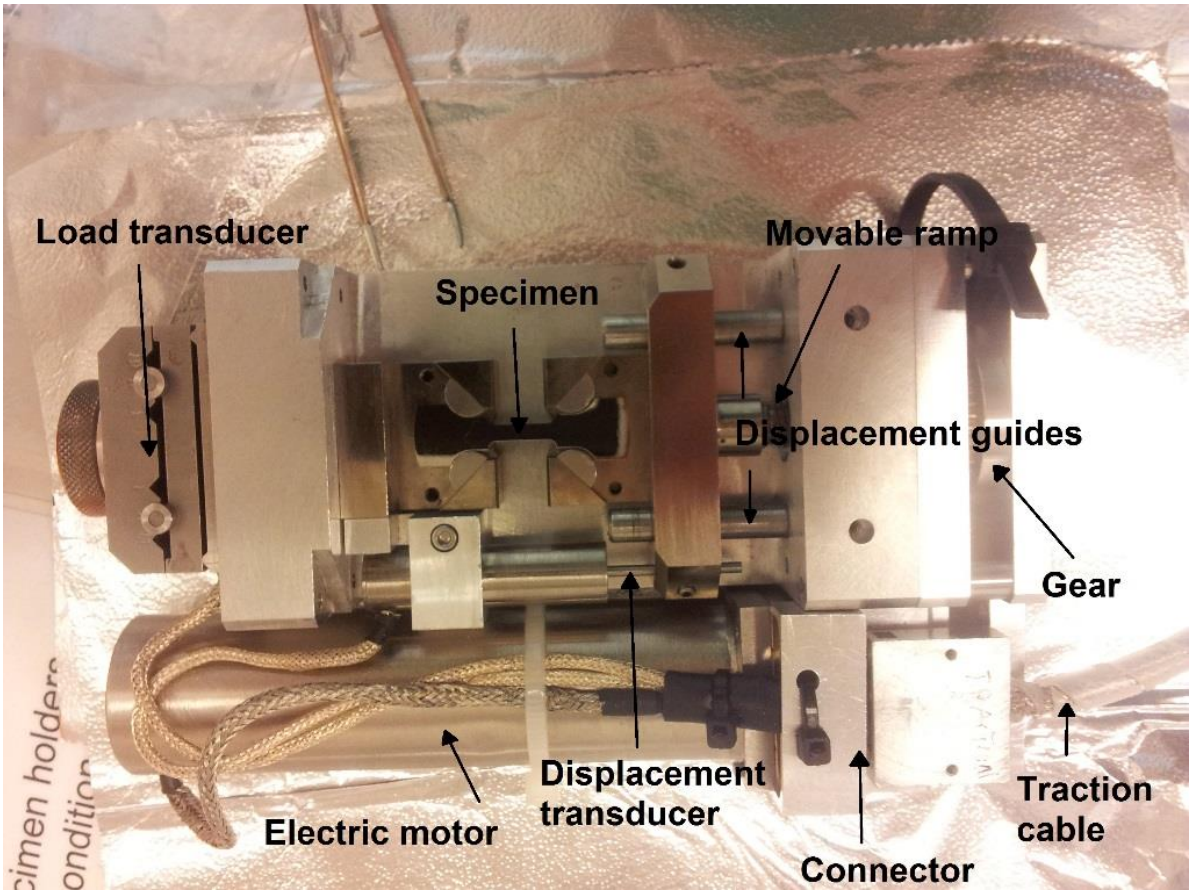

Figure 23: The tensile stage is mounted into the SEM. The specimen is clamped by using four pieces of steel shaped to fit along the tensile specimen.

It's beneficial to have some irregularities in the seconday electron (SE) image used for EBSD to use as guidance, so that the same region of interest (ROI) can be examined for every increment of strain. The elongation shown by the software (RT Traction) is somewhatlower than the actual elongation. The tensile test were usually aborted when reaching 7% strain, as some samples might go to premature fracture. It's not ideal for the samples to go all the way to fracture in the SEM, as both the sample itself and the pieces used for clamping (Figure 23) might hit and break equipment inside the chamber. Both set-up of stage, sample and software was done according to Pedersen [49]

3.4.2 SEM parameters

After inserting the sample into *Zeiss Ultra, 55 Limited Edition* and achieving vacuum, the stage can be tilted to 70°. The software used for obtaining the diffraction patterns are Nordif 2.0, the software used for indexing are OIMDC 5.32, and the detector was Nordif UF-1000. When switching from the secondary electron image to Nordif 2.0 the contrast should be as high as possible so that the user is able to observe distinct areas in the image. It should be noted that these parameters depends on the deposition of hydrocarbons on the surface.

The aperture (wobble-function) and astigmatism should be adjusted after the EBSD detector is inserted, alongside with the final focus. This is because the EBSD-detector will affect the electron column and backscattered electrons. The aperture and focal plane should be optimized at a magnification up towards 10000X. The dynamic focus should be adjusted to get as much of the tilted sample in focus. This is most crucial for the area towards the center, since this is the region that will make the ROI. As the sample is tilted the tilt compensation mode could be activated to obtain a correct image, although it's not necessary as the function is integrated into Nordif 2.0.

E0 [kV]	Aperture [µm]	WD [mm]	Tilt angle [°]	Magnification
20	300	23.3-24.5	70	800

Table 5: The SEM parameters used during EBSD in the in-situ tensile tests.

Before scanning the ROI in Nordif 2.0, the tilt compensation should be switched off, as this is an already integrated function in the Nordif software. When optimizing the diffraction pattern, the frame rate and gain should be adjusted so that the amount of electrons per diffraction pattern is just too low for the diffraction patterns to be oversaturated by light.

Scanned area [µm x µm]	Step size [µm]	Image resolution	Frame rate [fps]
Height: 175-130 Width: 175-140	0.35-0.25	600x600	0.2

Table 6: EBSD parameters from Nordif 2.0 used during the in-situ tensile tests

When operating in Nordif 2.0, the parameters in the table 5 should be adjusted before continuing any further. To improve the quality of the diffraction patterns, background subtraction should be applied. After marking ROI, the user have to specify points for calibration. The calibration points will be used when indexing the diffraction patterns later on. In general 5 calibration points should be obtained. However, by using additional calibration points the user can choose to discard some of them during indexing. If the CI-value is too low (0.4), or the fit-value too high they should be discarded (1,0°).

	Frame rate [fps]	Gain	Resolution [px]
Calibration settings	75-140	4	160x160, 240x240
Acquisition settings	195-390	2-6	120x120

Table 7: EBSD parameters from Nordif 2.0 for calibration and acquisition data points

3.5 Mechanical Testing

Samples for EBSD in-situ tensile testing were extracted from the same material as the samples in tested by a conventional tensile test, performed at SINTEF Raufoss Manufacturing (SRM). The material were tested in the deposition direction and the build direction. For a full overview of the mechanical data, see Appendix B.

4. Results

The following section will show a selection of the results obtained in this project. Although the main task was to study the deformation behavior of the Ti-6Al-4V, both with and without heat treatment, the occurrence of hydrogen and oxygen contamination during the 1st heat treatment (section 3.2.1) gave rise to some new investigations. In addition, the thermal analysis performed by dilatometry will be presented.

4.1 In-situ tensile tests

In total 10 in situ tensile tests were performed, 3 on the as-received material, 3 on the heat treated material with air cooling (AC) and 4 on the heat treated material with furnace cooling (FC). Several aspects during of the micro deformation were studied, in addition to investigating the macro deformation of the specimens after testing. All images from the in-situ tensile tests were processed in OIM Analysis 6.1.

4.1.1 Texture

Although texture analysis isn't the main scope of this report, there are some interesting aspects that needs adressing for further research in the future. 3 contoured pole figure for the (0001) direction, 1 from each material state is presented. It should be noted that there's a significant scatter in different inverse pole figures and intensities both between the different material, as well as between material with the same thermal history.

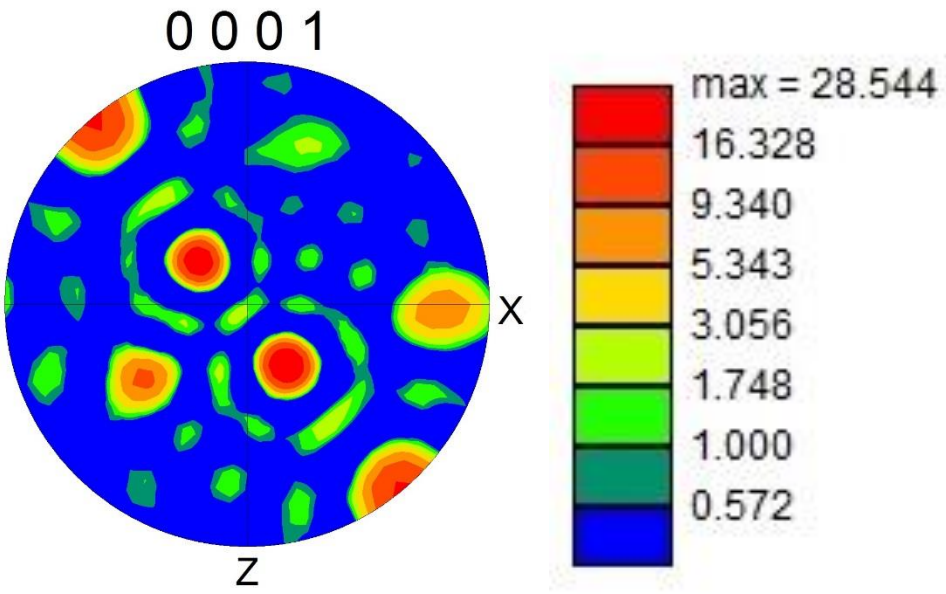

Figure 24: <u>Left:</u> Contoured pole figure in the x/z-plane for the as-received material in the (0001) direction. The texture is extracted from an area with dimension 140µm x 130µm (Figure 66 in Appendix G). <u>Right:</u> Showing the intensity levels of the contoured pole figure

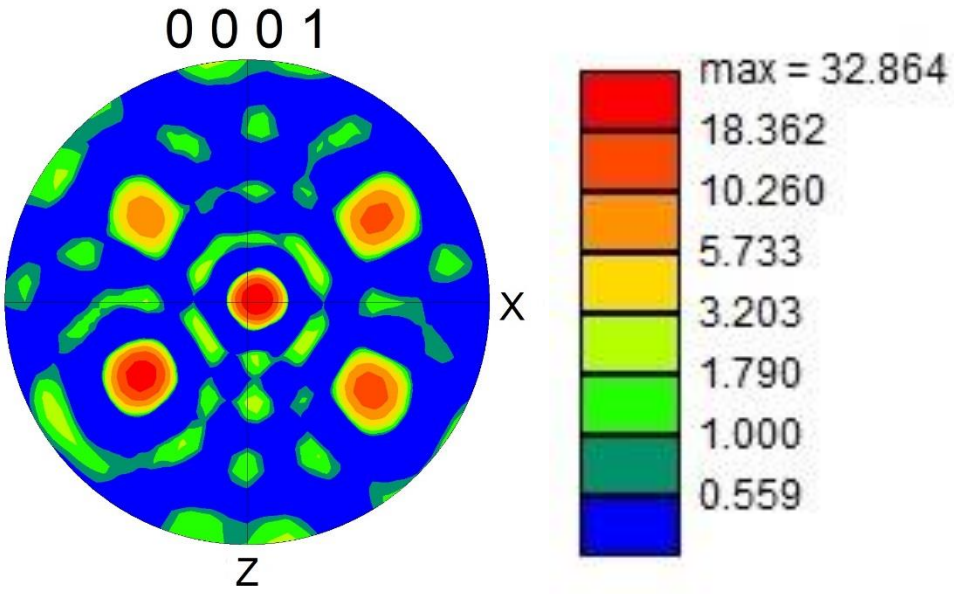

Figure 25: <u>Left:</u> Contoured pole figure in the x/z-plane for the AC material in the (0001) direction. The texture is extracted from an area with dimension 175µm x 175µm (Figure 69 in Appendix G). <u>Right:</u> Showing the intensity levels of the contoured pole figure

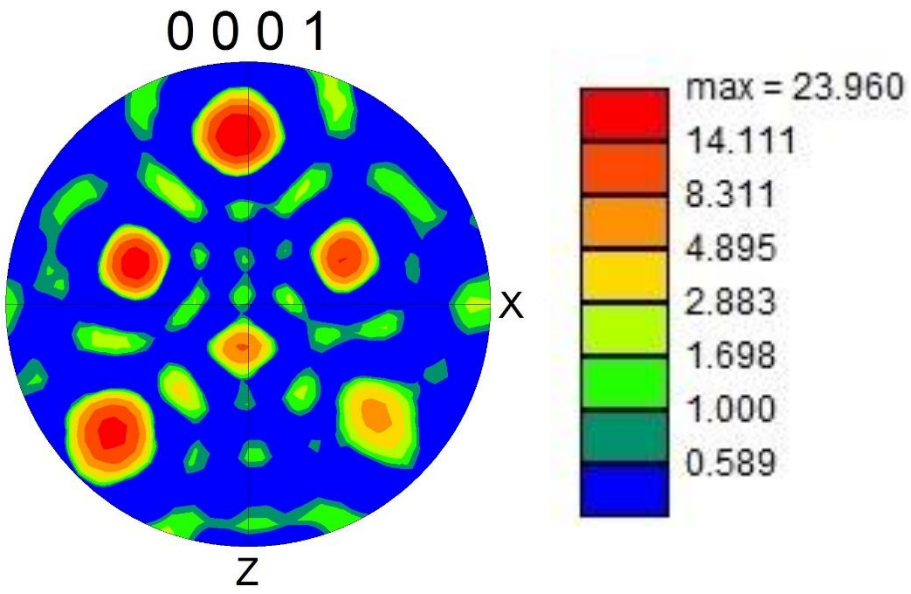

Figure 26: Left: Contoured pole figure in the x/z-plane for the FC material in the (0001) direction. The texture is extracted from an area with dimension 175µm x 175µm (Figure 36). Right: Showing the intensity levels of the contoured pole figure

4.1.2 Microdeformation

The use of in-situ tensile testing using EBSD gives an unique insight into the deformation of the material at a microlevel. However, as the ROI only constitute for a fraction of the total tensile area (area 1, 2 and 3 in Figure 41), one should not exclude the presence of other deformation mechanisms that's not observed. Nonetheless, the observations are important to further increase the understanding of the Ti-6Al-4V produced by AM. The results presented here, are only a fraction of what can be extracted from the material when using OIM Analysis 6.1. The main focus in the analysis performed is on the Schmid factor for basal and prismatic slip and the stiffness (E-module). All the IPF figures shown in this report uses the normal direction as a reference direction, i.e. out of the plane.

4.1.2.1 As-received material

Figure 27 shows a triple-point intersection of three β-grain boundaries. It is seen that the slip has a tendency to go along the lamellae boundaries before accumulating at the grain boundaries. The interior of the grain to the right in Figure 27 is more or less free for deformation.

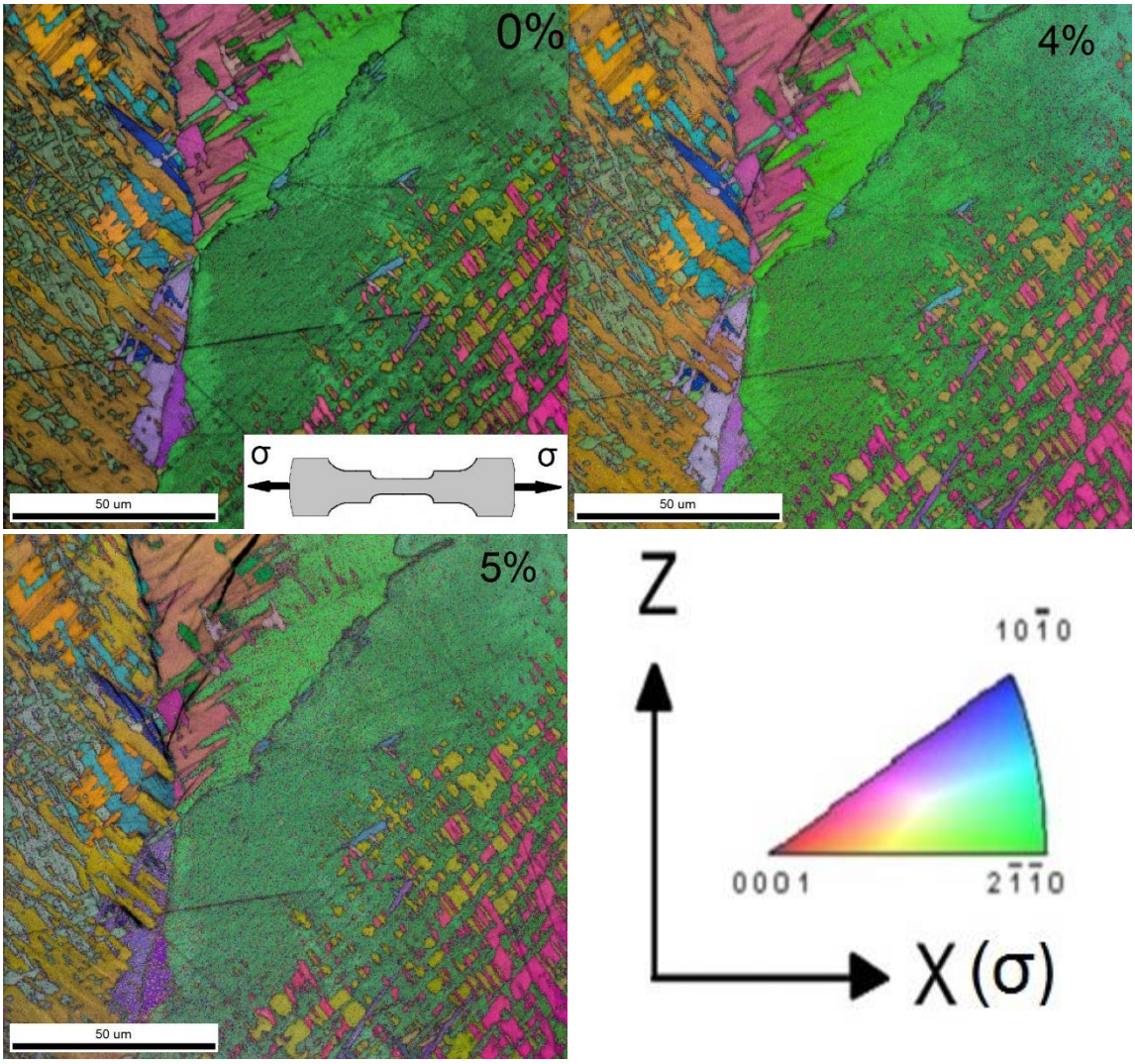

Figure 27: Image Quality (IQ) map colored according to the inverse pole figure (IPF) showing the strain response at 0%, 4% and 5% elongation for the as-recieved material at a tripple-point (intersection of three grain boundaries). CI-value at 0% strain were 0.36, and the Fit were 1.23. The belonging inverse pole figure and the axis orientation are shown at the bottom right corner

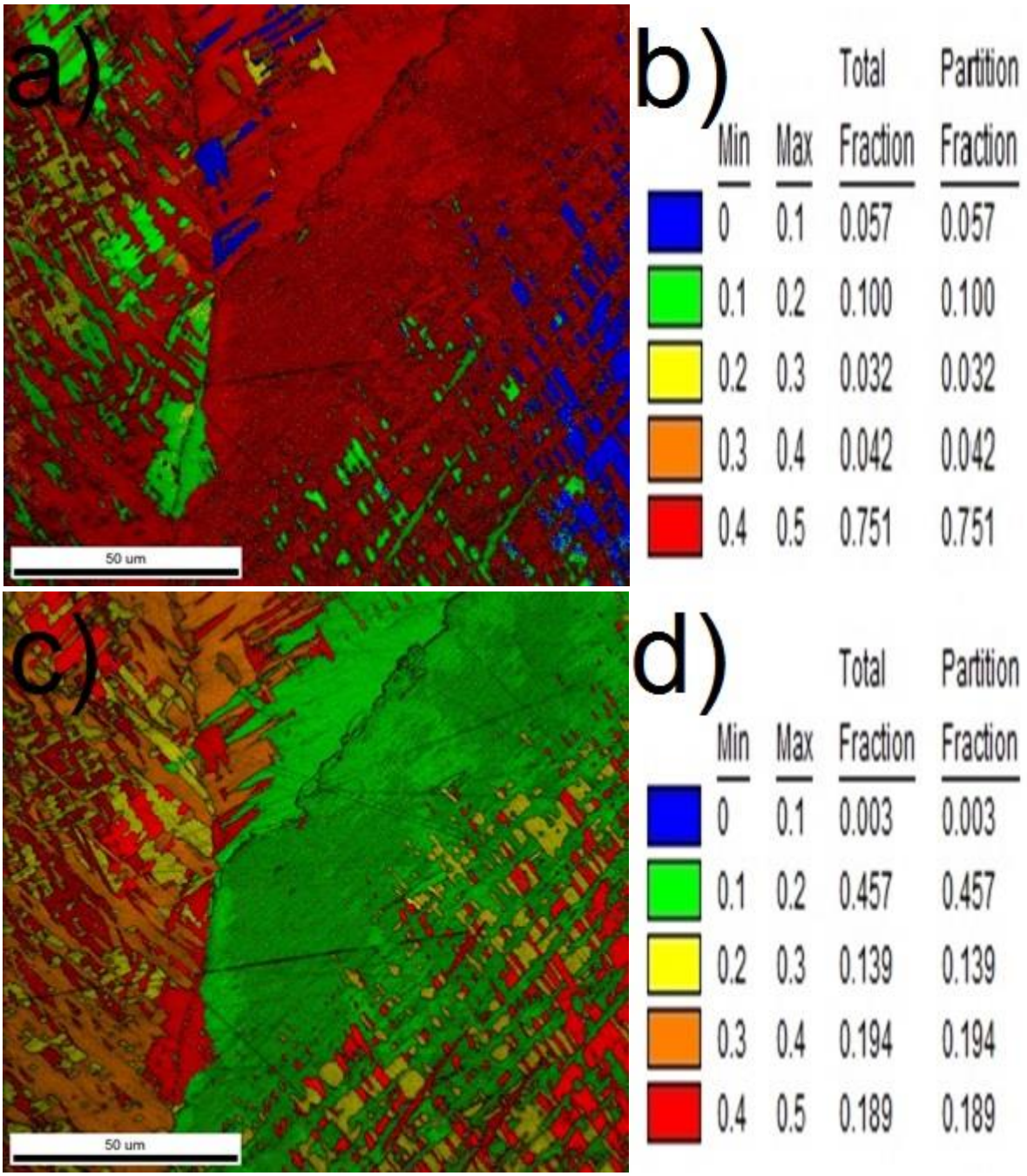

Figure 28: a) Shows the Schmid factor for basal slip (0001)$< \bar{1}\bar{1}20 >$ at 0% strain for the as-received material, while b) shows the values and fractions of the different segments of the basal Schmid factor. c) Shows the Schmid factor for prismatic slip $(\bar{1}100)\langle\bar{1}\bar{1}20\rangle$, while d) shows the values and fractions of the different segments of the prismatic Schmid factor

As can be seen in Figure 28 theres's a significant fraction of high Schmid factor for basal slip in all the three grains observed, with smaller scattered regions (islands) having a very low Schmid factor, i.e. hard to deform. Prismatic slip is mainly limited to the left grain. The stiffness (E-

module) is also related to the orientation of the grains (section 2.5.3), in a somewhat similar way as the Schmid factor (section 2.5.2). A high stiffness makes the grain harder to deform, and visa versa. The left grain is dominated by a low stiffness, while the right and middle grain have higher average E-module.

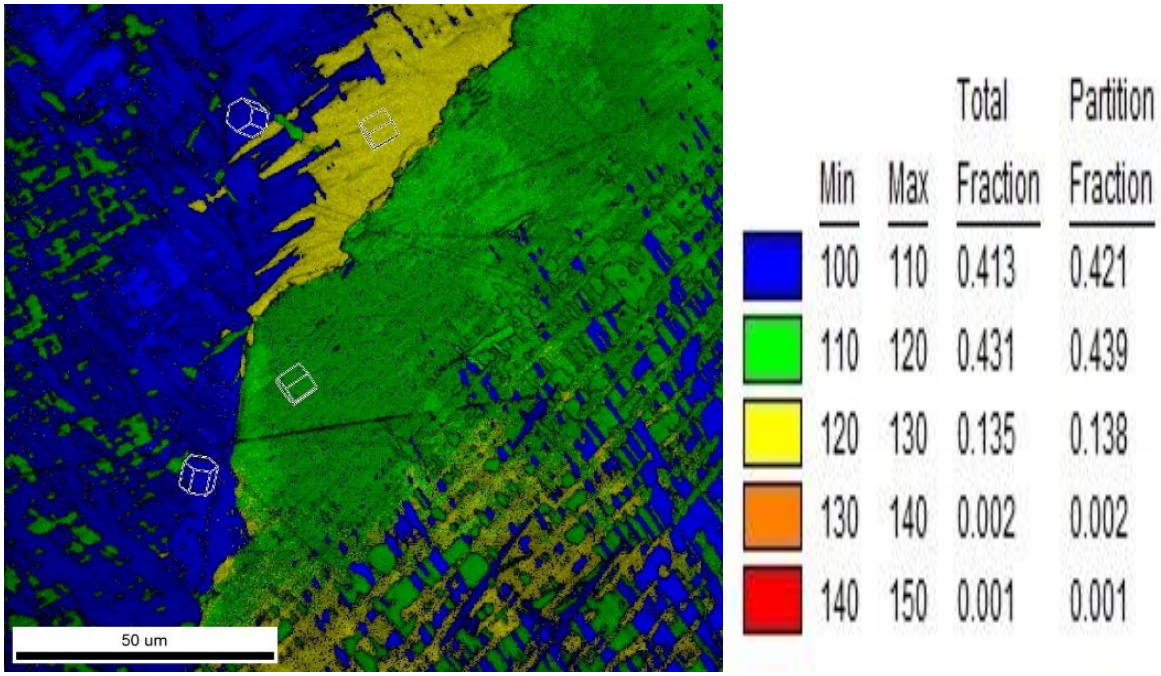

Figure 29: <u>Left:</u> Showing the E-module [GPa] of the α-phase in the as-recieved material at 0% strain. Four lattices are drawn in the figure, showing how the E-module in Ti-6Al-4V is dependent on its orientation. <u>Right:</u> Showing the values [GPa] and fractions of the different segments of the elasticity

One of the slip lines observed in Figure 27 are studied further, with respect to both the Schmid factor of prismatic slip, and the strain accumulation at the boundary. The image showing 5% elongation in Figure 27 are cropped, i.e. a small area in the image is studied more extensively. The slip seems to travel along lamellae boundary before cutting a small alpha lamellae (or segment) in two, before eventually ending up at the grain boundary.

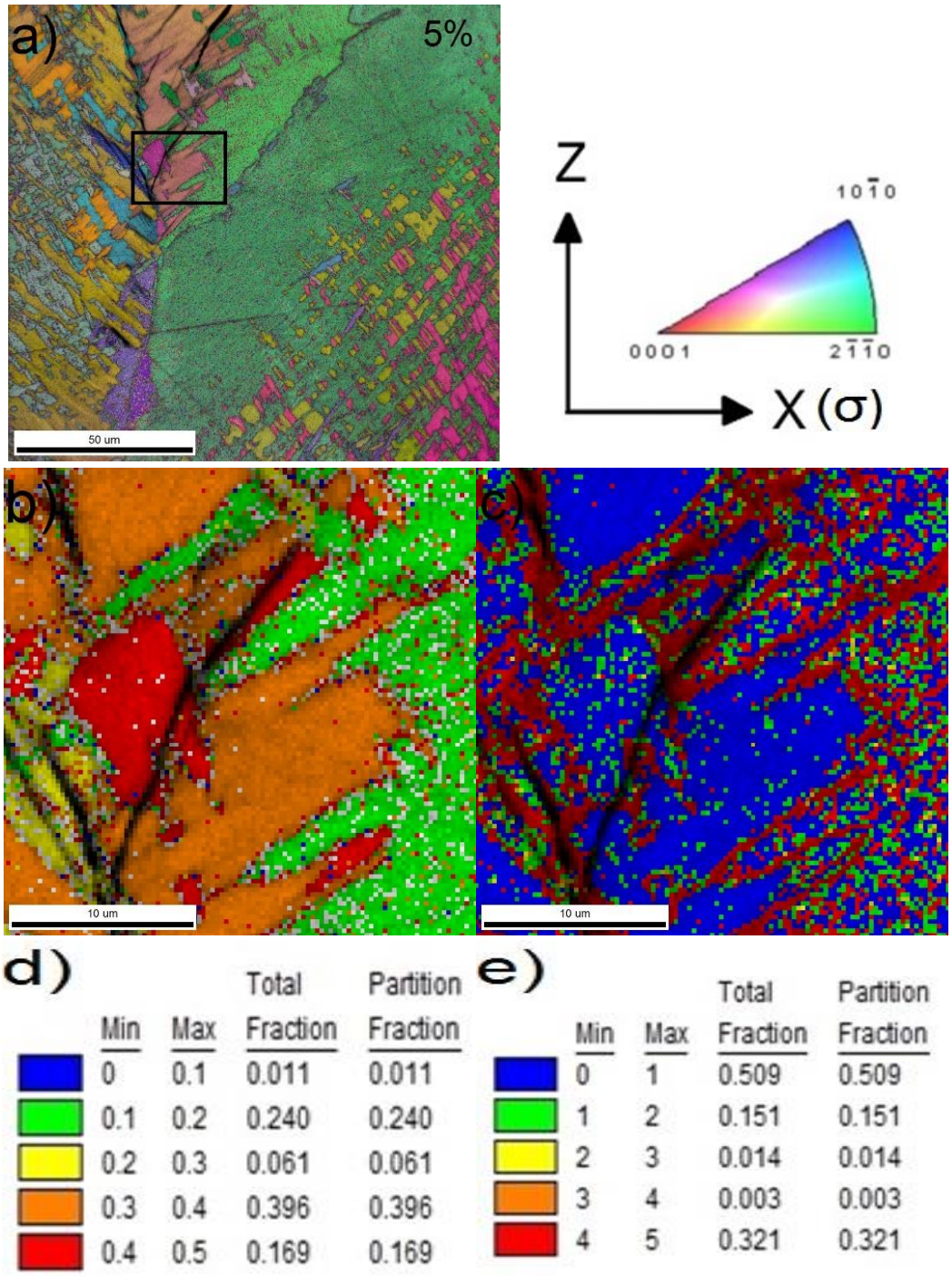

Figure 30: a) IQ/IPF image at 5% strain, the black square indicates the cropped area. b) showing the prismatic $(\bar{1}100)\langle\bar{1}\bar{1}20\rangle$ Schmid factor of the cropped image. c) showing up to 5° of the local misorientation of the cropped image. d) and e) Shows the partitioning and fractions of the Schmid factor and the local misorientation respectively

To investigate whether or not the slip line in Figure 30 were promoted to grow further due to a similar orientation of the lamellae (or segment) the slip is travelling though, the misorientation of the three grains in question is measured at 0% strain.

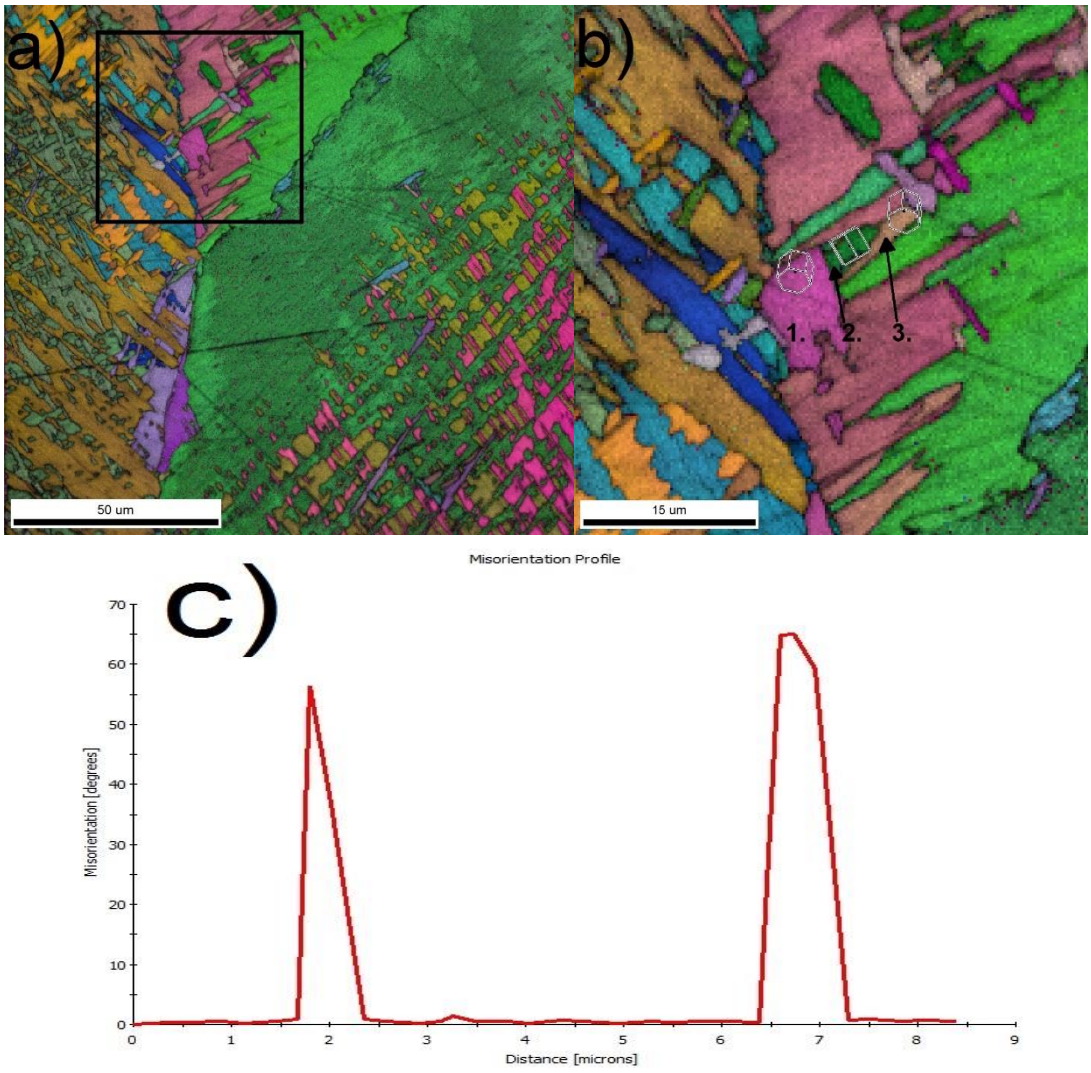

Figure 31: a) An IQ-IPF map at 0% strain showing the region being cropped b) The lattice of three grains, the misorientation was measured from grain 1. To grain 3., via grain 2. c) The misorientation plot shows two peaks at approximately 56° and 64°

4.1.2.2 Furnace-cooled material

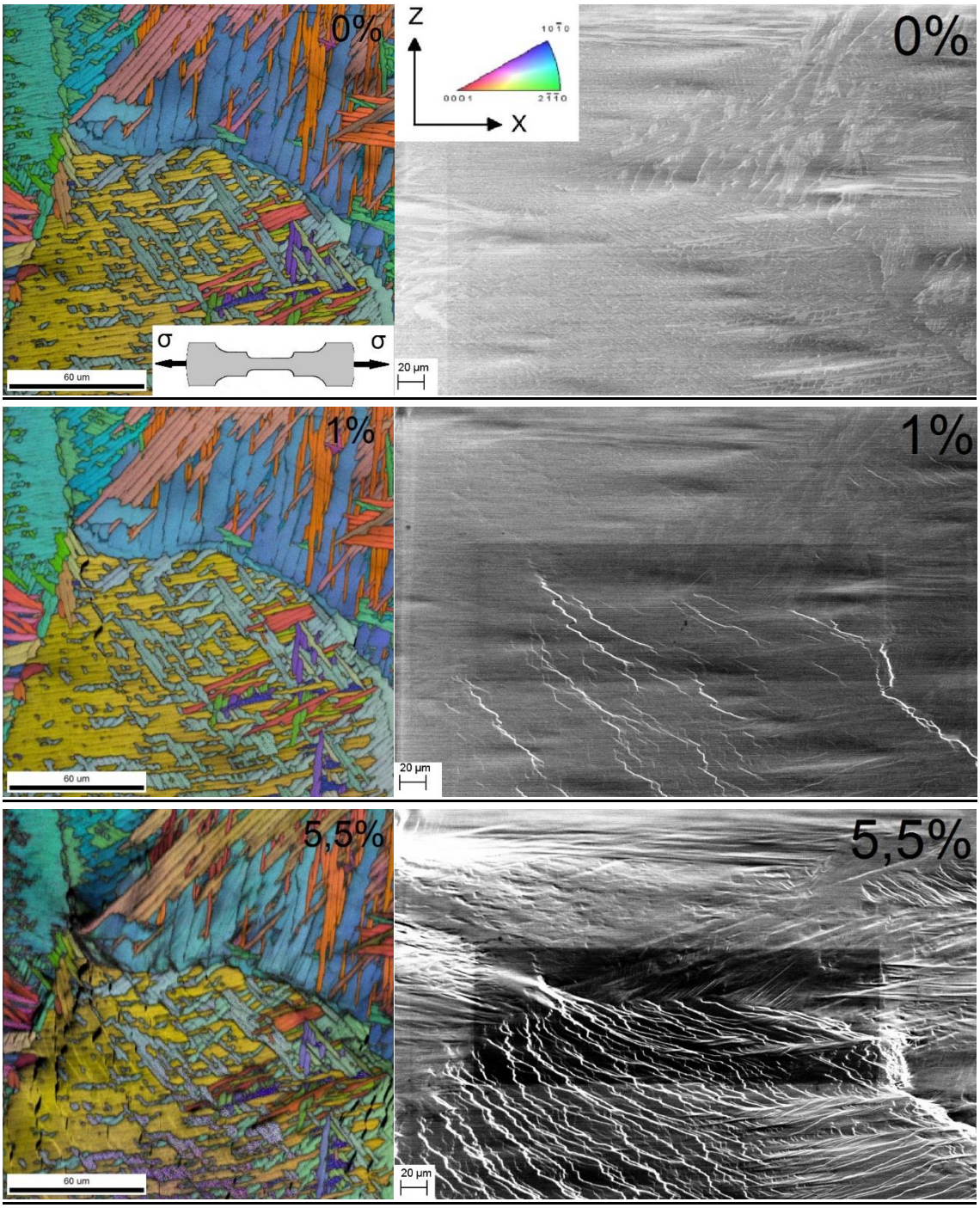

Figure 32: <u>Left:</u> IQ/IPF-map of a triple-point (intersection of three β-grain boundaries) in the FC material. Showing the strain response at 0%, 1% and 5.5%. CI-value at 0% strain were 0.52, and the Fit were 0.89. <u>Right:</u> SE images of the ROI after 0%, 1% and 5.5% strain at 800x. The black rectangular seen in the image for 1% and 5.5% are caused by hydrocarbons and shows the ROI.

The FC material should (in theory) have the most homogenous material when it comes to deformation. It is however observed in Figure 32 that the slip is restricted to one of the three β-grains. The SE images shows the result of deformation in form of topography. The bottom grain is clearly deformed more than the surroundings, as can be seen at 5,5% strain in Figure 32.

The E-module for in the ROI of Figure 33 is highly unhomogenous, as one of the grains has an orientation that makes more or less the entire grain obtaining a low stiffness. There are however a lamellas in the two other grains exhibiting a similar stiffness, but on average the E-module in the two other grains are higher.

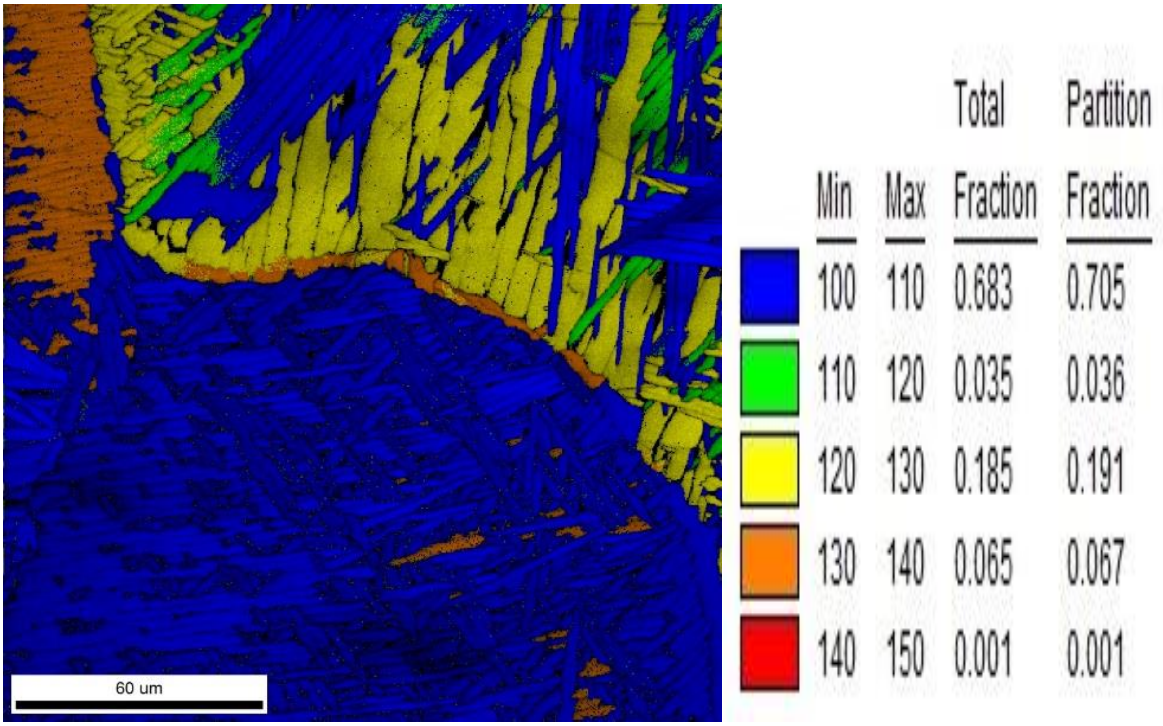

Figure 33: <u>Left:</u> Showing the E-module [GPa] of the α-phase in the FC material at 0% strain. There are a clear distinction between the stiffness in the three grains. <u>Right:</u> Showing the values [GPa] and fractions of the different segments of the elasticity

The lamellas close to the grain boundary in the two grains at the top of Figure 33 has a low Schmid factor for prismatic slip, while the lamellas in the interior of the two grains seems to have a more evenly distributed Schmid factor. The bottom colonies shows high to intermediate Schmid factor for prismatic slip. The Schmid factor for basal slip is generally high for the entire ROI, except for the top grain to the left.

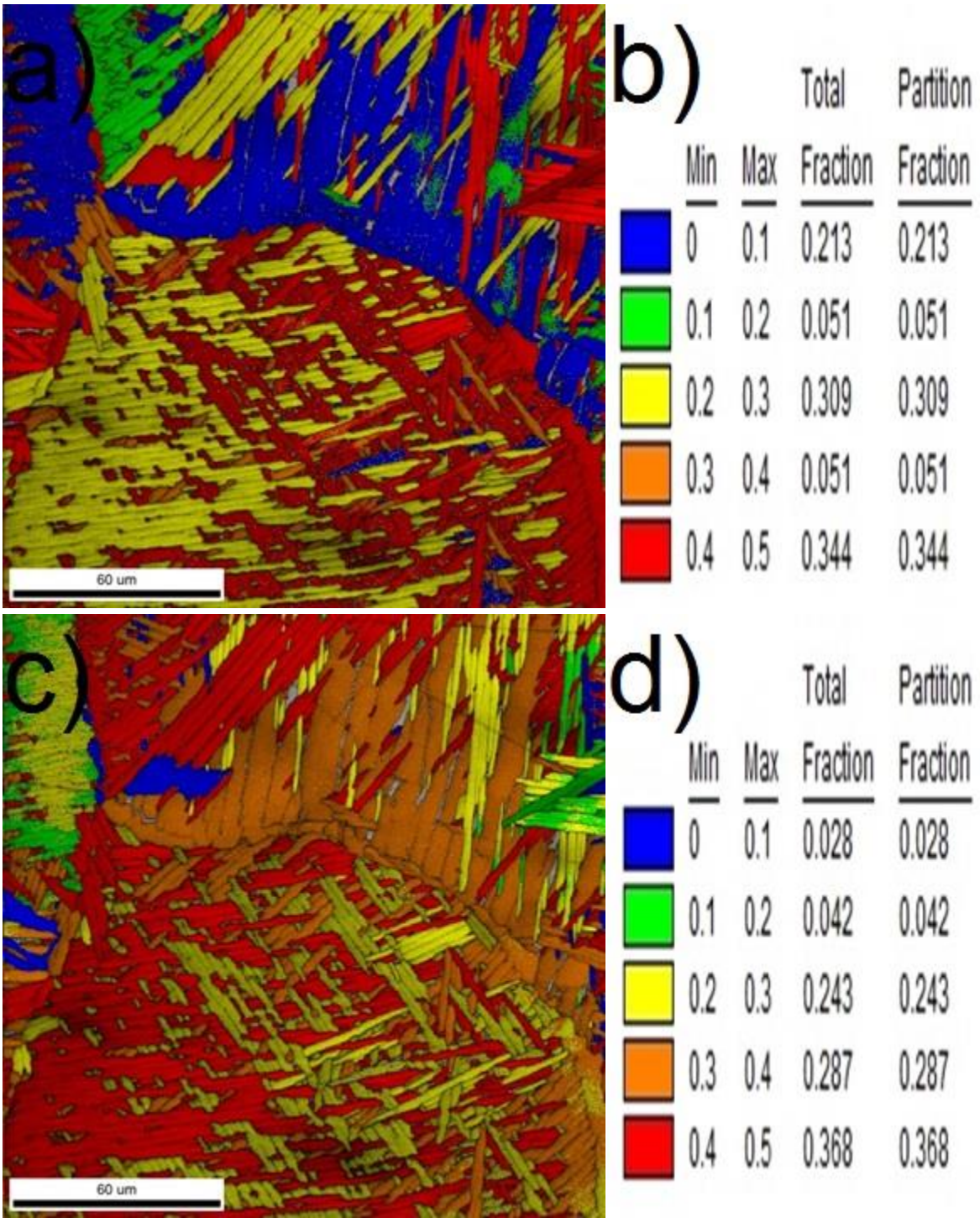

Figure 34: a) Shows the Schmid factor for prismatic slip $(\bar{1}100)\langle\bar{1}\bar{1}20\rangle$ at 0% strain for the FC material, while b) shows the different segments for the prismatic Schmid factor and their fractions. c) Shows the Schmid factor for basal slip (0001)$< \bar{1}\bar{1}20 >$ at 0% strain for the FC material, and d) shows the different segments for the basal Schmid factor and their fractions

The Schmid factor for basal slip (Figure 34) is significantly higher than the prismatic in all the three colonies observed. Only a small fraction (approximately 3%) of the material is showing a basal Schmid factor towards 0. As the bottom colony has quite different mechanical properties than its surroundings, which is displayed during deformation, the grain boundary towards the top grain is being examined further. It's shown in Figure 35 that there's a relatively large misorientation between the two grains, which would result in accumulation of dislocation when stress is applied, and eventually leading to slip along the boundary.

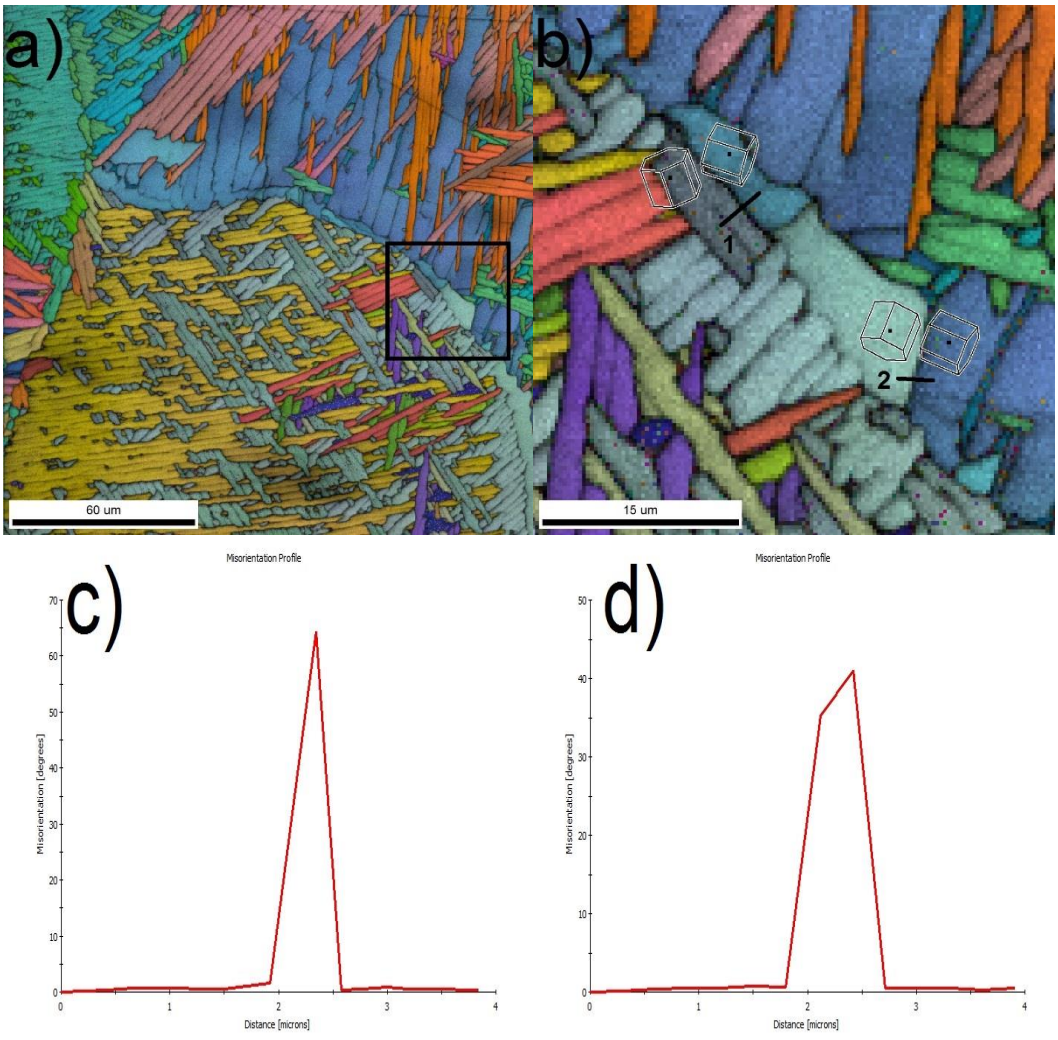

Figure 35: a) An IQ-IPF map at 0% strain where the black square shows the region that's being cropped. b) The lattice of two pairs of neighbouring lamellas at the grain boundary. The two line segments shows where the measurement of misorientation has taken place. c) The misorientation of line segment 1 shows a grain boundary angle at 64°. d) The misorientation of line segment 2 shows a grain boundary angle at 41°.

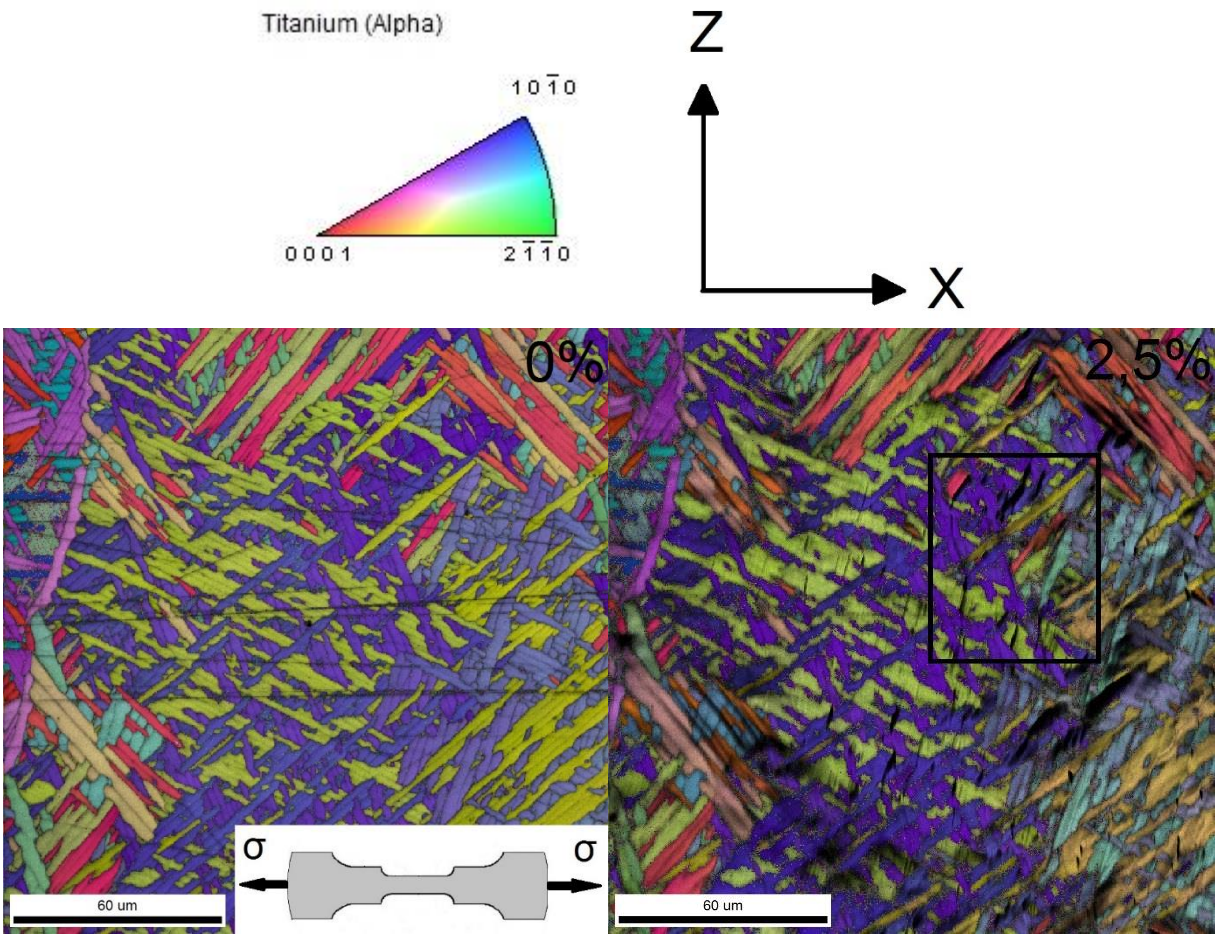

Figure 36: IQ/IPF map of FC material. The α-colony at 0% and 2.5% strain, showing several slip lines in the z-direction. The black square in the right image shows the region that have been cropped for Figure 37. The CI-index and fit-value at 0% strain is 0.45 and 1.09 respectively

A second in-situ tensile test for the FC material is shown in Figure 36, showing the effect of the lamellae width. The slip in the α-colony travels perpendicular on the lamellas seen in Figure 36, i.e. in the width direction, as well as being aligned close to perpendicular to the stress axis (x-axis). The lamellas within the colony are overlapping creating what resembles a discontinous basketweave structure.

After cropping of Figure 36, the Schmid factor of both basal and prismatic slip are calculated in Figure 37. The four slip lines marked in Figure 37 are basal in nature. The 1st, 2nd and 3rd are limited to the lamellae width, as they soon encounter a lamellae with a low basal Schmid factor. The fourth slip line has the same origin as the three others, but seems to travel a short distance into the new unfavorable α-orientation before coming to a complete stop.

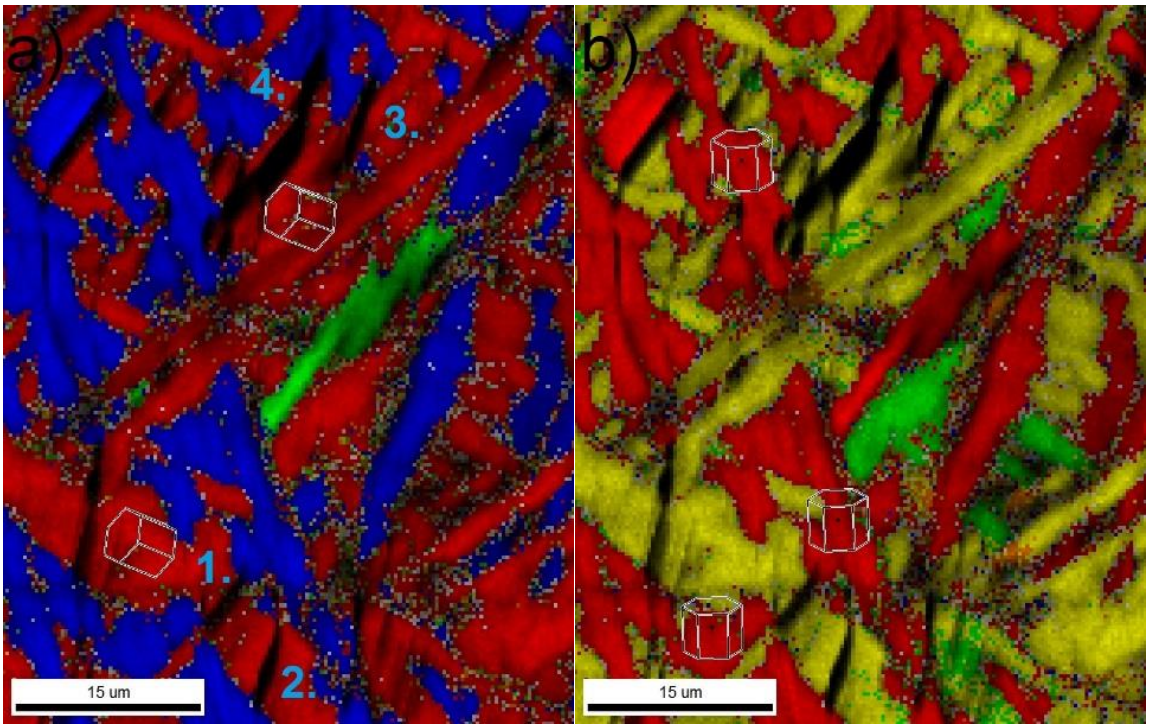

c)

	Min	Max	Total Fraction	Partition Fraction
	0	0.1	0.349	0.349
	0.1	0.2	0.038	0.038
	0.2	0.3	0.015	0.015
	0.3	0.4	0.033	0.033
	0.4	0.5	0.492	0.492

d)

	Min	Max	Total Fraction	Partition Fraction
	0	0.1	0.012	0.012
	0.1	0.2	0.074	0.074
	0.2	0.3	0.387	0.387
	0.3	0.4	0.051	0.051
	0.4	0.5	0.404	0.404

Figure 37: Showing the cropped area from Figure 36. Some HCP-lattices are drawn to show the orientation of the different regions in the image. a) The Schmid factor for basal slip (0001)$< \bar{1}\bar{1}20 >$. b) The Schmid factor for prismatic slip$(\bar{1}100)\langle\bar{1}\bar{1}20\rangle$. c) and d) shows the partitioning and fractions for basal slip and prismatic slip respectively

4.1.2.3 Air-cooled material

The material that underwent air-cooling after solution annealing, should be more homogenous than the as-received material, but this effect could have been somewhat suppressed due to the cooling rate. The amount of β-phase in all the three material states (as-received, FC and AC) are

minimal, as can be seen in Figure 38. The β-phase is mainly found along grain and lamellae boundaries.

The slip is observed mainly in the left grain towards the grain boundary in Figure 39, and seems to mainly travel along the lamella exterior or boundary. The secondary electron images shows that the slip and deformation clearly is concentrated in towards the grain boundary.

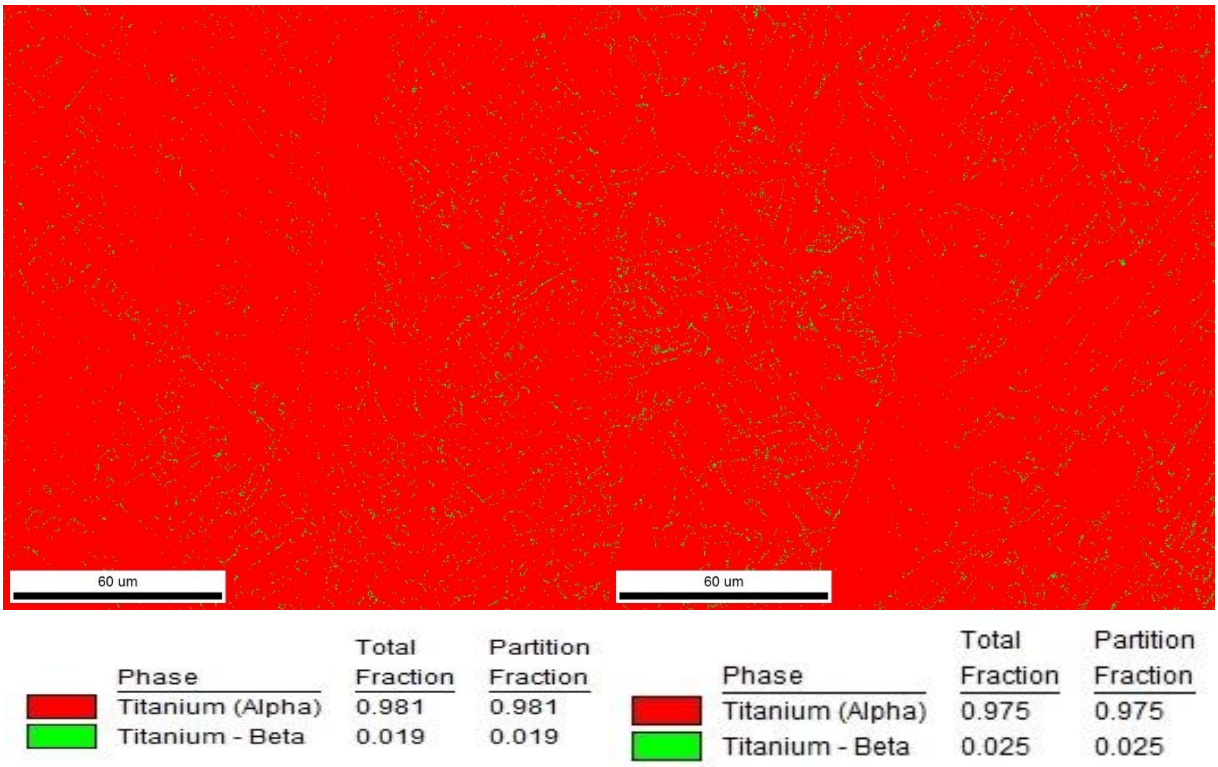

Figure 38: Showing the phase distribution in two AC specimens. The phase-distribution to the left is the same area seen in Figure 39

In the cropped image (Figure 40), both Schmid factors and the E-module are considered for a restricted area from Figure 39 with several slip lines (at 3% strain). There seems to be both pure prismatic slip, and slip occurring due to hard-soft grain interaction.

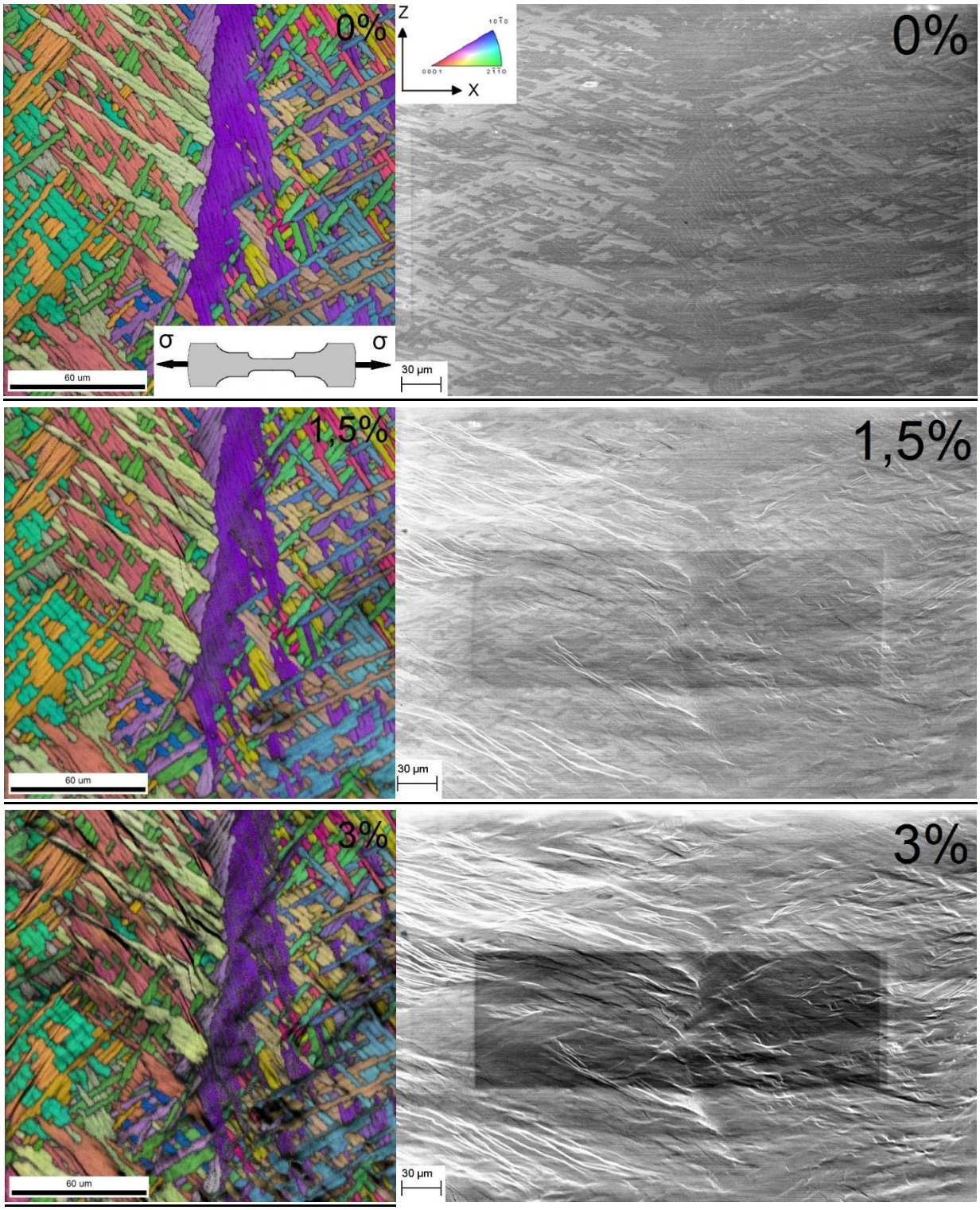

Figure 39: <u>Left:</u> IQ/IPF-map of a grain boundary in the AC material. Showing the strain response at 0%, 1.5% and 3%. CI-value at 0% strain were 0.51, and the Fit were 0.96. <u>Right:</u> SE images of the ROI after 0%, 1.5% and 3% strain at 800x. The black rectangular shown in the image for 1.5% and 3% are caused by hydrocarbons and shows the ROI

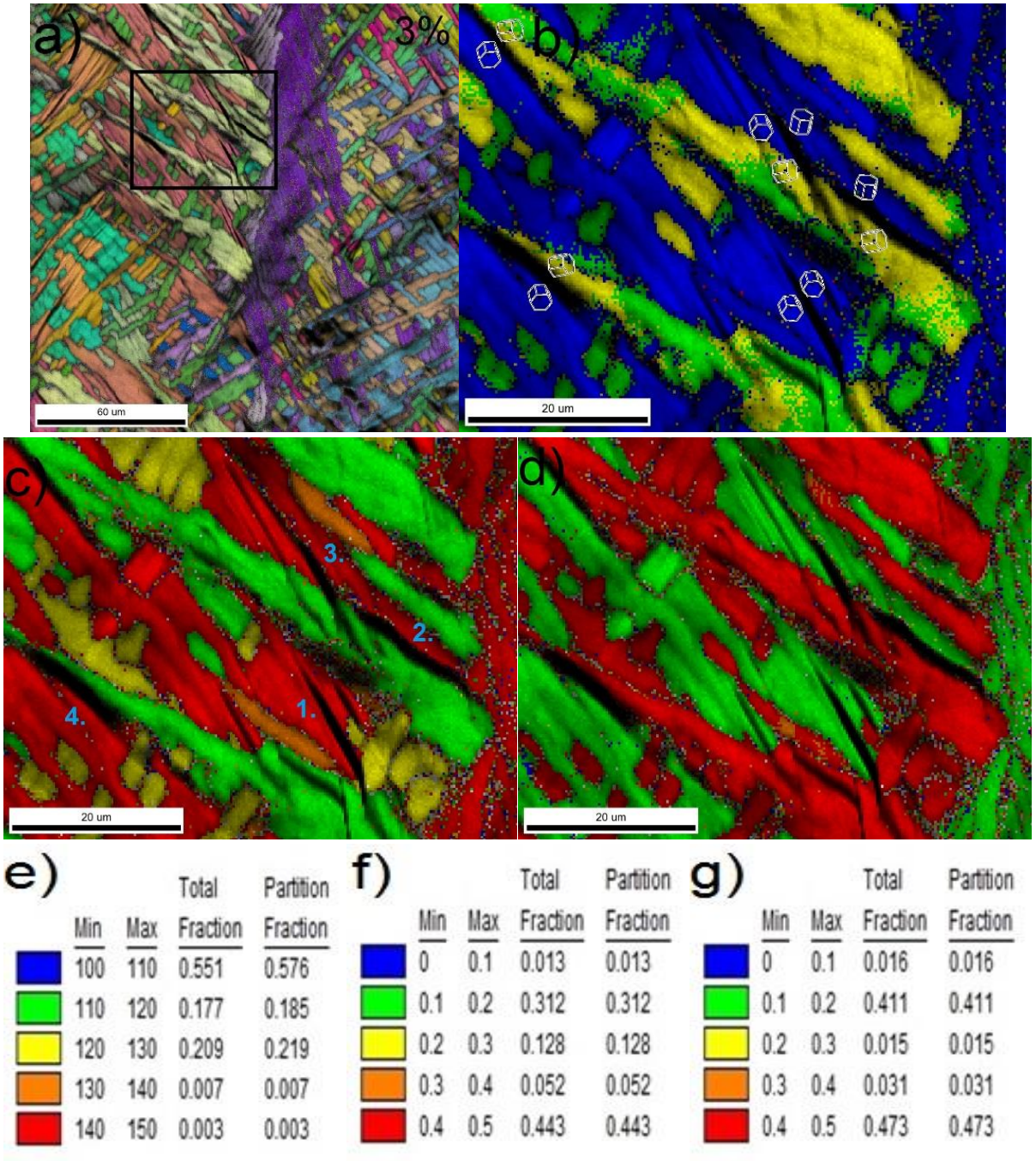

Figure 40: a) IQ/IPF image at 3% strain, the black square shows the area that has been cropped. b) Showing the E-module [GPa] as well as the crystal orientation of some of the lamellas c) showing the prismatic Schmid factor. d) showing the basal Schmid factor. e), f) g) shows the partitioning and fractions of the E-module and prismatic and basal Schmid factor respectively

4.1.3 Macrodeformation

To get an overview of the general deformation of the material, bright field microscope was used on the specimens after the tensile test to observe the distribution of deformation.

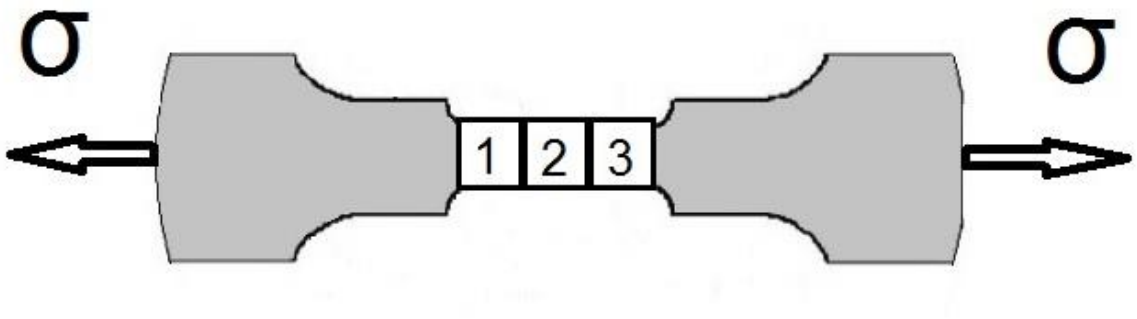

Figure 41: Showing the three sections of the tensile specimen where the images of the macrodeformation have been obtained from.

There's an obvious accumulation of deformation along the grain boundaries in the as-received material (right hand side in Figure 42). Even though there's some slip occurring in the interior of the grains, it's limited compared to the exterior at the grain boundaries. The deformation is restricted to the tensile area (area 1, 2, and 3 in Figure 41), which is expected.

The FC material to the left in Figure 42 shows a more homogenously distribution of deformation, than in the as-received material. Even though there's still some accumulation of slip along the grain boundaries, it seems as the deformation is more severe in the interior of the grains than in the previous picture. The deformation is mainly limited to area 2 in Figure 41.

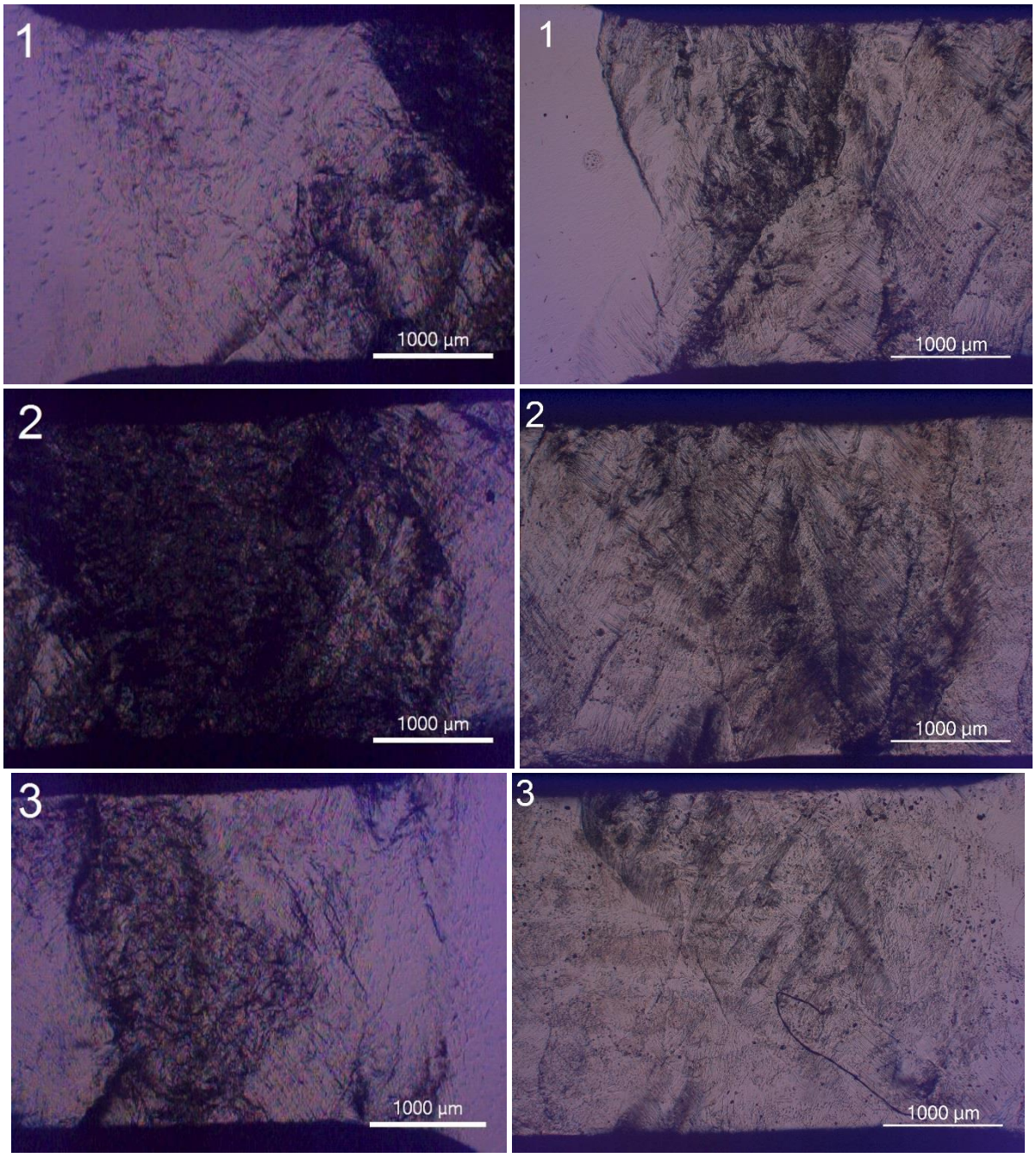

Figure 42: <u>Left</u>: Three pictures of the macrodeformation of the FC material in-situ tensile specimen obtaining 8,5% strain. Accumulation of deformation along β-grain boundaries, as well as in the interior of the grains. <u>Right</u>: Three pictures of the macro deformation in a tensile specimen (as-recieved) obtaining 8% strain. Note the accumulation of deformation along the β-grain boundaries.

4.2 Premature fracture

The first batch of specimens that underwent a heat treatment (section 3.2.1), showed a very brittle behavior. The samples fractured either during fastening or after a slight increase in stress (300MPa) during the in-situ tensile test. To understand what caused this unexpected behavior, four parallels were made (Table 8), experiencing the exact same temperature cycle as the previous specimens (section 3.2.1). The parallels were then investigated in bright field microscope and by chemical analysis and microhardness. In addition the fracture surfaces of the already fractured specimens were investigated. The as-received material (no heat treatment) is used as reference for most of the results obtained.

Sample	**1**	**2**	**3**	**4**
Treatment	Furnace cooled	Furnace cooled + aging	Air-cooled + aging	Air-cooled

Table 8: Four different parallels were made. Each of them experienced a different heat-treatment

4.2.1 Chemical analysis

The chemical analysis performed by Molab AS, gave good indications of hydrogen contamination as can be seen in Table 9.

SAMPLE	**Contaminated (1)**	**Contaminated (2)**	**As-received (Not-contaminated) (3)**
Amount [ppm]	102	82	43

Table 9: The values of hydrogen in the three samples sent to Molab, given in [ppm]

4.2.2 Bright field microscope

To investigate the effect of hydrogen contamination on the microstructure, the parallels (Table 8) were investigated in bright field microscope with polarized light. The samples was later etched, and investigated in a regular bright field mode. A conventional microstructure for the AM produced Ti-6Al-4V is shown in Figure 43. The β-grains in Figure 43 are columnar, containing a fine lamellar structure. Due to the nature of the AM-process the microstructure is not

homogenous. The axis from the bright field microscope images are the same as for microdeformation (Figure 39).

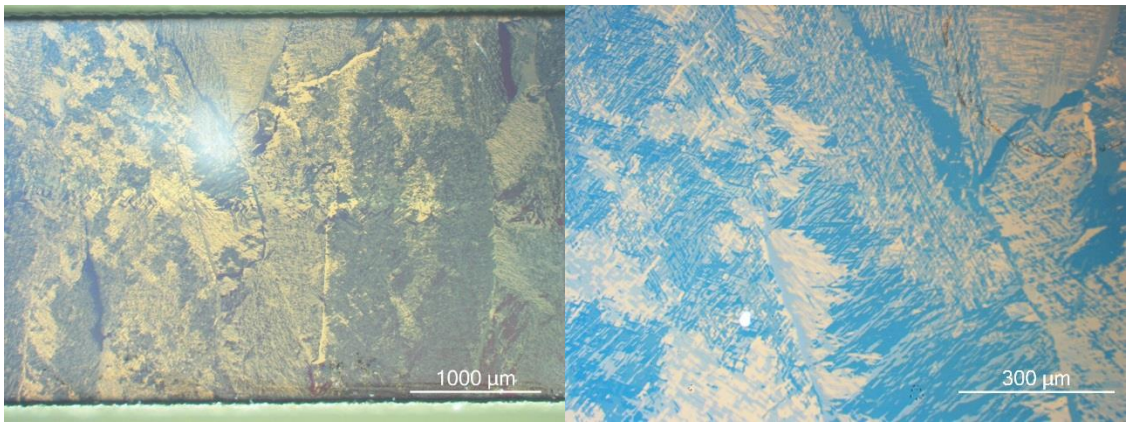

Figure 43: Left: The as-received material in polarized light at 2,5x. Right: As-received material in polarized light at 10x One can easily see columnar β-grains, as well as what looks to be lamella structure. The grain boundary α seems to rather limited.

Figure 44 shows the microstructure of sample 1 and sample 4 respectively. Compared to Figure 43 the β-grains are rather large not only in build direction (columnar), but also in the deposition direction. The lamellas that are very clear in Figure 43 is hardly present for the two parallels except towards the edges. In addition the decoration of grain-boundary α seems to be higher after heat treatment. The microstructure can therefore be said to exhibit an even more unhomogenous microstructure than the as-received material.

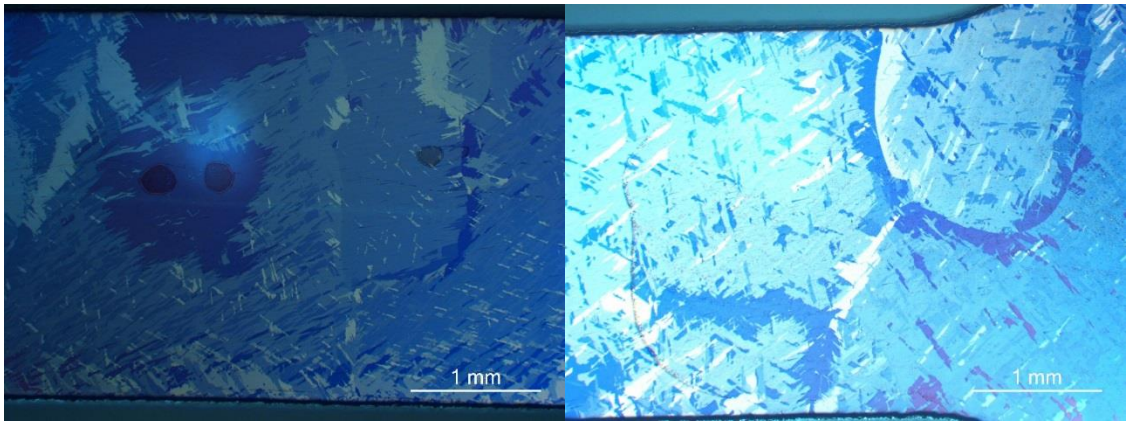

Figure 44: Left: Sample 1 in polarized light at 2,5x, showing the relatively inhomogeneous microstructure that were achieved after solution annealing. It does look as if there's more lamellas towards the edges of the specimen. Right: Sample 4 in polarized light at 2,5x, showing rather large β-grains, with a lot of grain-boundary α decoration

The heat treatment seemed to give a more inhomogenous microstructure. One of the proof of this is shown to the left in Figure 45, where there's a relatively large elliptical grain more or less free for lamellar structure in its interior, using polarized light. In addition, the material towards the edge exhibits features of recrystallization. After etching in Kroll's reagent (right image in Figure 45), it was however shown that the grain in fact was build up by a lamellar structure. The black pores towards the edge becomes more evident after etching.

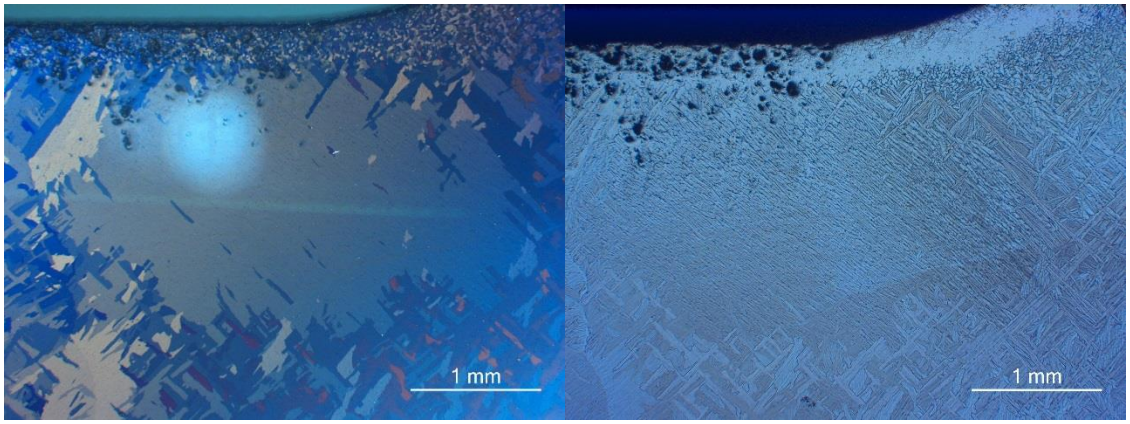

Figure 45: <u>Left:</u> Sample 2 in polarized light at 2,5x, were there's obvious that a grain refinement have occured towards the edge. In addition there seems to be some pores (black areas) towards the edge. <u>Right:</u> The same area as to the left, but after etching. What seemed to be a compact grain is actually a grain that contains several fine lamellas.

After etching the samples, a lamellar structure was unveiled as island in the large β-grains, although not continuously distributed (Figure 46), as the islands are scattered throughout the material. Even though exhibiting an lamellar structure, a major part of the material still shows no sign of lamellar structure. As also can be seen in Figure 44, the β-grains are considerably larger than in the as-received material (Figure 43).

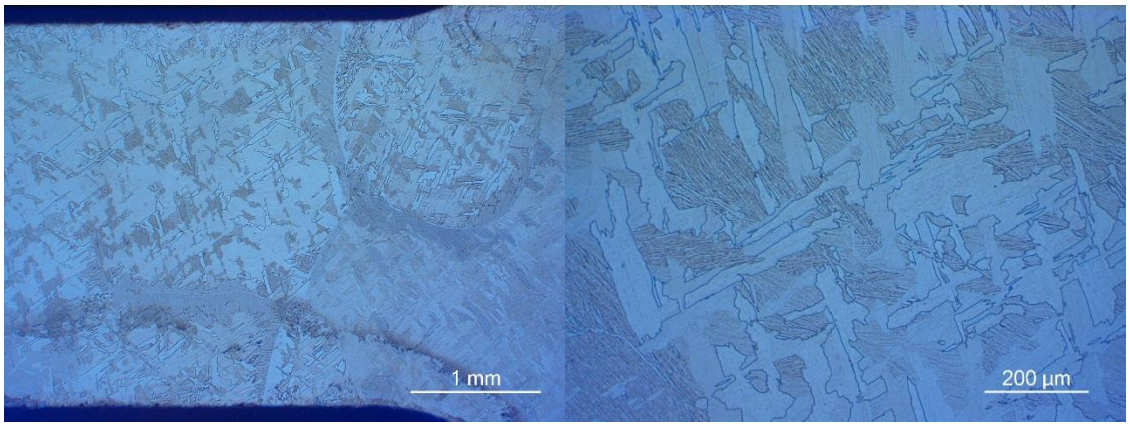

Figure 46: <u>Left:</u> Sample 4 after etching at 2,5x. Large β-grains are observed, as well as a lamellar structure. The lamellar are rather scattered throughout the specimen. <u>Right</u>: Sample 4 after etching at 10x. There are certain regions (islands) showing a lamellar structure, while others doesn't.

4.2.3 Hardness measurements

After spark cutting, some oxidation was observed on the sample surface (Figure 47). This made the author suspicious of oxygen contamination in the samples. For this reason, the microhardness in the region from Figure 45 was obtained. 10 measurements along the edge and 10 measurements in the "bulk" were measured (Table 10).

Figure 47: Showing the oxidation present on the material after spark cutting. The oxidation is observed as a brown/darker surface than the original material.

The microhardness measurements showed a clear difference between the bulk-material and the material towards the edge. There's almost 100HV1 separating the average values of the two regions from Figure 45.

Microhardness (HV1)	Edge	Bulk
Average	540,1	445,8
Standard deviation	31,9	24,2

Table 10: Results from hardness measurements from the edge and bulk region in Figure 45. The load applied were HV1.

4.2.4 Fracture surface in SEM and bright field microscope

Even though the nature of the fracture strongly suggests a brittle fracture, the surfaces were examined in *Zeiss Supra 55 VP* and *Leica* MEF4M. Additional fracture surfaces are displayed in Appendix C. To the left in Figure 48 the contaminated specimens are compared to the as-received material after fracture. The as-received material is deformed throughout the tensile area (1,2,3 in Figure 41), while the contaminated sample shows no deformation at macroscale. Even at microscale (right in Figure 48) the contaminated specimens shows more or less no deformation, with a transgranular-like fracture surface. Fractured surfaces obtained by the use of SE in SEM can be found in Appendix C.

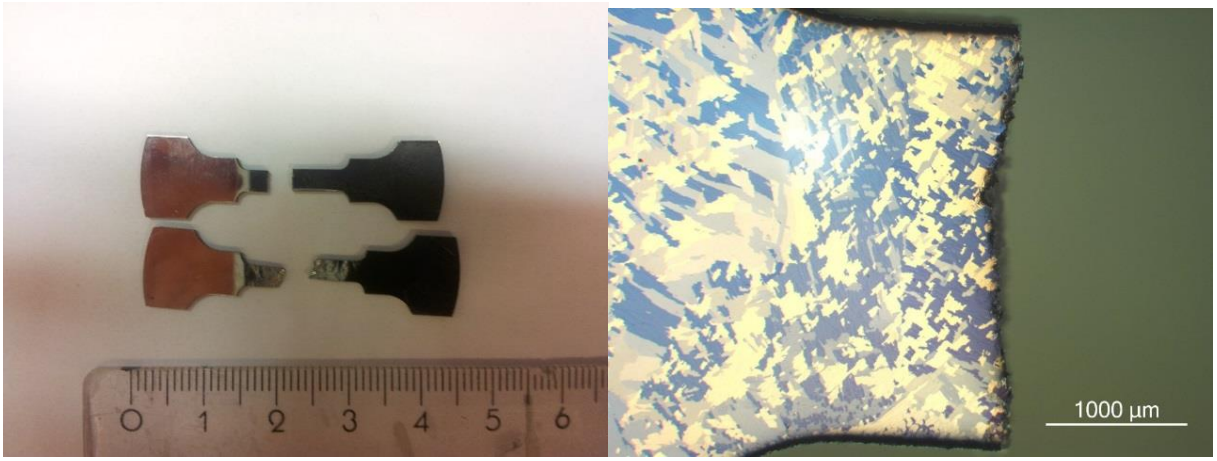

Figure 48: <u>Left:</u> The tensile specimen at the top is contaminated, while the tensile specimen at the bottom is the as-received material. The contaminated specimen fractured around 300 MPa, while the bottom specimen fracture around 10% elongation. <u>Right:</u> Tensile specimen (AC) observed in Leica MEF4M with polarized light. The sample went to fracture before the tensile test could start, i.e. during clamping/fastening.

4.3 Thermal investigation

Four dilatometry tests were performed according to section 3.3.1. The results obtained showed the same trend, and for this reason the results from only one of the experiments is displayed in this section. The three other experiments are showed in Appendix D. The dilatometry tests shows a more or less continuous expansion of the lattice during heating. At cooling a little jump is detected, before the specimen starts to shrinks. The expansion of the lattice during heating, is a little faster than the shrinkage during cooling, i.e. steeper slope.

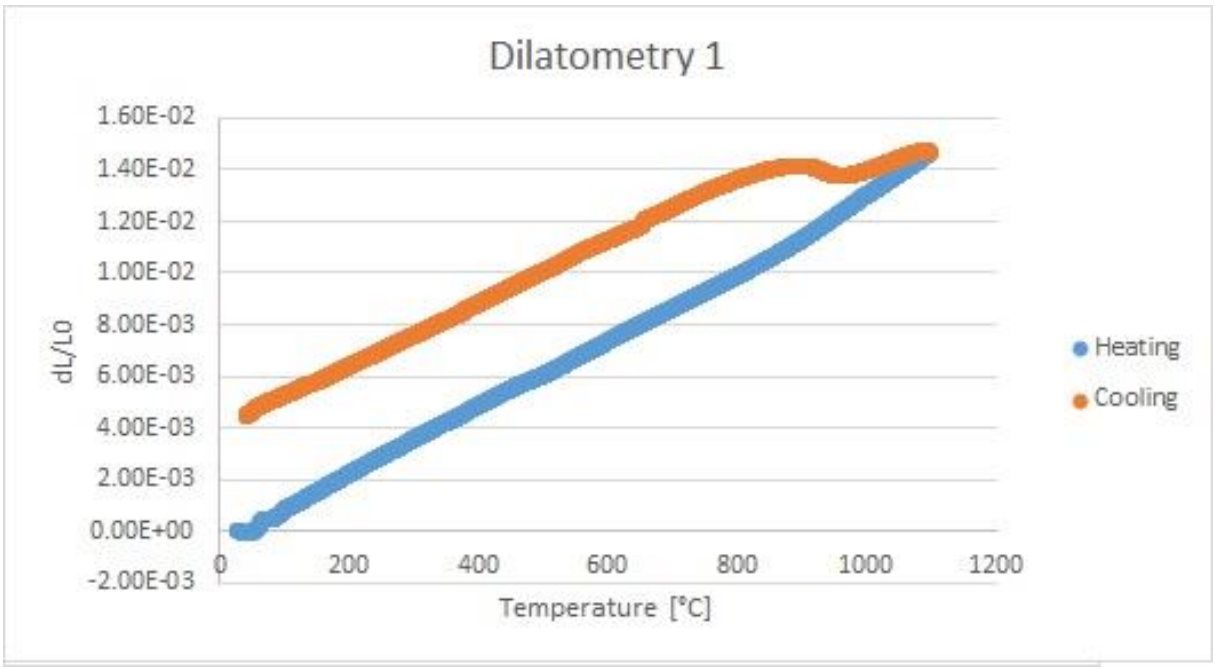

Figure 49: Relative length expansion vs. temperature [°C] for the first dilatometry test. The blue slope shows the heating of the sample, while the orange slope shows the cooling of the sample

5. Discussion

In the following section, the experimental procedures, texture evolution, microdeformation, macrodeformation, microstructure, the contaminated specimens as well as the thermal analysis will be addressed.

5.1 Experimental

Quite a lot of work was spent performing experiments, and even though a well functioning sample preparation technique [1] have already been established, there's certain parts of the procedure that needs addressing.

For the thermal analysis both dilatometry and thermogravimetry differential scanning calorimetry (TG-DSC) were selected as techiques to determine the transition temperature. TG-DSC is a technique that measures both the mass change during heating, as well as endotherm/exothermic reaction in the sample relative to a reference material. The use TG-DSC didn't give in any clear results, and the determination of the transus temperature were not possible regarding the results from these experiments. The dilatometry results are discussed further in section 5.7.

The sample holder used (Figure 19) was new, so a few test had to be performed to confirm that it would work for general sample preparation. The technique used for this were similar to the sample preparation used at the tensile samples (section 3.1). The surfaces finish was if possible better than previous manual preparation considering the CI-index and fit in EBSD (Appendix E). It was however noted that the grinding (section 3.1.2) had resulted in a specimen surface that wasn't completely level. Even though only fractional, this can cause the need to refocus when moving across the sample surface in SEM. It did however not seem to cause any problems regarding the actual results from EBSD.

During examination of the contaminated samples, several techniques were used to be able to characterize the material as good as possible. The use of backscatter detector (BSD) was performed on the parallels (Table 8), to see if any lamellar structure could be obtained. Unfortunately, the signals obtained with 30µm aperture opening was weak, and the images could not be used. When the aperture opening was increased to 120µm the signal were better, but as

a result to a larger aperture opening the noise/signal-ratio increased. As a result, the use of polarized light was concluded to be used for characterization of the microstructure. A possible explanation for this behavior could be that the heat treatment had led to homogeneity of the elements aluminium and vanadium, thus reducing the effect of Z-contrast . As can be seen in [15], the AM material has a rather low contrast with the use of BSD even before heat treatments. The observation of hydrides isn't expected in SEM as they are too thin, and can only be observed by using transmission electron microscope (TEM) or similar techinques.

When observed in the SEM, a thin film were detected on the surface of the specimens that experienced the 1st heat treatment (section 3.2.1). A quick energy-dispersive X-ray spectroscopy (EDS) gave indications that the film were organic as it contained quite a lot of carbon, nitrogen and hydrogen. This film caused some occasional charging of the specimens, making the EBSD scan useless. Except for the occational charging the film didn't seem to have any negative effect on the EBSD results in form of CI-index and fit-values. But it did make it rather hard for the operator to get sufficient contrast in the images when using the secondary electron detector. Usually one would expect this type of organic layer to disappear during the cleansing, either in the ultrasonic bath or by the plasma cleaner. However, no obvious conclusion can be drawn to what, and from where, the film appeared. After some tests, the author suspects the glue from the double sided tape to be the cause of this organic layer. It is thought that the glue would have reacted with the OPS/H_2O_2-mixture, and deposited on the sample surface.

When heat-treating the tensile tests there were some samples that showed warping, especially those with the steepest cooling gradient, i.e. AC. The warping did however not prove too critical for the sample preparation. Even so, it did cause some problems when mounting them to the sample holder (Figure 19) with double-sided tape, as the samples seemed broke loose from the tape at a relatively high frequency (every 2 minutes). Even though the sample themselves didn't suffer any significant damage from this, except some smaller scratches, it did make the grinding and polishing step rather tedious. To try to compensate for this, the force per sample was usually decreased about 5N relative to Table 2 and Table 3. As a substitute for the double-sided tape, a wax (Crystalbond 555) was applied, having a positive effect regarding the loosening of the

samples. The use of the wax as a replacement for double sided tape should be considered for future experiments.

It should be mentioned that the tensile stage used shows a higher strain than actually being the case. Although this would depend on the force during fastening of the specimen, the operator can easily go up to 1.5%-2% elongation right away without any plastic deformation occurring. There are two major flaws regarding the stress-strain curves from the in-situ tensile tests. One factor is that the gear (or motor) that is controlling the strain, not a dilatometer. As the gear is far less accurate then the dilatometer, there's bound to be some errors as the material is strained. The second factor contributing to this misguided strain are the fact that the specimen is fastened before being inserted into vacuum. This clamping is done manually, and will therefore lead to specimens starting off from different stress-states. For these two reason one can't really use the stress-strain curves obtained to say very much of the quantitative mechanical properties of the material. In addition to these internal errors, the tensile tests performed on the 2nd heat-treated samples (section 3.2.2) had a third error as the tensile stage were in need of calibration. This resulted in a rather inconsistent tensile test where the specimens often were stretched several percent above the elongation typed in by the operator. This made the in-situ process harder to control, and resulted in that some stages of deformation couldn't be obtained.

OIM Analysis 6.1 was used for analysis of the obtained EBSD data. Based on the work of Bridier et. al. [39], the elastic stiffness were investigated to see if the anisotropy of the HCP lattice would have any effect on the deformation mechanism. Tensile tests performed by NTi have stated an E-value of 115GPa for the bulk material, it would therefore seem reasonable to obtain an average E-module at approximately the same value at a micro-level. OIM Analysis uses an elasticity matrix when calculating the E-module. Initial analysis of the material with OIM Analysis 6.1, gave a maximum E-module of 69,5GPa. After consulting with the producers of the software (EDAX), it was confirmed that there had been some problems with calculations of the E-module in the previous versions, and the author was recommended to try OIM Analysis 7. Even though OIM Analysis 7 gave a higher E-module (maximum value: 115GPa), the stiffness was still lower than expected.

It was however observed a certain relation between the minimum and maximum value from OIM Analysis 7 (82GPa and 115GPa) and the minimum and maximum value from figure 13 (100GPa and 145GPa). For this reason, a scaling of 1.24 of the original elasticity-matrix in OIM Analysis 6.1 were performed based on the following calculation:

$$0{,}5 \cdot \left(\frac{145}{115} + \frac{100}{82}\right) = 1{,}24$$

By scaling the elasticity-matrix, the E-module became more trustworthy regarding the tests performed on the bulk material, and was therefore chosen as the correct matrix for calculating the E-module of the anisotropic HCP lattice (Appendix F). During calculations of the E-module, it became evident that OIM Analysis 6.1 (and OIM Analysis 7) still had problems calculating the stiffness of the anisotropic HCP lattice, as it frequently calculated values that didn't have any basis in theory (Appendix F). The correct scaled E-module were eventually obtained, and used for further analysis.

5.2 Texture

Texture can play a significant role, for example regarding the stiffness of the titanium, because of the anisotropy of the HCP structure [50]. Unfortunately there have not been performed much research regarding the texture of HCP materials, especially not for material produced by AM. So a detailed discussion of the microtexture and its evolution is not performed in this project. Earlier studies on the texture of AM Ti-6Al-4V have made it clear that a relation between the properties and the texture, is not at all straightforward [23].

There are some points that should be mentioned regarding the texture memory effect. As can be seen in Figure 24, Figure 25 and Figure 26 there isn't really any tendencies towards loss of texture after heat treatment, which one might would expect after heat treatment. The intensities of the peaks in the contoured pole figures does not change significantly after heat treatment. This is caused by the strong orientation relationship (section 2.3) and the variant selection, which makes titanium rather unique compared to more conventional materials such as steel and aluminum.

The blocks (Figure 17) used in production has a large thickness, while a thin sections (1-5 mm) will show a significantly lower variant selection and texture [51]. This is mainly because of the amount

of small β-grains with a different orientations being formed at the surface of the material, leading to a wide variety of possible variant selections of the α-phase along the specimen. An AM production technique using the effect thin sections could prove to give a more isotropic material, at the expense of the characteristic columnar grains.

Although highly anisotropic and dependent on thermal history, the similarities of the texture between the different planes can be observed [23], usually with a 4 or 5 peaks around the center in the (0001) contoured pole figure (Figure 24 - Figure 26). A strong texture component is reported perpendicular to the build direction (X/Y-plane) [26], but it can be concluded that the presence of a strong texture in the x/z-plane is also very much present.

The α-phase present during annealing is determining for the texture after cooling, the higher the amount of α-phase present at the annealing temperature, the higher the texture memory effect [52]. It is therefore rather difficult to remove the texture achieved after AM completely, unless a detailed overview of the phase distribution at high temperature is applied. Although not desired, a treatment of Ti-6Al-4V in the β-region will lead to drastic changes of the texture [50], but has drawbacks in the form of a rather different microstructure than in the as-received material. The β-grains achieved after deposition are already highly elongated, and an increase in the grain size would usually not be favored. In addition, the presence of α' would not be desirable when working towards an increased ducility. The amount of high angle grain boundaries would have an effect on the texture during heating [21]. This indicates that a smaller and more spherical β-grain morphology, would lead to a more isotropic material. Unfortunately, this is hard to achieve by AM.

The variant selection during β→α transformation is very strong, and will always be present. One way of coping with the problematic related to texture of AM material, would be to tailor the texture and properties of each different components, by an intense control of the process parameters [26] and geometry. This would require a technical breakthrough regarding beam motion to interrupt the growth of columnar β-grains, and as far as the author know, this has not been done yet. Products with thin cross sections has proven [51] to decrease the anisotropy, as compared to thick blocks with a longer and more complicated thermal history.

5.3 Microdeformation

Compared to other conventional techniques for producing Ti-6Al-4V the AM process has the advantages of reduced cost and time. But up to date it's use have been limited to parts in airplanes and medical implants, the anisotropic behavior being one of the major reasons for this restrictive usage. Even for the more convential production techniques, Ti-6Al-4V exhibits inhomogeneous deformation [42]. And a complete understanding of microstructure, texture, thermal history and their correlation is needed to obtain a full knowledge of the alloy and its properties.

The α/β-interfaces have been reported to be areas for dislocation build-up [41], for Ti-6Al-4V produced by forging or casting. However, the β-phase found in the material from NTi is very limited [9], as can be seen in Figure 38. Based on its CI-index (approximately 0,05) the β-phase will not be regarded as reliable enough to be used for further analysis.

The mechanical AM produced Ti-6Al-4V is very dependent on which directions that are tested (build, deposition or transverse direction), and process parameters such as feeding of wire or powder, interpass temperature, geometry and deposition rate. The tensile test performed at SINTEF (Appendix B) does not show as high anisotropy as observed by Baufeld et. al. [5], and could in fact be considered as a relatively isotropic material when compared to other AM techniques. This shows that NTi has come a long way improving the AM technique already, but there's always room for improvement. By the use of post build-up heat treatments, the mechanical properties of AM can be competitive to both cast and wrought material [30]. A drastic decrease in the strength of the material is however not expected during the heat treatment, as compared to many other structural materials.

Twinning is generally not present as a deformation mechanism in monotonic tensile tests of Ti-6Al-4V at room temperature [36], and is therefore not studied any further in this project. As the AM is intrinsically anisotropic [17], the orientation in the material is crucial for its behavior during deformation. This have usually been related to the different amount of β-grain boundaries in the build and deposition direction, and can be to a certain extent be explained by the Hall-Petch

relation [53]. It is however obvious that other factors than the β-grains will influence the mechanical properties.

Due to its anisotropy, there's a non-uniform strain among different regions in the material, making the Taylor factor somewhat undescriptive [54]. Although Eriksen [9] has used the Taylor factor in earlier studies, its application for this material is limited. The Schmid factor (section 2.5.2) ranges from 0 to 0.5, and was chosen as one of the parameters describing the deformation in Ti-6Al-4V. To be able to fully understand the nature of slip in the material, other aspects as well as the Schmid factor has to be considered. The activation of a slip system would also depend on the E-module, in addition to the Schmid factor [39], where a low stiffness would promote an easier activation than a lamellae with a high E-module.

Bridier et. al. [36] stated that a Schmid factor of 0.35 is needed in Ti-6Al-4V before slip could occur, for both the prismatic and the basal slip systems. The CRSS of pyramidal slip is high compared to both prismatic and basal slip, making it less prominent as a deformation mechanism [42]. Pyramidal slip do occur, but rather scarcely, and can be hard to detect and is therefore neglected as a deformation mode in this project. It is hard to differentiate slip lines from microcracks in the EBSD images. For simplicity, all observed deformation will be referred to as slip lines.

Based on general mechanics in a homogenous bulk, one would assume slip and eventually cracks to occur perpendicular to the stress axis. This also seems to be the case for this material (Figure 27, Figure 32 and Figure 39 and Appendix G), although they are somewhat restricted by the alpha lamellas and would therefore be slightly tilted in the build-direction. This restriction experienced by the slip lines from the lamellas can especially be seen for Figure 39 and Figure 40. In Figure 27 and Figure 30 it can be seen that slip travels across several lamellas before being arrested [41]. For slip to cross lamellas they need to have a similar orientation, promoting the same kind of slip. The slip can, when subjected to sufficient deformation travel across relative large distances of lamellas with an unfavorable orientation [36], before reaching a colony with a more preferable orientation. In the same way, the lamellas can work as slip/crack arresters if the misorientation between them are sufficient (Figure 36 and Figure 37), or the deformation for slip transmission is insufficient.

When the c-axis of the HCP-lattice is parallel with the stress-axis, all type of $\vec{a}$ slip (section 2.5.1) will have a very low Schmid factor. The grains will have a hard time deforming and is therefore referred to as a hard grain [38]. A lamellae with the c-axis perpendicular to the stress axis will deform easily, and is therefore referred to as a soft grain. When a hard and a soft grain have a boundary in common, this will lead to strain and dislocation build up within the soft grain. Hard/soft grain (or lamellae) deformation can be observed for slip 2 and 4 in Figure 40, where there's two pairs neighboring lamellas having their c-axis orientated very different. In both slip 2 and 4 (image c in Figure 40), one of the lamellas has a c-axis close to perpendicular to the stress axis, exhibiting a blue color indicating a low E-module. While the lamellas on the other side of slip 2 and 4 have a higher stiffness, up towards 30 GPa higher, and thus a yellow color. The two lamellas with its c-axis that's close to perpendicular to the stress axis (soft grain), will deform easily with an $\vec{a}$-type slip system, while the stiff lamellae would generally require a higher stress before any slip is observed.

The two stiff lamellas will have a tendency for slip in the basal plane. The Schmid factor for basal slip is very high (Figure 40), but for a hard grain to obtain slip in the basal plane, intermediate values of the Schmid factor is usually preferred [39]. The strain will therefore accumulate in the soft grain as prismatic slip toward the boundary, and eventually penetrate across the boundary into the hard grain leading to a cleavage type of slip. These areas with a hard/soft-grain combination are often referred to as "hot-spots", and could reach strain 3-3,5 times the surrounding material [42] before slip or crack formation occur. Slip 1 and 3 in Figure 40 originates from within a grain with a low stiffness and high Schmid factor for prismatic slip. The slip eventually encounters a somewhat stiffer grain, with a preferred slip in the basal plane, and will stop relatively quick upon encountering them.

In Figure 27 there's seem to be a clear accumulation of slip towards one of the β-grain boundaries. When observing the stiffness (Figure 29) of the material, the slip seems to be restricted to the region with a relative low stiffness (100-110GPa) and grow towards the grain boundary, which also exhibits a low stiffness. The the two other grains in the image has a higher E-module (yellow and green in Figure 29). As a result, they are sheltered for slip at the given strain, although the Schmid factor for basal slip (Figure 28) would indicate rather high affinity towards slip throughout

both grains. It should be noted that the Schmid factor for prismatic slip (Figure 28) shows tendency towards slip in the same region as the material with low stiffness. It's likely that the combination of both these two factors are determining for the slip observed in Figure 27.

Even though a greater portion of the ROI in Figure 28 indicates slip by the basal rather than the prismatic plane, prismatic slip seem to grow easier (Figure 30). The prismatic slip will grow from the right along grain 3, before eventually passing through grain 1 in Figure 31, and eventually ending up at the β-grain boundary. There's a small accumulation of strain at grain boundary before crossing the grain boundary into grain 1, relative to the surrondings. But because of an almost similar orientation in grain 1 and 3, the accumulation is limited and slip transverses rather easy into the next lamellae [22]. The angle at the grain boundaries between the three grains are approximately 60°, but grain 2 has a rather different orientation than grain 1 and 3. To prevent crossing into the 2nd grain with a lower Schmid factor than grain 3 (Figure 30), the slip travels along the boundary between the 3rd and 2nd grain. A larger width of grain 1 would not have caused any significant arrest of the slip line, as both grain 1 and 2 promote the same slip system it will continue without any arrest. The strain will build up along the β-grain, leading to propagation along the boundary, and eventually fracture [11].

The deformation in Figure 32 is highly localized towards the β-grain at the bottom. The stiffness in the bottom grain is seen to be continuously lower than the two surrounding grain (Figure 33), although lamellas with a similar low stiffness can be found in the two other grain as well. Because of the significant lower stiffness, the deformation in the grain is significantly higher propagating towards the boundary. As can also be seen in the SE images in Figure 32 the deformation is very heterogeneous, and shows the influence of columnar β-grain during deformation. The slip will not move across the boundaries because of the difference in orientation of the two grains [22], but rather lead to a build-up of strain along the boundary. The slip occurring in the bottom grain would be both prismatic and basal, which is in accordance with the Schmid factor, as well as hard/soft grain deformation (Figure 32 - Figure 34).

The slip along the grain boundary (Figure 32) shows strong resemblance to the rogue grain effect reported by Dunne et. al. [38]. For line segment 1 (image c in Figure 35), a grain boundary angle

of 60° between the hard and soft grain is measured. The basal slip plane of the hard grain will coincide with the prismatic slip plane of the soft grain [38], which is caused by a crystallographic reorientation of the two slip planes at the grain boundary. For the second line segment (image d in Figure 35) the grain boundary angle at 41° could indicate that much strain would be carried by the grain with a lower stiffness, before slip finally occurs across the boundary by a cleavage-mechanism.

The β-grains seems to play a crucial role during deformation as slip seems to propagate towards the boundaries, although the slip themselves usually originates from the lamellas. The sensitivity of the grains could however be controlled by the amount of grain boundary α. By decreasing the amount of this soft phase at the boundaries the initiation of crack will be decreased. The grain-to-grain orientation of the β-grains also plays a crucial role, as the grains in this report have shown a rather anisotropic behavior to the acceptance of deformation. This behavior would seem to be strongly related to the stiffness of the grain (Figure 27 and Figure 32). When a large amount of the lamellas towards a grain boundary has a low E-module, slip will initiate from there rather than in surrounding stiffer grains, before it propagates further towards the boundary.

The 1st, 2nd and 3rd slip line (basal) in Figure 37 is restricted by the width of lamellar structure, which again confirms the importance of the width of the lamellas in the material. The fourth slip line in Figure 37 seems to travel a short distance into a new α-structure that shows a tendency towards prismatic slip, before being restricted by orientation of the lamellae. No clear difference where found in the grain angle between the 1st, 2nd and 3rd with respect to the 4th. In the literature it has been reported that basal cracks appears earlier and propagates faster than prismatic cracks [39], although this effect isn't very clear in this study, except for in Figure 36 and Figure 37 where there's a substantial amount of basal slip early in the deformation of the specimen.

Although not observed nearly as much as the prismatic, basal slip does occur in AM produced Ti-6Al-4V, as seen in Figure 36. The reason for the tendency towards prismatic slip are caused by the c/a-ratio of the HCP structure in α-titanium, giving a lower CRSS for prismatic gliding, as compared to basal slip [36]. By increasing the amount of oxygen and aluminium in the alloy, this effect can be changed towards pyramidal and basal slip respectively [36]. A chemical analysis of the material

have not been performed, but it's assumed that the oxygen content is well below the accepted values, so the presence of twinning and pyramidal slip is limited. The basal slip lines have been reported to be of a finer nature, and more homogenously distributed, as compared to the prismatic slip lines which are coarser and more clearly spaced [39]. A significant difference between the morphology of the two slip systems has not been observed in this project. There are however indications towards that the prismatic slip are more flexible, and less restricted by the orientation of its surrounding. For this reason, one can state that the prismatic slip lines is less homogenous as they are not as restricted to orientation as the basal slip. Example of this is in Figure 40, where the prismatic slip travels a short distance into a new lamellae with an non-preferable orientation before stopping. There's a possibility that this type of prismatic slip will be transmitted to a new α-lamellae with similar orientation at higher strain [39].

The width of α-phase clearly has an effect on the mechanical behavior of TI-6Al-4V. Which effect the α-width has is not perfectly clear, as it has been claimed to affect both ductility [40], and the ultimate tensile strength [17]. Observing the results in this project, the effect of the α-width have to be complemented with the orientation of the neighbouring lamellas. If the neighbouring α-phase has a different orientation, with a large shift towards a different deformation mode, the slip will most likely stop upon reaching the boundary. For a large misorientation, and thin lamellae width, the deformation will stop relatively early, leading to a higher strength, but a lower ductility. With a larger width of the α-phase, the ductility would increase, as the slip would cause more deformation, before being arrested by a neighboring lamellae. With a neighboring α-structure promoting the same slip system, the width of the α-phase would seems to be of less importance, as the slip transfers rather easily into the neighboring lamellae.

5.4 Macrodeformation

The microstructure of the as-deposited material is as mentioned highly anisotropic, and very dependent on direction of the stress [30], especially regarding the ductility. The anisotropic nature of the material can also be observed for the mechanical tests performed on the as-received material at SINTEF (Appendix B), although not as anisotropic as observerd for Baufeld et. al. [5]. The two tensile specimens seen in Figure 42 have approximately gone through the same

amount of strain. Due to fastening and problems with in-situ stage (section 5.1), the strain difference can in reality be in the range of a few percent elongation.

For the as-received material, the deformation is concentrated towards the columnar β-grains (Figure 42). The β-grain are thought to play a crucial role during deformation [22], because of the grain boundary α being deposited during cooling from the α/β-field. Certain boundaries shows more deformation than others do, with continuous deformation through the entire grain, while other areas shows a more discontinuous deformation behavior within the β-grains. The FC material (Figure 42), exhibits a higher degree of deformation, as well as more homogenous. As the β-grains are supposed to remain unchanged during heat treatment, the change in deformation would have to be explained by the α-phase [41]. It is likely that the discontinuous microstructure in the FC material promotes slip to propagate homogenously through the grain, instead of having a build-up of strain towards the grain boundaries.

Both strength and ductility are reported to increase with solution annealing at 950°C for 1 hour [34]. The observed higher deformation for the FC material, is most likely an effect of the heat treatment performed on the material (section 3.2), giving more discontinuous lamellas. The better part of the deformation in the FC material is limited to the central part (region 2 in Figure 41) of the tensile area. The surrounding area still shows some similarities to the as-received material, where the deformation is concentrated towards β-grains.

The inhomogeneous deformation is clearly seen in Figure 32, as one colony deforms much more than the surroundings, giving rise to the suspicion that the α-colonies are a crucial microstructural unit regarding the mechanical properties [55]. As can be seen in Figure 33 there's a clear anisotropic nature between the grains in the AM material. As the deformation concentrates around the β-grain boundaries, it is obvious that also the β-grains is crucial for the deformation of the AM material, although to a lesser extent after the heat treatment.

5.5 Microstructure

Although being extremely complex to control, a desired microstructure can be obtained by controlling the parameters of the AM process. An alternate way of achieving a desired microstructure is by heat treatments. The heat treatments performed on the Ti-6Al-4V alloy is based on the desire to improve the mechanical response of the material, by increasing the isotropy and ductility. β-annealing was not an alternative in this project, as the columnar β-grain structure from the deposited material will be removed and replaced by more spherical β-grains [32], thus removing the AM footprint on the material. In addition, this type of heat treatment often leads to a brittle structure, as the material becomes extremely sensitive to the cooling rate [27], and the development of α' is likely.

By heat treating in the α/β-region (as done in this project), the β-grain size is assumed to remain more or less unchanged [32]. Both phases (α/β) wants to grow, and as a results of this they are both restricted by the other phase [27]. The cooling rate is the major parameter controlling the morphology of the α-lamellas in heat treatments high up in the α/β-region. It is therefore expect a thicker Wiedmanstätten structure after furnace cooling [17], as compared to the AC material. By comparing the two heat treated materials, this effect can to some extent be observed. The lamellas in the FC material seems to be more discontinuous (Figure 36) than the lamellas in the AC material, which shows resemblance to the basketweave structure (Figure 39). The restriction put on the slip lines by the lamellas in the FC material would be smaller, as slip could grow further because of the more discontinuous lamellar structure.

Unfortunately, the calculations of the aspect ratio (Appendix H) in OIM Analysis 6.1 could not confirm this indication of microstructural change, as reported by Zhang et. al. [40]. The width of the α-lamellas seems to remain more or less unchanged, although this is somewhat hard to confirm as the areas in this study has been limited to the grain boundaries and not the bulk of the β-grains. The α-lamellas in the as-received material (Figure 27) has an inhomogeneous morphology, where some of the lamellas has a significantly smaller width than the lamellas after heat treatment. It would seem as if the lamellas gets a more homogenous α-width as a result of the heat treatment. This is in contrast to the observations done by Lu et. al. [33], who observed a similar α-width before and after solution annealing with subsequent air-cooling. After longer

solution annealing times the microstructure would show a greater increase in the α-width, eventually ending up with a globalized morphology.

There have been reports of a crab-like morphology of the α-lamellas after annealing towards the transus temperature, with air-cooling [33]. The crab like morphology is known to increase the hardness of Ti-6Al-4V. Although the data concerning the microstructure is too small to make any clear statements, there seems to be a morphology in certain regions of the AC material with a resemblance to the crab-like morphology (Figure 40), as well as in the FC material (Figure 36). The crab-like morphology is very sensitive to temperature, and forms approximately 15-20°C below the transition temperature.

The grain boundary α will as a result of heat treatment become more discontinuous [33], and it can be which is observed when looking at the as-received material (Figure 27) contra the heat treated materials (Figure 32 and Figure 39). The amount of grain boundary alpha for the as-received material seems to be greater than after heat treatment, as well as more continuous. Even though the deformation still seems to concentrate around the grain boundaries, cracks will not initiate and grow as easily as in the as-received material, since the soft grain boundary α is more scattered. As expected, the grain boundary alpha in the FC material has a more discontinuous morphology than the in the AC material, due to a lower driver force during cooling.

The microstructures in AM produced Ti-6Al-4V is extremely complex, and is a result of solidification, production parameters, kinetics and heat treatments [26]. The initial microstructure produced during deposition of Ti-6Al-4V would be of great importance, and data regarding the temperature gradient during production would be needed. Titanium has a very low heat conduction, and it would seem likely that a substantial part of the heat put into the material during heating would accumulate just beneath the deposition surface. Leading to very localized microstructural alterations, as the heat are conducted slowly towards the deposition plate. It is likely that most of the heat transfer occur in the form of conduction [34], while radiation and convection are secondary sources for heat loss. The temperature gradient would therefore be at its highest close to the deposition plate, which also can be observed in the microstructure [17].

5.6 Premature fracture

The samples heat-treated in the ReSiNa furnace (section 3.2.1) showed an extremely brittle behavior, in sharp contrast to the reported effect of heat treatment on AM material [56]. The specimen fractured during the clamping in the tensile stage (Figure 23), or just after staring the EBSD tensile test (around 300MPa). Contamination of hydrogen was thought to be the most likely reason for this surprising behavior, which was confirmed by chemical analysis (Table 9). In addition, the microhardness measurements revealed a high probability of oxygen contamination called α-case [2]. A combination of both hydrogen and oxygen [57] are thought to cause the brittle behavior. As can be seen in Figure 48 the fracture is very brittle, as more or less no deformation is observed at the surface of the contaminated material. Although being an artefact, this behavior are thoroughly discussed in the following section, as it is might be an important aspect for future research.

Three events points out for causing the contamination in the specimens. The first event is related to the spark cutting. The material had been the spark cutted in pure water, before being subjected to a heat treatment. The temperatures will be high at the sample surface and the possibility for hydrogen and oxygen absorption onto the sample surface is present. It can be seen in Figure 47 that oxidation has taken place during spark cutting. Further diffusion of the hydrogen oxygen will then continue during the solution annealing and aging. This scenario is however not very likely, as water conducts heat very effectively away from the sample surface.

The second event causing this unexpected behaviour is the atmosphere in the ReSiNa (Figure 21) furnace. Even though the chamber were evacuated to 80 mtorr prior to heating. It is however not unlikely that moisture could have found its way into the chamber, in the form of gas or deposits inside the chamber. A third explanation is that the surface of the samples were contaminated by particles, dust and other impurities prior to the heat treatment. Even though the samples were cleaned in ultrasonic bath (Struers Metason 120) with acetone for several minutes before the treatment, as the rough edges of the specimens after the spark cutting might yet contain impurities. The alumina cups is also a possible source to contamination, as moisture and dirt could have deposited on their surface.

5.6.1 Hydrogen contamination

It was the recrystallization at the edges, especially Sample 2 (heat-treated with furnace cooling and aging) as seen to the left in Figure 45 that first caused the suspicion for hydrogen contamination (section 2.2). The other samples show a somewhat varying degree of recrystallization, usually in the form of lamellar α-precipitates at the edges. Recrystallization could also occur as an effect of a highly deformed material, but as the tensile samples was performed by spark cutting, the amount of deformation in the material should be minimal, making such a level of recrystallization unlikely.

The absorption of hydrogen occurs at a threshold temperature [57, 58] in Ti-6Al-4V. Upon reaching the threshold temperature the absorption of hydrogen increases abrupt, before steadily decreasing towards the transus temperature. Even though the threshold temperature ranges from about 400°C up to 600°C depending on microstructure, it's obvious that this temperature have been exceeded during the heat treatment.

Detection of hydrogen is rather complicated, being the smallest element (atomic number 1) making it very hard to verify the presence of the element, both as interstitial and hydride. Even though the nature of the hydrogen in the material wasn't examined any further, it's likely that the hydrogen were present in both solid solution and as hydrides. One of the most common ways to confirm the presence of hydrides in titanium is by using TEM.

The chemical analysis performed on the samples (Table 9), gives a clear evidence of hydrogen contamination. With a factor 2-2.5 higher hydrogen contamination than in the as-received material. It's likely that the amount of hydrogen have been even higher during tensile testing, since the samples have been stored at room temperature for several months before being examined for its hydrogen content. With the high diffusivity of hydrogen in titanium it's likely that hydrogen would have escaped through the sample surface during this time. In addition, the contaminated samples was kept in vacuum for several hours during the initial testing in the SEM. A vacuum process, even at room temperature, is likely to speed up the diffusion rate of hydrogen. The hydrogen content in the as-received material should be noted, even though much less than

in the contaminated samples. Whether the amount of hydrogen in the as-received material would have any significant effect on the deformation mechanisms in the material is not known.

The diffusion is very high for hydrogen, so it's not unlikely that the samples could be contaminated by hydrogen several micrometers into specimen, although the recrystallized region in Figure 45 only seems to be some 300µm thick. The presence of hydrogen can also be indirectly observed in other ways, such as the formation of martensite [58]. The rather large spherical β-grains (Figure 44 and Figure 45) gives indications of a temperature significantly above the transus temperature, where grain growth have occurred [27], and the old columnar structure have disappeared.

The direct effect of the embrittlement in Ti-6Al-4V caused by hydrogen are interstitials, and the formation of TiH_2 (δ-phase) precipitates [2]. In addition there could be increased precipitation of both the intermetallic phases TiAl (γ-phase) and Ti_3Al as a result of hydrogen in titanium [58]. There have also been reports the formation of martensite both the α'-type and the orthorhombic α''-type [59] in the presence of hydrogen. The presence of interstitial hydrogen, hydrides, intermetallics and martensite will lead to an extremely brittle behavior. Unfortunately, all of these phenomenons are rather hard to investigate with the techniques applied in this report.

The amount of hydrogen going in solid solution in the α –phase is in the range of 125-150ppm [2]. The actual amount will depend on the microstructure, as the hydrogen will tend to diffuse along the α/β grain boundaries [60]. The amount of hydrogen able to go in solution for the β-phase is significantly higher than for the α-phase [61]. As the solution annealing were performed high in the α/β-region, the amount of β-phase will be significant, but will decrease drastically during cooling. The contaminated specimens would therefore be able to dissolve a high amount of hydrogen. A greater part of this hydrogen would upon cooling form hydrides, because of the lower solubility in the α-phase. When the solubility limit is reached the hydrides will start to grow inwards from the grain boundaries. As there is a large volume misfit between the hydrides and the titanium there will be a stress field subjecting the surrounding matrix, which in time can lead to micocracks [62]. The presence of significant internal stresses in the material originating from production is unlikely, as the heat treatment should have removed them.

The hydrogen in solid solution will place itself in one of the three possible slip directions in the basal plane, significantly decreasing fracture strength [2]. The reason for the hydrogen to take the interstitial sites in the basal plane is not fully understood. Hydrides will when subjected to a stress field place themselves as thin plates perpendicular to the stress axis, promoting cracks [2]. There is a stress field subjected to the specimens for a relatively long time, as the samples are clamped in the in-situ tensile device during the evacuation of the SEM chamber for approximately eight hours. During this time, hydrogen will have time to position itself in more favorable positions promoting fracture. As the clamping are done manually, some specimen were fastened under such a stress state that fracture occurred before the tensile test could start.

In Figure 44 there are several large grains having a limited amount or no lamellas in its interior. Compared to the as-received material (Figure 43), the amount of lamellas is very small. The few morphologies in Figure 44 that resembles a lamellar structure are usually too coarse to be categorized as a basketweave or Wiedmanstätten structure. Etching does revealed a lamellar structure of the grain (Figure 46), indicating the likelihood of martensite (α'/α'') formation [58]. This would give a second indication that the temperature during solution annealing have been above transus temperature. The identification of α'-martensite is not possible in EBSD, because of the similarities in crystal lattice XRD have to be obtained to identify the phase. The α'' has a orthorhombic crystal structure, but isn't aveliable for indexing in OIMDC 5.32.

As already stated, there's several evidence leading to hydrogen contamination in the bulk of the specimens. These observations are in contrast to Sozanska et. al. [63], who reported that contamination of hydrogen mainly is observed at the surface, while the bulk microstructure remains unchanged. The reason for observing tendencies towards hydrogen contamination through the entire specimen, is most likely caused by the relatively large surface/volume-ratio (Figure 18). When comparing Figure 43 and Figure 44 it's obvious that that the amount of grain boundary α is higher after heat treatment, which degrades the mechanical properties (section 2.5.4). This is a common effect during heat treatment of Ti-6Al-4V, and is reinforced by a low driving force during cooling (section 2.4).

5.6.2 Oxygen contamination (α-case)

After microhardness measurements on the edge and in the bulk of the material (Table 10), it became clear that the samples most likely had been contaminated by oxygen, in addition to the hydrogen. The phenomenon where oxygen strengthens the α-phase by solid solution is often referred to as α-case [2]. The hardness of the measurements in Table 10 are in good accordance with the results obtained by Chan et. al. [64]. Although no further experiments than the hardness measurements were performed to confirm the α-case, it is very likely that there is some degree of oxygen interstitials present. Figure 47 strengthens the suspicion towards the presence of oxygen, as oxidation can be observed at the material surface.

The presence of α-case will lead to formation of microcracks at the surface when stress is applied, which will be determining for the tensile behavior of the specimen [64]. It might be that in the presence of both hydrogen contamination and α-case that the crack is initiated due to the increased hardness at the surface caused by oxygen, and the growth of the crack is accelareted due to the presence of hydrogen. As the edges after spark cutting is far from smooth, there are many possible areas where a crack can be initiated.

When exceeding 427°C, titanium should be in a protective atmosphere [26]. The contaminated samples should have been heat treated in an inert atmosphere, but the presence of contamination seems to have left the material exposed to oxygen. The solubility of oxygen in α-phase have been reported to as high as 30at%, as the oxygen place itself at interstitial sites in the lattice promoting pyramidal slip [12]. As more oxygen goes in solid solution the material increases its strength and hardness, while decreasing the ductility. The presence of aluminium in the TI-6Al-4V will decrease the diffusion rates of oxygen [2], but can on the other hand lead to the formation of Ti_3Al [12].

5.7 Thermal analysis

Even though the transus temperature for Ti-6Al-4V is known to be right below 1000°C [2], there are factors that can alternate this, such as microstructure and chemical composition. It is for example known that larger beta-grains gives a somewhat lower transition temperature [29]. The heat treatments presented in this paper are done at 950°C, so it's unlikely that any material will have passed the transus temperature, except for the samples contaminated by hydrogen. When carrying out a heat treatment, it would be beneficial to get an exact value for the transus temperature. Dilatometry was a natural choice of method for this type of thermal analysis. Some work related to the use of dilatometry on Ti-6Al-4V do already exist, such as Homoporová et. al. [18]. Even so the published work on the thermal expansion of α/β-alloys is limited, and even less regarding additive manufacturing [65]. As there is a change from HCP to BCC structure, dilatometry was thought to give sufficient results because of the relative difference of the two crystal structures.

The results obtained from four dilatometry experiments (section 4.3 and Appendix D) did not show any significant peaks during heating, but rather a continuous expansion with the temperature. Upon cooling, some minor peaks were observed, as well as a decrease in the slope compared to the heating. The samples used for dilatometry exhibit a brown surface scale, which would indicate that the titanium had reacted with air.

Although these experiments didn't prove any phase transition, similar results had been obtained by Swarnakar et. al. [65] with the use of Netzsch DIL 402C with a heating/cooling rate of 2°C/min similar to the experiements performed in this project. It was suggested that Ti-6Al-4V exhibits this behaviour because of non-equilibrium phases caused by the additive manufacturing. The equilibrium α-phase has a larger lattice constants than the non-equilibrium α (Wiedmanstätten), in addition to an accelerated unit cell expansion of the β-phase upon reaching 500°C. This leads to a similar unit cell volume for α-phase and β-phase at the transition temperature, and a linear expansion of the alloy during heating.

The small peak during cooling (Figure 49) is most likely caused by the β→α phase transition, which is observed because Ti-6Al-4V is closer to equilibrium than during heating [65]. During the

dilatometry experiment the vanadium content in α decreases, while increasing in the β-phase towards equilibrium. This clearly shows the influence that both chemistry and microstructure has on the mechanisms of the transus temperature. The slow heating rate (2°C/min) allows the redistribution of aluminum and vanadium as well as a more homogenous microstructure. It is expected that the material after heat treatment would show some peaks at the transition temperature during heating, as the alloying elements would have been redistributed, and the material is closer to its equilibrium state.

It proved extremely difficult to avoid the brown oxide layer, with the equipment used in this project. Even though the chamber used for the experiments were evacuated and flushed with argon several times prior to heating the oxidation took place. The difficulties related to avoiding this oxide layer shows the extreme reactivity that titanium has towards oxygen and other elements (nitrogen and hydrogen) at elevated temperatures. The oxidation layer observed on the samples will however not have any effect on the results, as the time/temperature aspect is too small for significant inward diffusion [65]. And as dilatometry is a measuring technique that's not sensitive towards changes in the surface, this won't affect the measurements.

6. Conclusion

Based on the results from the experiments performed in this project and earlier work on Ti-6Al-4V (section 8), the following conclusion can be drawn:

- A combination of both E-module and Schmid factor gives a good indication of where slip will occur, as well as how the slip lines will propagate in the material.
- The presence of both prismatic and basal slip were observed, although the prismatic slip is easier activated.
- Slip along boundaries with a hard and soft orientation on each side is an important deformation mechanism, both at β-grain boundaries and between α-lamellas
- The effect of α-width on the material properties depends on its orientation relative to its surroundings. A high lamellae width gives longer slip lines, and thus increase the ductility of the material. When the same type of slip system is promoted in two neighboring lamellas, the slip can propagate across the boundary, increasing the ductility even more.
- The β-grains plays a crucial role during tensile testing, as deformation accumulates at the boundaries. This effect is reduced after heat treatment, and a more homogenous deformation takes place. The anisotropy is however still observed, as certain β-grains is significantly more deformed than others
- The α-lamellas in the AC material has a more homogenous width than the as-received material. The FC material shows a more discontinuous lamellar structure as compared to the as-received material
- No evident change in texture after heat treatment are observed, due to a strong texture memory effect
- The dilatometer cannot be used for characterization of the transition temperature due to non-equilibrium composition and microstructure
- The affinity for the alloy towards hydrogen and oxygen at elevated temperatures are evident. Degradation of the mechanical properties after contamination of both hydrogen and oxygen gives an extremely brittle behavior during tensile testing

7. Further Work

The deformation mechanisms in Ti-6Al-4V should be studied further with the use of the EBSD technique. The deformation mechanisms from the interior of the columnar β-grains should be studied as well as the deformation along the grain boundaries. A study including deformation of larger areas than performed in this project would provide an increase insight in the deformation mechanism, especially regarding the β-grains and α-colonies. The effect of deformation mechanism with respect to alloying elements such as oxygen and aluminum should be studied further. This would probably give insight into some of the deformation behaviour in the as-received material as well.

The study of the microstructural change of the material should in the future be performed for relative large areas in the EBSD (transgranular), to obtain sufficient data not only at the vicinity of grain boundaries. The same goes for the texture, and it's response to heat treatment. Even though the microtexture is important for the deformation, an understanding of the texture effect in this alloy would be beneficial to gain more insight in the processes occurring during heat treatment. To study the texture at a larger scale, XRD should be used.

To obtain an effective heat treatment, the changes in the material during heating are needed. To obtain a transition temperature, a high temperature XRD should be obtained. This work could possibly prove tedious, as the accuracy of the equipment is rather low. However, after obtaining the phase transition data for the alloy, the understanding of the heat treatment and process as a whole will increase.

The affinity of the AM produced Ti-6Al-4V towards hydrogen and oxygen should be studied further. Both regarding the microstructure and deformation mechanisms. This could be done by promoting hydrogen and oxygen contamination in different environments. This type of study should also study which environments that promotes contaminations the most. Finally, a survey of the effect from different production parameters should be obtained. The only way to do this is either by accurate measurements of heat gradients, or by modelling. When all the process parameters are understood properly, the microstructure and texture could be more easily controlled.

8. References

1. Mathisen, M.B., et al., *Characterization of Microstructure and Strain Response in Ti-6Al-4V Plasma Weld Deposited Material by combined EBSD and In-Situ Tensile Testing*. 2013: Trondheim, Norway. p. 17.
2. Lütjering, G. and J.C. Williams, *Titanium*. 2007, Berlin, Heidelberg: Springer-Verlag. : v.: digital.
3. Arcella, F.G. and F.H. Froes, *Producing titanium aerospace components from powder using laser forming.* Jom, 2000. **52**(5): p. 28-30.
4. Wohlers, T.T., *Wohlers report 2013: additive manufacturing and 3D printing state of the industry : annual worldwide progress report*. 2013, Fort Collins, Colo.: Wohlers Associates, Inc. 297 s. : ill.
5. Baufeld, B., E. Brandl, and O. van der Biest, *Wire based additive layer manufacturing: Comparison of microstructure and mechanical properties of Ti-6Al-4V components fabricated by laser-beam deposition and shaped metal deposition.* J. Mater. Process. Technol, 2011. **211**(6): p. 1146-1158.
6. Martina, F., et al., *Investigation of the benefits of plasma deposition for the additive layer manufacture of Ti-6Al-4V.* J. Mater. Process. Technol, 2012. **212**(6): p. 1377-1386.
7. Schjetlein, M. *Norsk Selskap vil lage deler til Dreamliner*. 2013 [cited 2013 24.06].
8. LTD, L.T. *Laser metal deposition*. Research & technical 2013 [cited 2013 15.11].
9. Eriksen, L., *Combined EBSD-Investigations and In-situ Tensile Tests of a Direct Metal Deposited Ti6Al4V-Alloy*, in *Materials Science and Engineering*. 2013, NTNU: Trondheim, Norway. p. 154.
10. Banerjee, S. and P. Mukhopadhyay, *Phase Transformations*. Materials & Mechanical. 2007: Elsevier Science Ltd. 1.
11. Baufeld, B., O. Van der Biest, and R. Gault, *Additive manufacturing of Ti-6Al-4V components by shaped metal deposition: Microstructure and mechanical properties.* Mater. Des., 2010. **31**(Suppl. 1): p. S106-S111.
12. Welsch, G. and W. Bunk, *Deformation Modes of the alpha-phase of Ti-6Al-4V as a function of oxygen concentration and aging temperature.* Metallurgical Transactions A, 1982. **13A**: p. 11.
13. Elmer, J.W., et al., *Phase transformation dynamics during welding of Ti-6Al-4V.* J. Appl. Phys., 2004. **95**(12): p. 8327-8339.
14. Mathisen, M.B., *Direct metal deposition of Ti grade 2: Characterisation of microstructure and mechanical properties*. 2011, University: Trondheim, Norway. p. 53.
15. Vilaro, T., C. Colin, and J.D. Bartout, *As-Fabricated and Heat-Treated Microstructures of the Ti-6Al-4V Alloy Processed by Selective Laser Melting.* Metall. Mater. Trans. A, 2011. **42**(10): p. 3190-3199.
16. Kurz, W. and D.J. Fisher, *Fundamentals of Solidification, Fourth Revised Edition*. 1998. 316 pp.
17. Baufeld, B. and O. van der Biest, *Mechanical properties of Ti-6Al-4V specimens produced by shaped metal deposition.* Sci. Technol. Adv. Mater., 2009. **10**(1): p. No pp given.
18. Homoporová, P.P., C., M. Stockinger, and W. F., *Dynamic phase evolution in titanium alloy Ti-6-Al-4V.* International Journal of Material Forming, 2010. **3**(1): p. 4.
19. Burgers, W.G., *The process of transition of the cubic body-centered modification into the hexagonal close-packed modification of zirconium.* Physica (The Hague), 1934. **1**: p. 561-86.
20. Cass, T.R., R.W. Quinn, and W.R. Spencer, *Growth of hexagonal titanium and titanium-aluminum single crystals.* J. Cryst. Growth, 1968. **2**(6): p. 413-16.
21. Semiatin, S.L., et al., *Influence on texture on beta grain growth during continuous annealing of Ti-6Al-4V.* Mater. Sci. Eng., A, 2001. **A299**(1-2): p. 225-234.
22. Sandala, R.S., *Deformation Mechanisms of Two-Phase Titanium Alloys*, in *Faculty of Engineering and Physical Sciences*. 2012, The University of Manchester.
23. Baufeld, B., O. Biest, and S. Dillien, *Texture and Crystal Orientation in Ti-6Al-4V Builds Fabricated by Shaped Metal Deposition.* Metall. Mater. Trans. A, 2010. **41A**(8): p. 1917-1927.

24. Bermingham, M.J., et al., *Microstructure of cast titanium alloys.* Meaterials Forum, 2007. **31**: p. 6.
25. Semiatin, S.L., et al., *Effect of Process Variables on Transformation-Texture Development in Ti-6Al-4V Sheet Following Beta Heat Treatment.* Metall. Mater. Trans. A, 2013. **44**(8): p. 3852-3865.
26. Al-Bermani, S.S., et al., *The origin of microstructural diversity, texture, and mechanical properties in electron beam melted Ti-6Al-4V.* Metall. Mater. Trans. A, 2010. **41**(13): p. 3422-3434.
27. Vrancken, B., et al., *Heat treatment of Ti6Al4V produced by Selective Laser Melting: Microstructure and Mechanical properties.* Journal of Alloys and Compounds, 2012. **541**(0): p. 8.
28. Ivasishin, O.M., S.V. Shevchenko, and S.L. Semiatin, *Effect of crystallographic texture on the isothermal beta grain-growth kinetics of Ti-6Al-4V.* Mater. Sci. Eng., A, 2002. **A332**(1-2): p. 343-350.
29. Gil, F.J., et al., *Formation of alpha-Widmanstätten structure: effect og grain size and cooling rate on the Widmanstätten morphologies and on the mechanical properties in Ti6Al4V alloy.* Journal of Alloys and Compounds, 2001. **329**: p. 11.
30. Brandl, E., et al., *Additive manufactured Ti-6Al-4V using welding wire: comparison of laser and arc beam deposition and evaluation with respect to aerospace material specifications.* Phys. Procedia, 2010. **5**(Pt. 2): p. 595-606.
31. Mathisen, M.B., *Varmebehandling og sammendragsartikkel*, E.N. Trøan, Editor. 2013, Norsk Titanium. p. 1.
32. Brandl, E., A. Schoberth, and C. Leyens, *Morphology, microstructure, and hardness of titanium (Ti-6Al-4V) blocks deposited by wire-feed additive layer manufacturing (ALM).* Mater. Sci. Eng., A, 2012. **532**: p. 295-307.
33. Lu, Y., et al., *Microstructure evolution of sub-critical annealed laser deposited Ti-6Al-4V alloy.* Mater. Des., 2012. **37**: p. 56-63.
34. Dinda, G.P., L. Song, and J. Mazumder, *Fabrication of Ti-6Al-4V scaffolds by direct metal deposition.* Metall. Mater. Trans. A, 2008. **39A**(12): p. 2914-2922.
35. Wang, Y.N. and J.C. Huang, *Texture analysis in hexagonal materials.* Mater. Chem. Phys., 2003. **81**(1): p. 11-26.
36. Bridier, F., P. Villechaise, and J. Mendez, *Analysis of the different slip systems activated by tension in a alpha/betha alloy in relation with local crystallographic orientation.* Acta Materialia, 2005. **53**: p. 12.
37. Udomphol, T., *Plastic deformation of single crystals*, in *Lecture*. 2007, Suranaree Univeristy of Technology: Suranaree. p. 42.
38. Dunne, F.P.E., A. Walker, and D. Rugg, *A systematic study of hcp crystal orientation and morphology effects in polycrystal deformation and fatigue.* Proc. R. Soc. A, 2007. **463**(2082): p. 1467-1489.
39. Bridier, F., P. Villechaise, and J. Mendez, *Slip and fatigue crack formation processes in an α/β titanium alloy in relation to crystallographic texture on different scales.* Acta Mater., 2008. **56**(15): p. 3951-3962.
40. Zhang, S., et al., *Heat-treated microstructure and mechanical properties of laser solid forming Ti-6Al-4V alloy.* Rare Met. (Beijing, China), 2009. **28**(6): p. 537-544.
41. Gil, F.J., et al., *The effect of cooling rate on the cyclic deformation of β-annealed Ti-6Al-4V.* Mater. Sci. Eng., A, 2003. **A349**(1-2): p. 150-155.
42. Littlewood, P.D. and A.J. Wilkinson, *Local deformation patterns in Ti-6Al-4V under tensile, fatigue and dwell fatigue loading.* Int. J. Fatigue, 2012. **43**: p. 111-119.
43. Sundaresan, S., G.D.J. Ram, and G.M. Reddy, *Microstructural refinement of weld fusion zones in alpha-beta titanium alloys using pulsed current welding.* Mater. Sci. Eng., 1999: p. 12.
44. Hjelen, J., *Scanning elektron-mikroskopi*. 1989, Trondheim: SINTEF. 106 s. : ill.

45. Hjelen, J., *EBSD*, in *Lys- og elektronmikroskopi*. 2012, NTNU: Trondheim, Norway.
46. Randle, V. and O. Engler, *Introduction to texture analysis: macrotexture, microtexture, and orientation mapping*. 2010.
47. *Crystal Orientation Mapping*. 2013, Oxford Instruments: http://www.ebsd.com.
48. Chen, Y., et al., *Optimization of EBSD parameters for ultra-fast characterization.* Journal of Microscopy, 2011.
49. Pedersen, J.H., *In situ strekkforsøk med EBSD karakterisering av HSLA-stål ved romtemperatur og -60°C*, in *Department of materials science*. 2011, Norges teknisk-naturvitenskapelige universitet: Trondheim, Norway. p. 107.
50. Daymond, M.R., et al., *Texture inheritance and variant selection through an hcp-bcc-hcp phase transformation.* Acta Mater., 2010. **58**(11): p. 4053-4066.
51. Antonysamy, A.A., P.B. Prangnell, and J. Meyer, *Effect of wall thickness transitions on texture and grain structure in additive layer manufacture (ALM) of Ti-6Al-4V.* Mater. Sci. Forum, 2012. **706-709**(Pt. 1, THERMEC 2011): p. 205-210.
52. Lonardelli, I., et al., *In-situ observation of texture evolution during α → β and β → α phase transformations in titanium alloys investigated by neutron diffraction.* Acta Mater., 2007. **55**(17): p. 5718-5727.
53. Dieter, G.E., *Mechanical Metallurgy, SI Metric Edition*. 3. ed. 1988: McGraw-Hill Book Company (UK) Limited.
54. Bieler, T., R.L. Goetz, and S.L. Semiatin, *Anisotropic plasticity and cavity growth during upset forging of Ti-6Al-4V.* Mater. Sci. Eng., A, 2005. **A405**(1-2): p. 201-213.
55. Lee, D.-g., et al., *Effects of microstructural factors on quasi-static and dynamic deformation behaviors of Ti-6Al-4V alloys with Widmanstaetten structures.* Metall. Mater. Trans. A, 2003. **34A**(11): p. 2541-2548.
56. Brandl, E. and D. Greitemeier, *Microstructure of additive layer manufactured Ti-6Al-4V after exceptional post heat treatments.* Mater. Lett., 2012. **81**: p. 84-87.
57. Lopez-Suarez, A., J. Rickards, and R. Trejo-Luna, *Analysis of hydrogen absorption by Ti and Ti-6Al-4V using the ERDA technique.* Int. J. Hydrogen Energy, 2003. **28**(10): p. 1107-1113.
58. Zhang, Y. and S.Q. Zhang, *Hydrogenation characteristics of Ti-6Al-4V cast alloy and its microstructural modification by hydrogen treatment.* Int. J. Hydrogen Energy, 1997. **22**(2/3, Proceedings of the Selected Papers of the First International Conference on Hydrogen Treatment of Materials, 1995): p. 161-168.
59. Qazi, J.I., et al., *Kinetics of martensite decomposition in Ti-6Al-4V-xH alloys.* Mater. Sci. Eng., A, 2003. **A359**(1-2): p. 137-149.
60. Tal-Gutelmacher, E., D. Eliezer, and T. Boellinghaus, *Hydrogen's absorption/desorption behavior in gaseous-phase charged duplex-annealed Ti-6Al-4V alloy.* Mater. Sci. Forum, 2007. **546-549**(Pt. 3, Progress in Light Metals, Aerospace Materials and Superconductors): p. 1367-1372.
61. Tal-Gutelmacher, E. and D. Eliezer, *Hydrogen cracking in titanium-based alloys.* J. Alloys Compd., 2005. **404-406**: p. 621-625.
62. Yuan, B.G., et al., *Effect of hydrogen on fracture behavior of Ti-6Al-4V alloy by in-situ tensile test.* Int. J. Hydrogen Energy, 2010. **35**(4): p. 1829-1838.
63. Sozanska, M., *Effect of high-temperature hydrogen treatment on the microstructure and properties of titanium alloy Ti-6Al-4V.* IOP Conf. Ser. Mater. Sci. Eng., 2011. **22**: p. 012009/1-012009/11.
64. Chan, K.S., et al., *Modeling of alpha-case formation and its effects on the mechanical properties of titanium alloy castings.* Metall. Mater. Trans. A, 2008. **39A**(1): p. 171-180.
65. Swarnakar, A.K., O. Van der Biest, and B. Baufeld, *Thermal expansion and lattice parameters of shaped metal deposited Ti-6Al-4V.* J. Alloys Compd., 2011. **509**(6): p. 2723-2728.

9. Appendix

9.1 Appendix A

To show the experimental procedure during this project, the flowchart in Figure 50 is shown. Due to the artefact regarding the contamination of the 1st batch of EBSD samples, additional time was spent on the experimental part of this project.

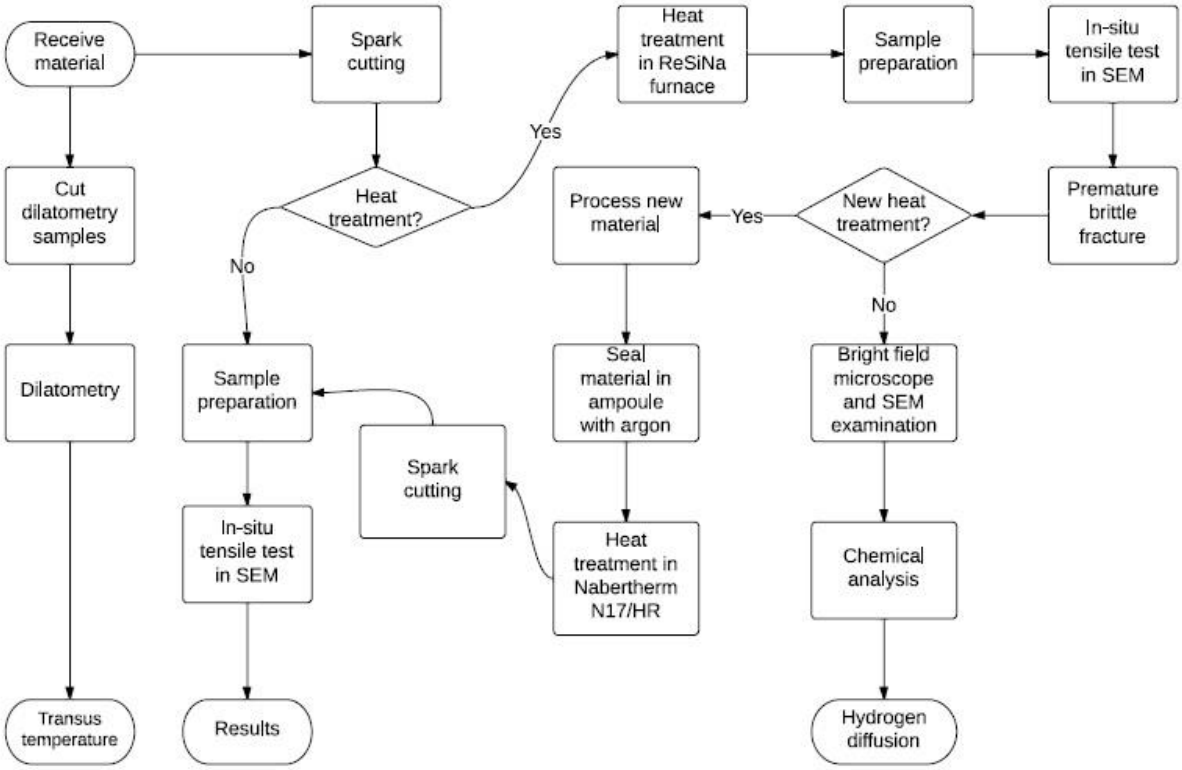

Figure 50: Flowchart showing the experimental process during this project

9.2 Appendix B

Mechanical data from the tensile test performed by SINTEF Raufoss Manufacturing

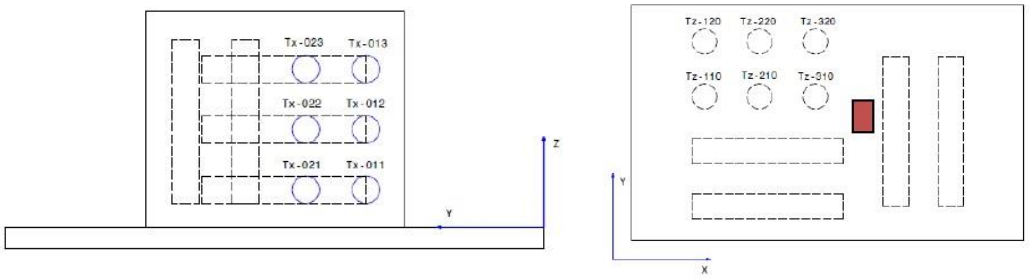

Figure 51: Tensile specimens from SINTEF. Left: Samples extracted from the y/z-plane (deposition direction). Right: Samples extracted from the y/x-plane (z-axis)

Block 29

	Rp0,2 [MPa]	Rm [MPa]	Ag [%]	A [%]
TX	887	968	4,0	7,4
TZ	884	963	3,8	8,5

Table 11: Showing the average value of the mechanical data from the tensile test performed on the as-recieved material. Ag is the elongation (engineering stress-strain) at maximum stress, while A is the elongation at fracture. The values presented are based on four tensile tests according to ASTM E 8M

9.3 Appendix C

Some of the fracture surfaces obtained from the as-recieved material and the contaminated material are presented. Each pair of images in each figure shows the same areas, but at different magnification

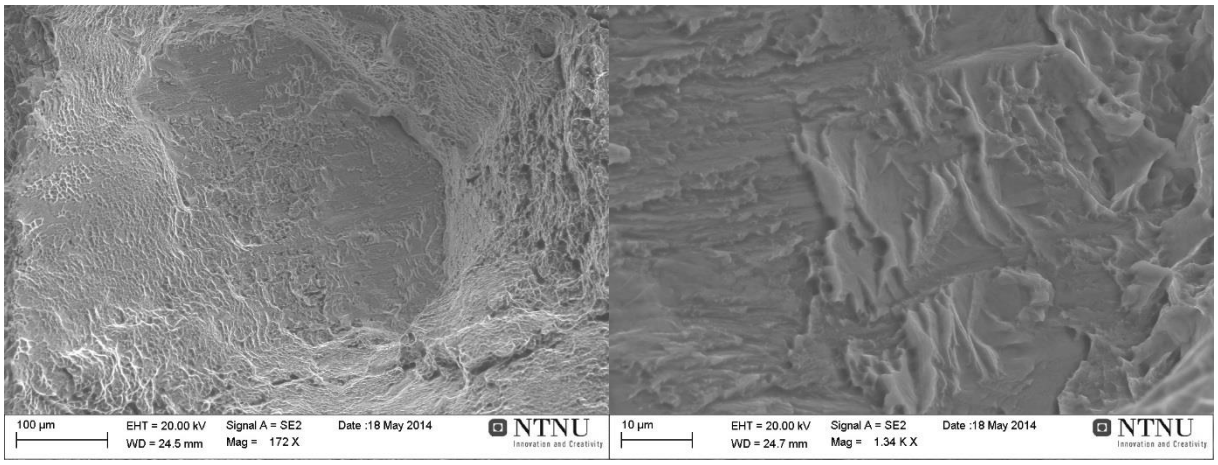

Figure 52: As-received material, at 172X and 1340X

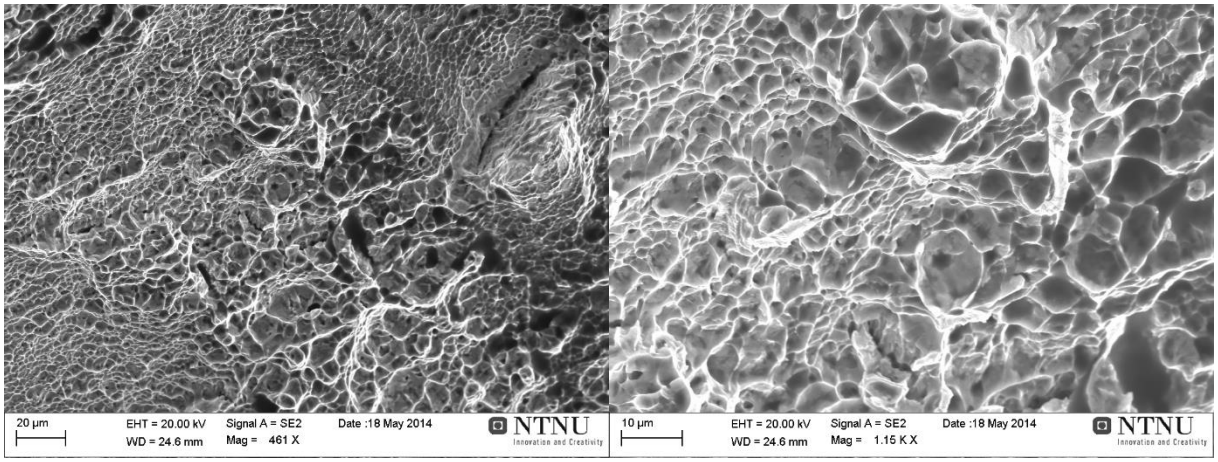

Figure 53: As-revieved material at 461X and 1150X

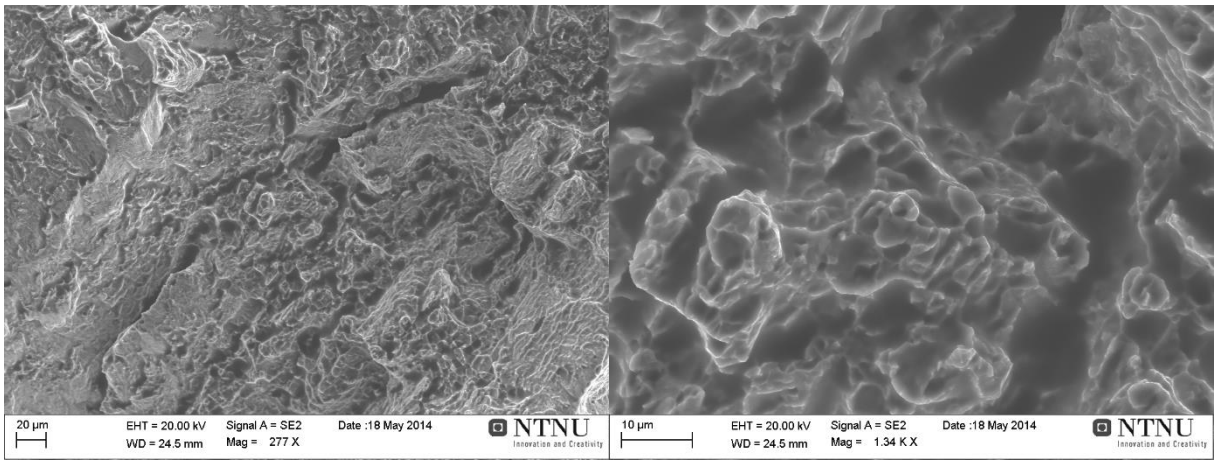

Figure 54: As-received material at 277X and 1340X

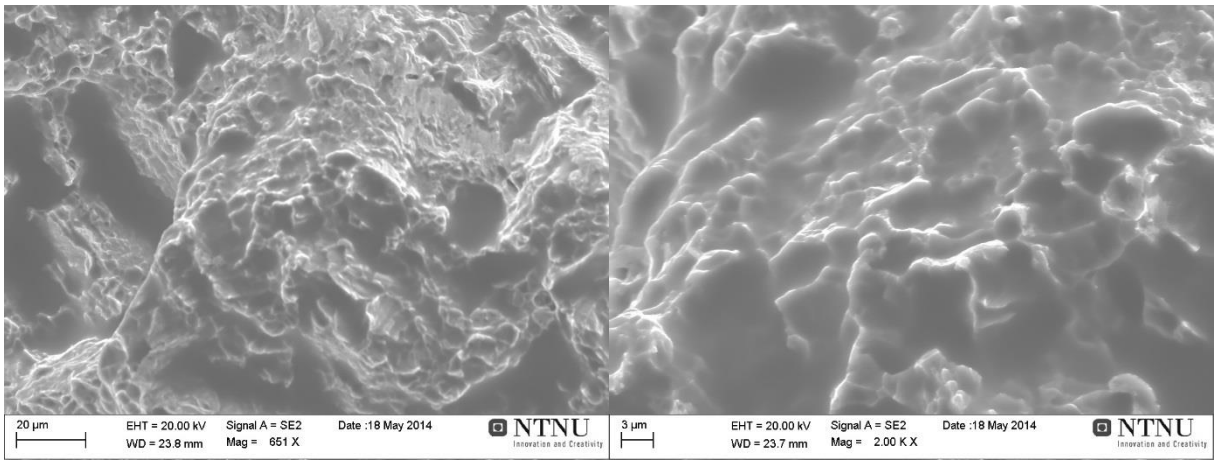

Figure 55: As-received material, at 651X and 2000X

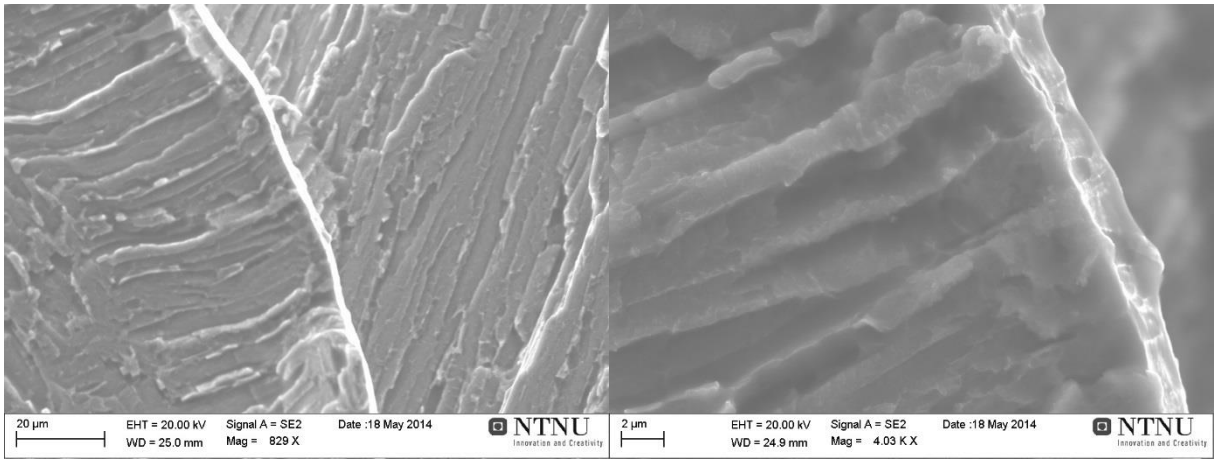

Figure 56: Contaminated specimen at 829X and 4030X

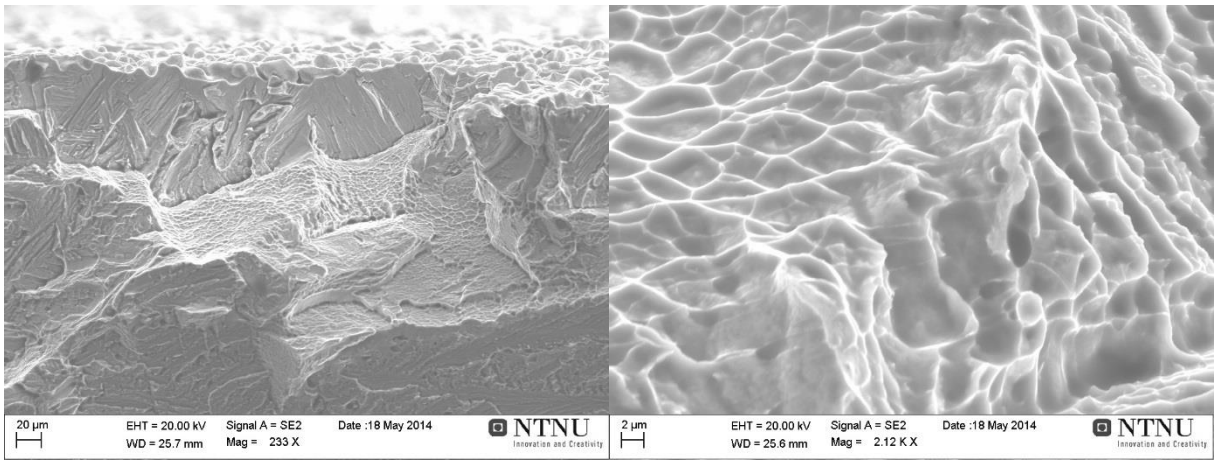

Figure 57: Contaminated specimen at 233X and 2120X

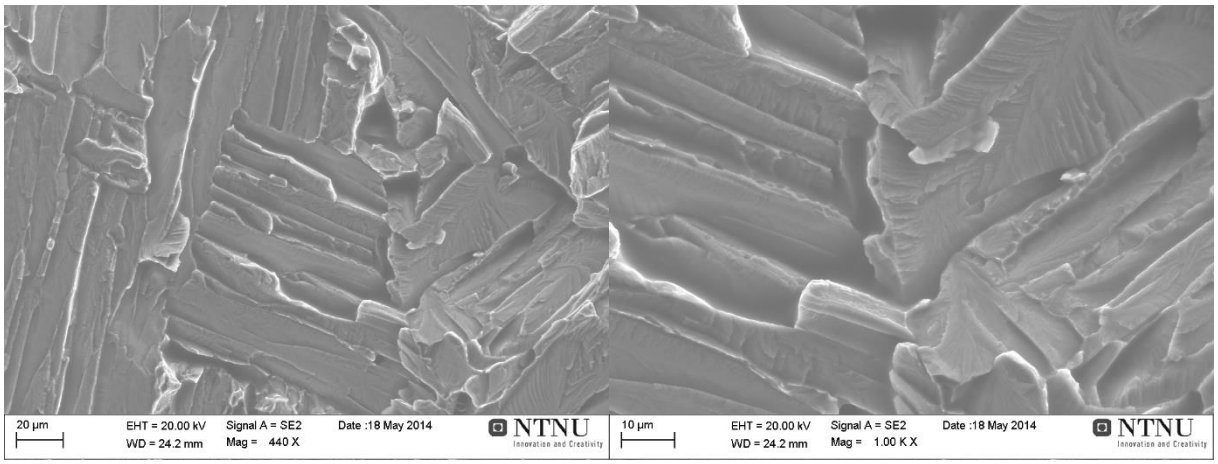

Figure 58: Contaminated specimen at 440X and 1000X

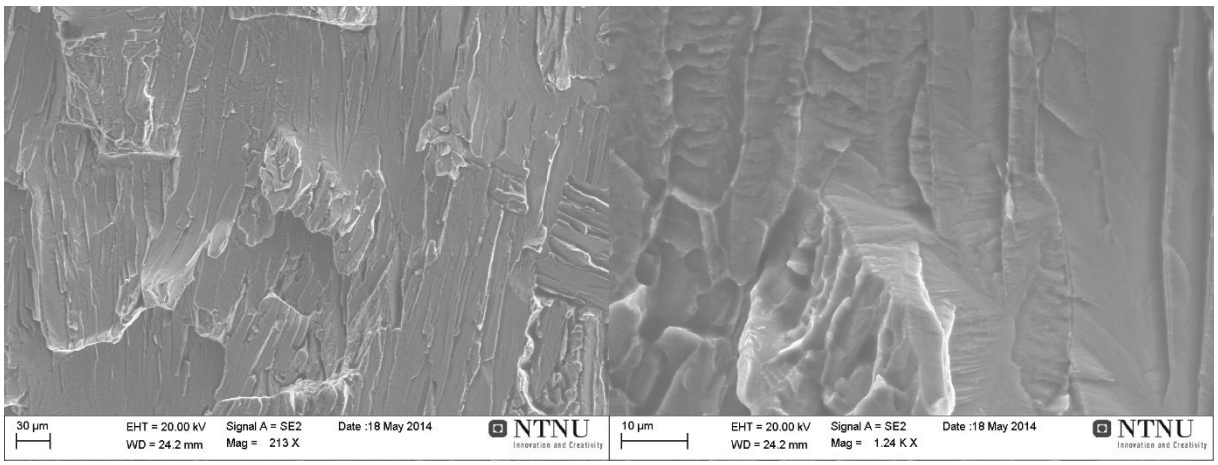

Figure 59: Contaminated specimen at 213X and 1240X

9.4 Appendix D

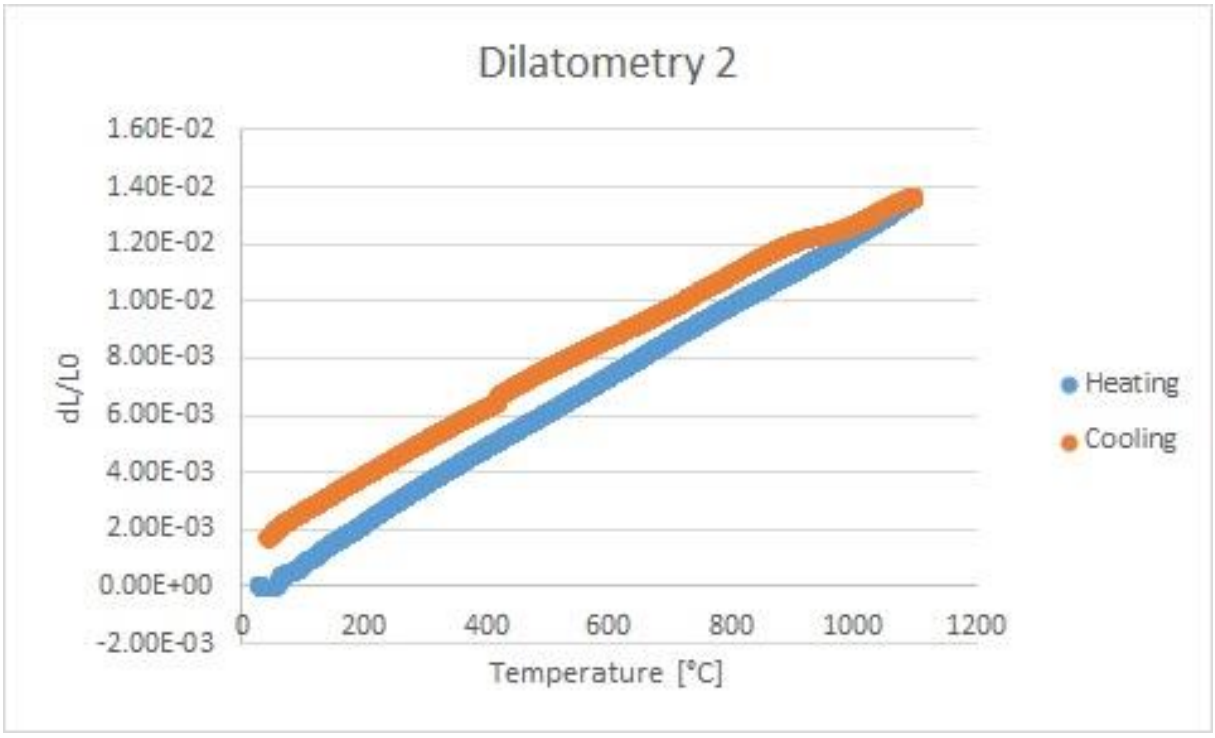

Figure 60: Dilatometry test number 2

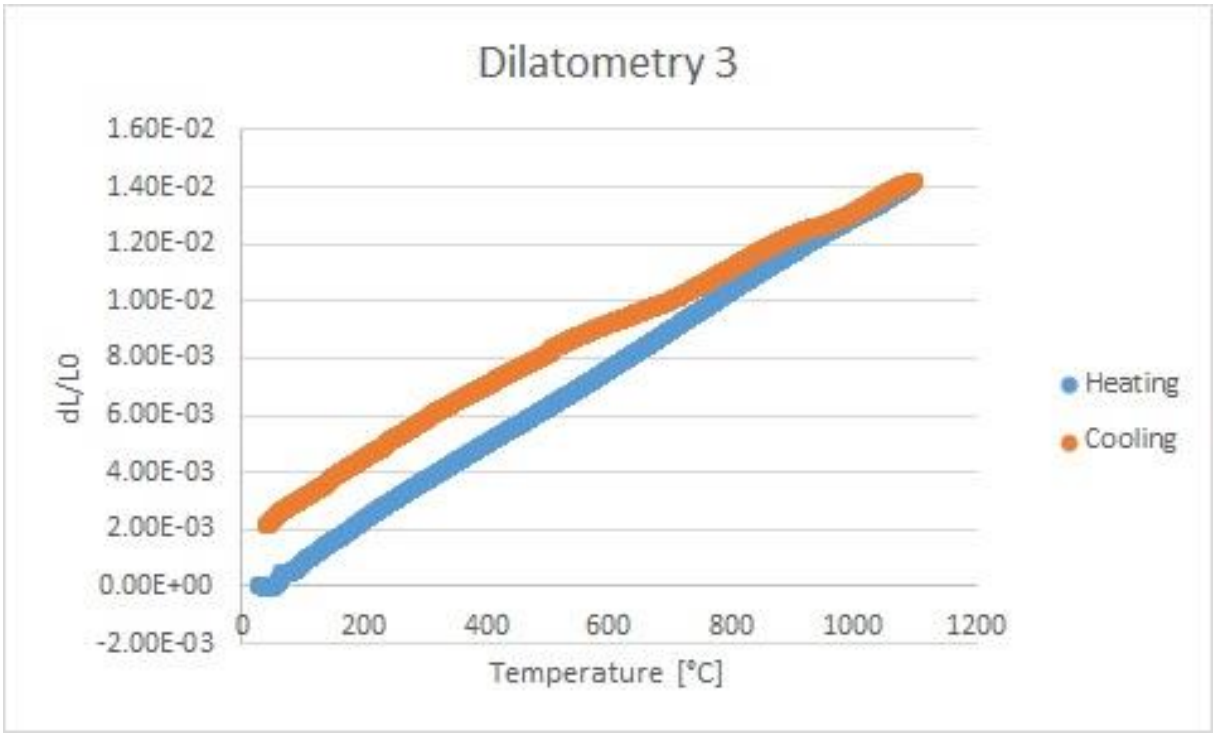

Figure 61: Dilatometry test number 3

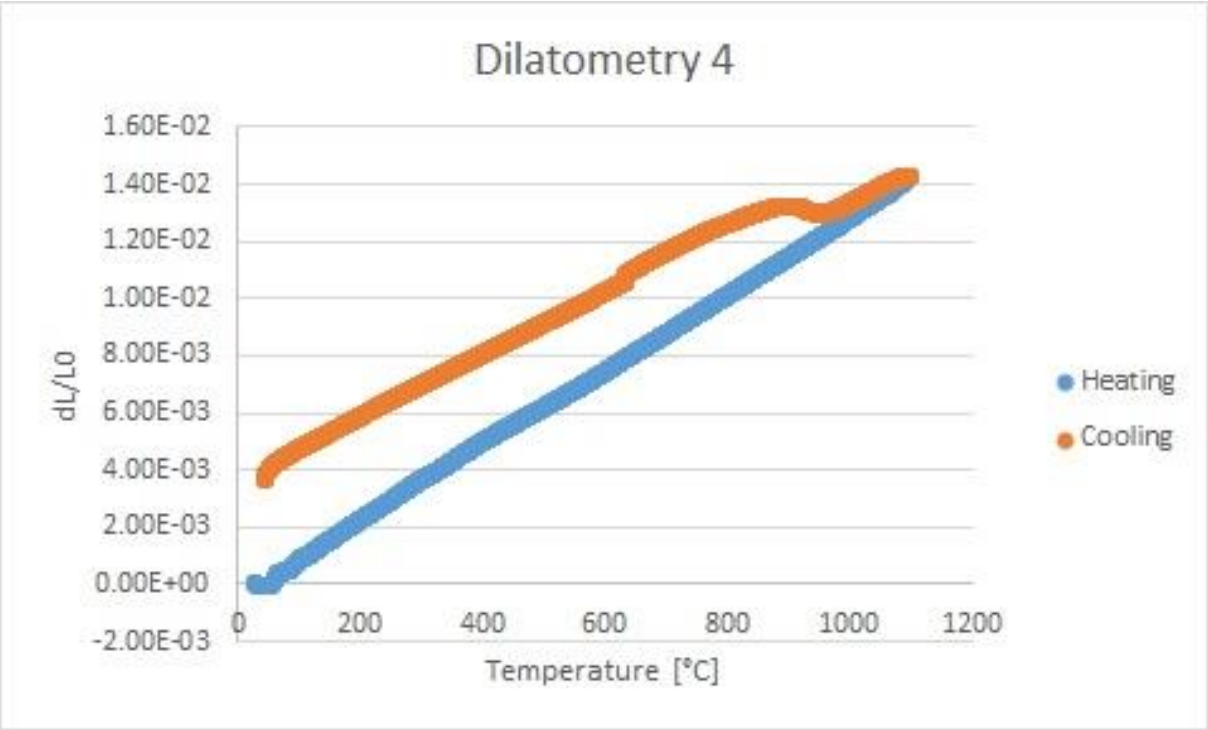

Figure 62: Dilatometry test number 4

9.5 Appendix E

Shows the different CI-, fit- and IQ-values for the different in-situ scans before any strain had been put on the specimens.

Scan	CI	Fit	IQ	Fraction good points
Air1	0.51	0.96	150.5	1
Air2	0.45	1.07	143.83	1
Air3	0.41	1.03	150.71	1
Furnace1	0.44	1.07	142.56	1
Furnace2	0.45	1.09	149.97	0.999997058
Furnace3	0.52	0.89	154.26	1
Furnace4	0.44	1.06	145.67	1
As-recieved1	0.43	1.14	131.09	0.999743935
As-recieved2	0.39	1.19	129.34	0.999973046
As-recieved3	0.36	1.23	150.18	1
Average	0.44	1.073	144.811	0.999971404
Std.dev.	0.04626013	0.09560858	8.039109963	7.6241E-05

Figure 63: Showing the CI, fit and IQ values of the in-situ tensile test at 0% strain

9.6 Appendix F

To show the problems related to calculate the elastic stiffness in OIM Analysis 6.1, a plot of a miscalculation is shown in Figure 64. It can be seen that the elastic stiffness [GPa] is much higher than the maximum theoretical stiffness of the alloy (145 GPa). In addition the new elasticity matrix are shown in Figure 65.

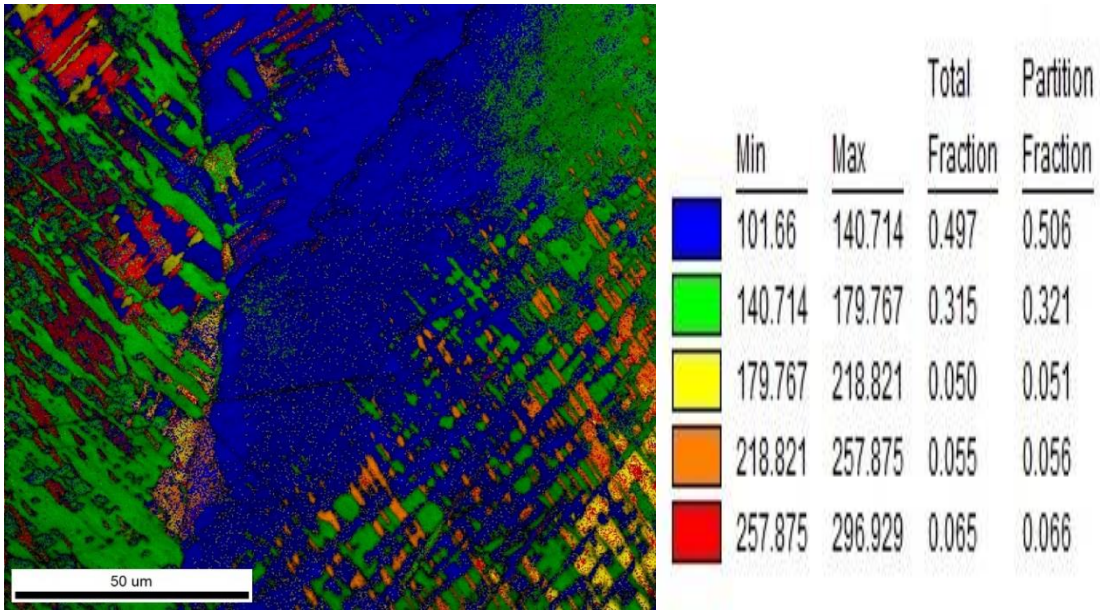

Figure 64: Shows the miscalculation performed in OIM Analysis 6.1 of the E-module. The ROI is the same as seen in Figure 29

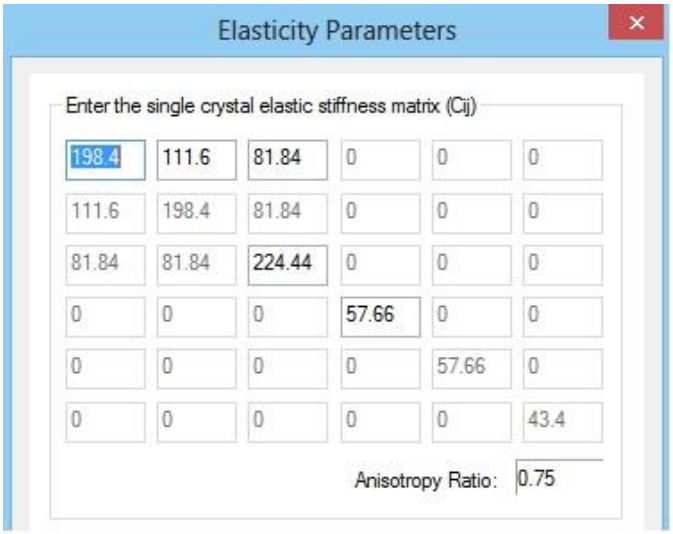

Figure 65: The new elasticity matrix used for calculations of the stiffness in OIM Analysis 6.1. The values have been scaled up a factor of 1.24 as compared to the matrix in OIM Analysis 7

9.7 Appendix G

The following images shows the ROI from the tensile test at different strain, that wasn't included.

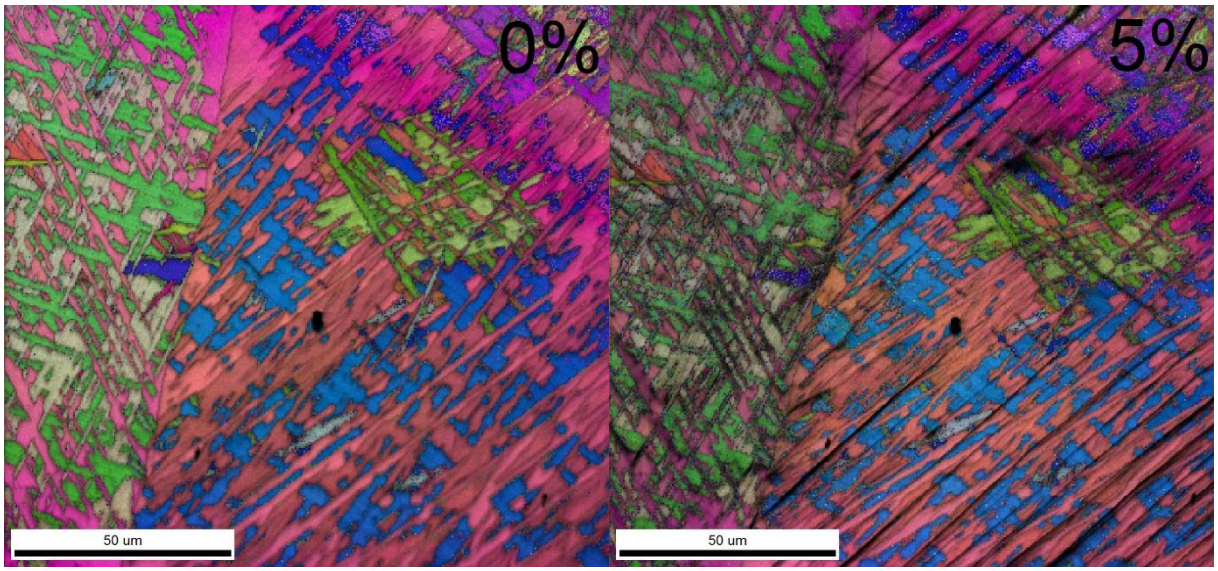

Figure 66: As-recieved material at 0% and 5% elongation

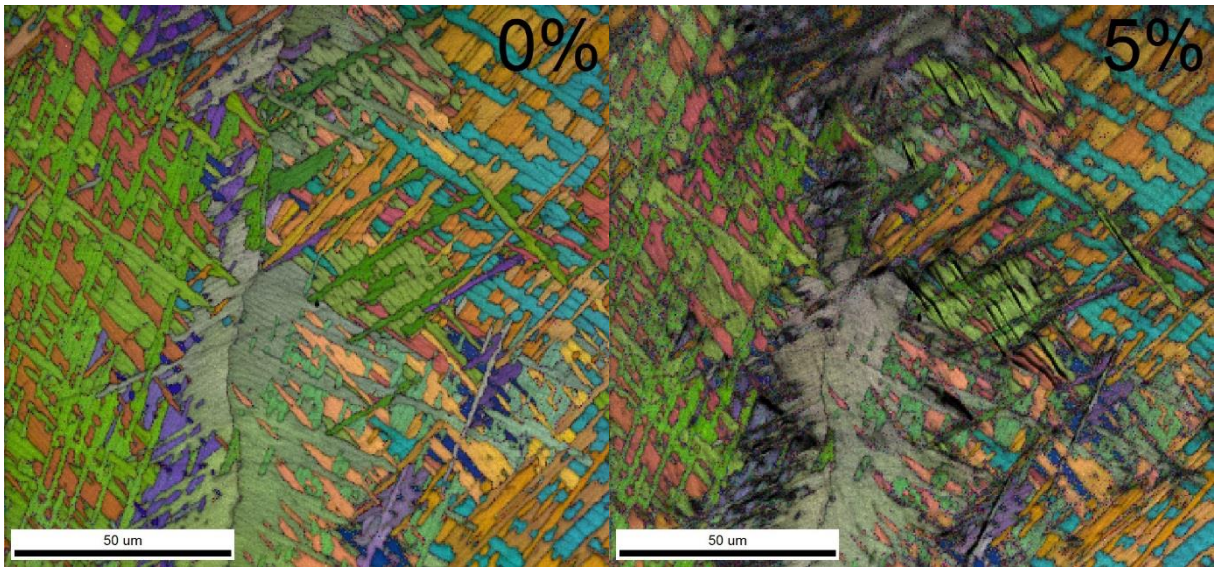

Figure 67: The as-recieved material at 0% and 5% elongation

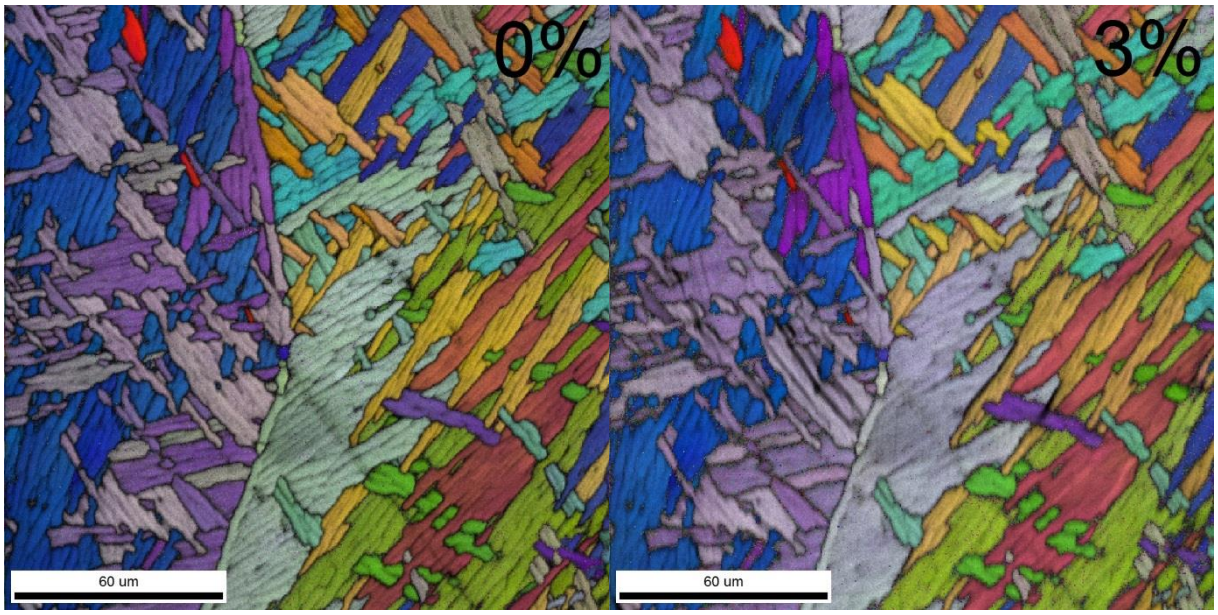

Figure 68: The AC material at 0% and 3% elongation

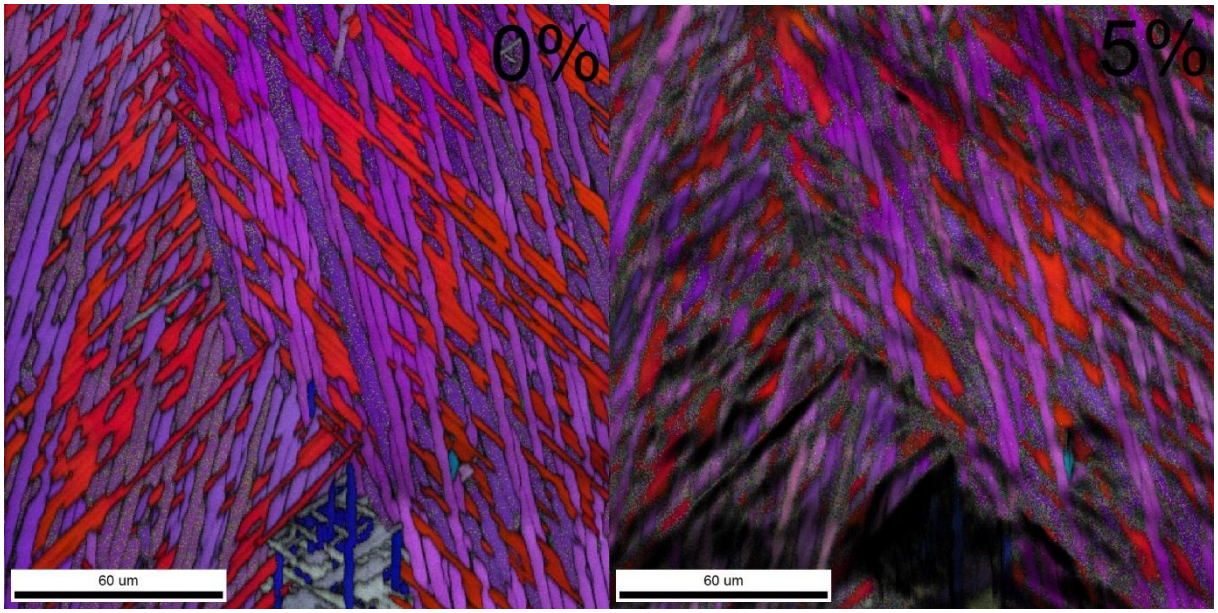

Figure 69: The AC material at 0% and 5% elongation

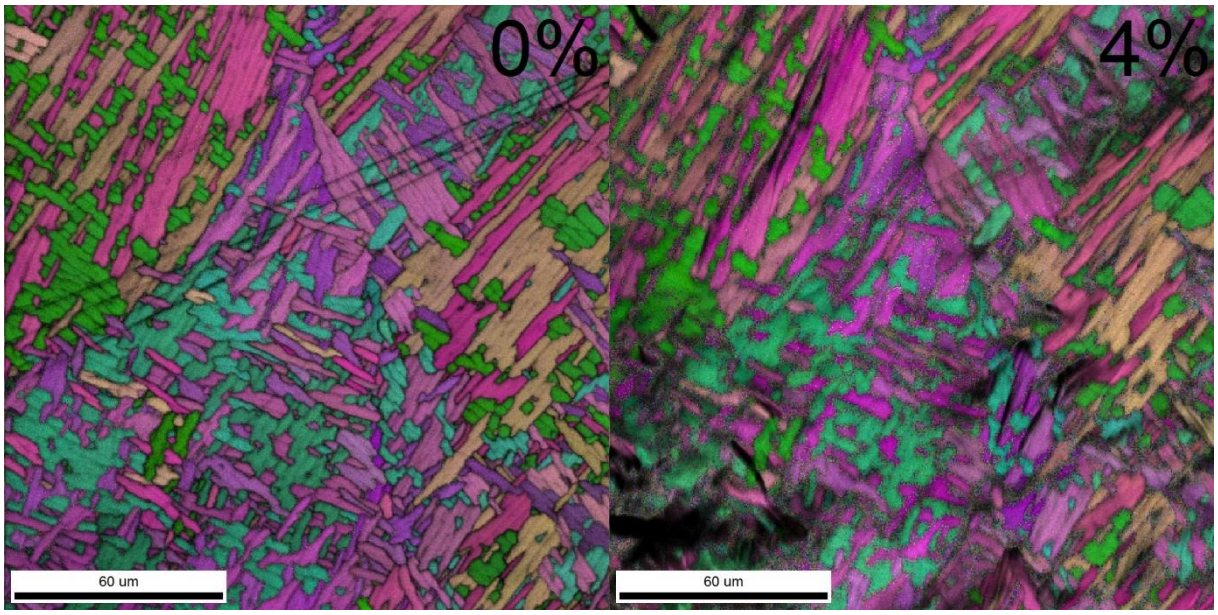

Figure 70: The FC material at 0% and 4% elongation

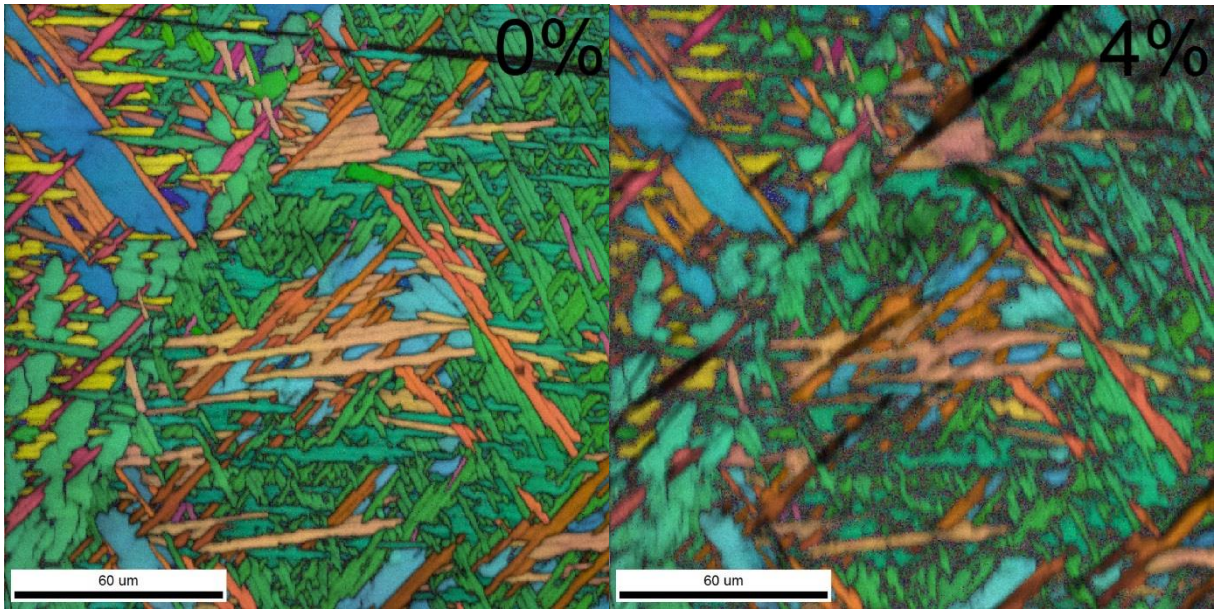

Figure 71: The FC material at 0% and 4% elongation

9.8 Appendix H

Showing the calculation of the aspect ratio for three different scans (one from each material) calculated in OIM Analysis 6.1. No noteworthy change was observed, and the microstructural change reported, are based on observations.

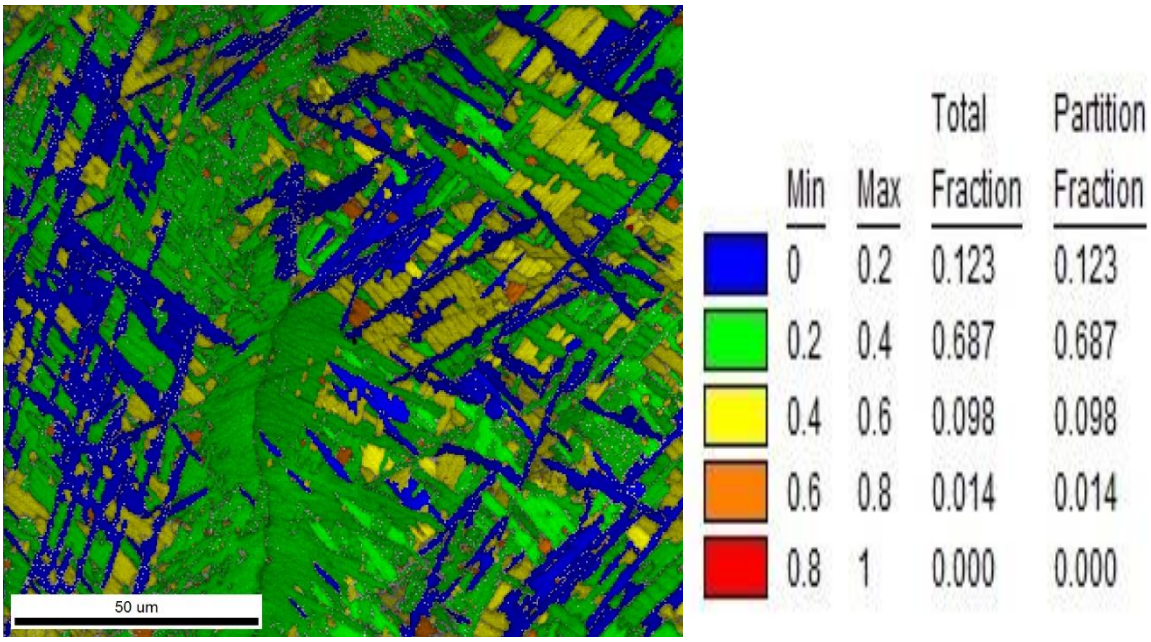

Figure 72: Aspect ratio of as-received material

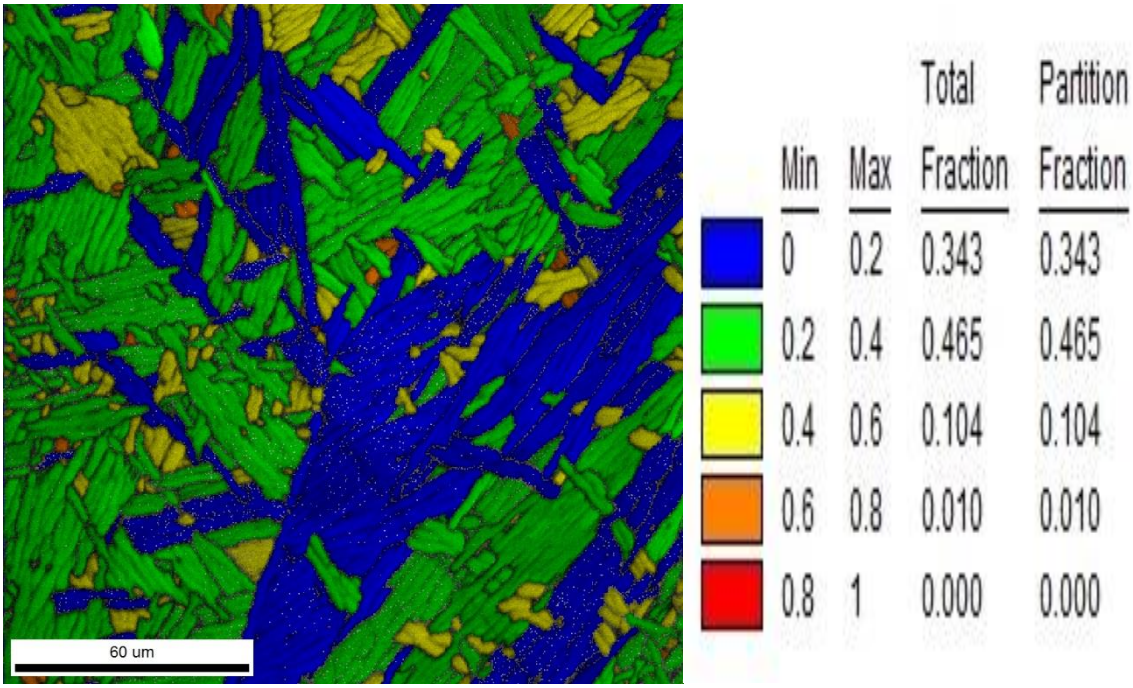

Figure 73: Aspect ratio of AC material

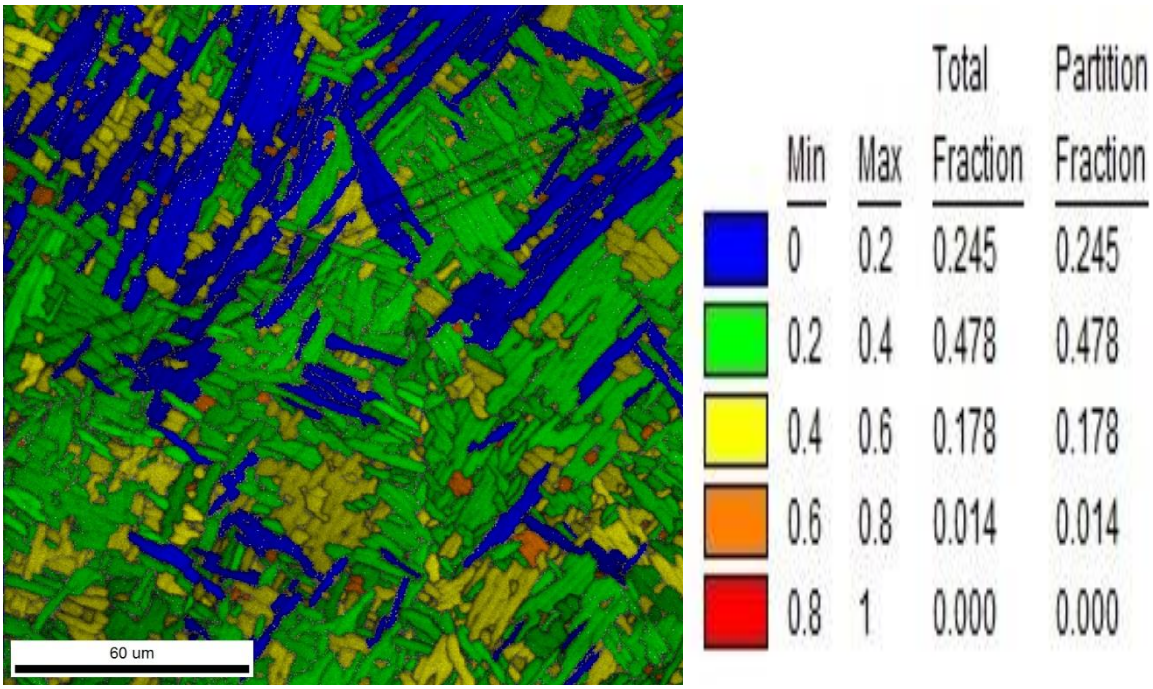

Figure 74: Aspect ratio of FC material